CERN-THESIS-2009-282

UNIVERSITÀ DEGLI STUDI DI MILANO–BICOCCA
Facoltà di Scienze Matematiche, Fisiche e Naturali

Scuola di dottorato di Scienze
Corso di Dottorato di Ricerca in Fisica e Astronomia

PERFORMANCE OF THE CMS FORWARD PIXEL DETECTOR AND ANALYSIS OF THE $B_C \to J/\psi\pi$ DECAY CHANNEL

Coordinatore: Prof. Claudio DESTRI
Tutore: Dott. Daniele PEDRINI

Tesi di: **Silvia TARONI**
Matricola: **708261**

XXII ciclo
anno accademico 2008-2009

CONTENTS

LIST OF FIGURES

LIST OF TABLES

INTRODUCTION

The Large Hadron Collider (LHC) at CERN is designed to accelerate protons at $\sqrt{s}$ = 14 TeV, with a design luminosity of $L = 10^{34}\text{cm}^{-2}\text{s}^{-1}$. During the first year of activity the machine is forseen to reach a maximum luminosity of $10^{31}\text{cm}^{-2}\text{s}^{-1}$ and energy of 10 TeV.
These luminosities and the unprecedent energy will allow the exploration of new phenomena. In particular, confirmation about the Higgs Mechanism, responsible for mass generation in the Standard Model (SM), and evidence of physics beyond the SM itself will be investigated. Since the early stage of the experiment a great interest and effort will be devoted to the Heavy Flavour physics as well.
To perform this ambitious physics program, the CMS experiment has been designed with an extended muon system, a high field solenoid, a fully active scintillating–crystal–based electromagnetic calorimeter and a inner tracker of silicon pixels and strips. Most of the reconstructed physics objects depend on the latter detector: tracks not only provide the momentum measurement for charged particles, but also they are input for primary and secondary vertex reconstruction and for b- and τ- tagging algorithms.
Particularly challenging is the innermost component of the tracking system, whose performance study is subject of this thesis. This pixel detector is composed of a barrel region of 3 layers of silicon at a radius of 4.4, 7.3 and 10.2 cm and a forward region of four disks of pixels, two at each end of the barrel region. The disks are at 34.5 and 46.5 cm, in both directions, from the interaction point and their inner and outer radii are 6.1 and 15.0 cm, respectively. As a consequence of these short distances, the pixel detector lives in a harsh environment and is expected to integrate a maximum dose of about 7 Mrad per year on the inner edge of the first disk at the full LHC design luminosity of 10^{34} $\text{cm}^{-2}\text{s}^{-1}$ at 14 TeV center-of-mass energy. At higher radius, the integrated dose per year should decrease as $\sim \text{r}^{-1.8}$. To study the effects of such a high dose on the forward pixel detector performance, a pre-production plaquette of 2 $\times$ 4 ROCs was exposed to a peak dose of 45 Mrad at the Indiana University Cyclotron Facility using a 200 MeV proton beam. Once completed the irradiation process, the plaquette was tested on the test-beam at Fermilab in July 2006 to study the long term performance.

The analysis of the collected data is discussed in the first part of this work. A deterioration in the charge collection efficiency is present: the signal released by a minimum ionizing particle is $\sim$ 75% of the expected value. The detection efficiency, though, remains very high, $\sim$99%, and despite the observed damages, the detector remains fully operational and certainly suitable to accomplish the CMS physics goals at the expected fluence after several years of running at the LHC luminosity.
These results are promising for the success of the heavy flavour physics program in CMS: the heavy flavoured mesons and baryons will be, in fact, identified through reconstruction of their primary and secondary vertices.
Measurements in CMS will contribute to improve our knowledge of the high mass states such as B_s, B_C, Λ_b and Ω_b not yet extensively studied.
The analysis of the $B_C \to J/\psi\pi$ decay channel is subject of the second part of the thesis. The B_C meson, the ground state of the $(\bar{b}c)$ system, is doubly heavy flavoured; it is then unique in providing a new window to study heavy–quark dynamics: with the doubly heavy flavour will complement the phenomenological information obtained from charmonium and bottomonium.
The B_C decay processes can be divided into three classes:

- the b quark decay with the c quark as a spectator;
- the c quark decay with the b quark as a spectator;
- annihilation channel.

In spite of several theoretical predictions, results from experimental investigation are still limited to only two channels:

$$B_C \to J/\psi\pi \qquad \text{and} \qquad B_C \to J/\psi l\nu.$$

The first observation of the B_C meson was reported in 1998 by the CDF experiment at the Fermilab Tevatron collider through the decay channel $B_C \to J/\psi l\nu$. In the following ten years, as the Tevatron luminosity increased, a larger statistics allowed the analysis of the $B_C \to J/\psi\pi$ channel as well, suppressed for its smaller Branching Ratio (theoretical prediction: BR($B_C \to J/\psi\pi$)$\sim$0.13%, BR($B_C \to J/\psi\mu\nu_\mu$)$\sim$1.9%).
The B_C mass and lifetime were determined. However, the lifetime measurement is still limited to the semileptonic channel and is affected by a large statistical uncertainty of the order of 10%.
A complication in the B_C feasibility studies in the experiment arises because of its small production rate: $\sim 10^{-3}$ $b\bar{b}$ production. A dedicated generator is necessary to produce, in a reasonable time, enough B_C mesons which then decay in the CMS spectrometer and are processed through the full detector simulation and reconstruction. An event generator is available: BCVEGPY.
The first step of my work in the B_C study has been the integration of the generator in the CMS simulation package (CMSSW). BCVEGPY emulates a Matrix

Elements (ME) generator and generation can be stopped at the "parton" level. The information of the B_C^+ meson plus the two additional quarks, b and $\bar{c}$, are written out in a file in the Les Houches Accord format, which can be easily interfaced with the different hadronizer models. In the present work, the interface has been implemented and the LHE output file has been hadronized by PYTHIA. The core of this generator has not been modified from the authors' original version.

In the analysis of $B_C \to J/\psi\pi$ channel, the J/ψ decays into two muons. The event reconstruction starts from the selection of the two muons coming from the J/ψ; a third charged track (π) is then associated to form a three–track secondary vertex. An integrated luminosity of 200 pb^{-1} (first year data collection, 2009 Chamonix schedule) corresponds to $\sim$ 70 events. Both the signal yield and the mass resolution (35 MeV) are already competitive with the current results from the CDF and D0 experiments.

The lifetime measurement from Tevatron in the semileptonic decay require a Monte Carlo correction due to the undetected neutrino. The $B_C \to J/\psi\pi$ channel can be fully reconstructed and free from this correction.

With 1 fb^{-1} of data, CMS can carry out a lifetime determination with a statistical precision of $\sim$7%, to be compared with the $\sim$ 10% from CDF and D0 experiments. At 200 pb^{-1}, the precision is estimated $\sim$15%.

In conclusion, the B_C mass and lifetime measurements will be carried out since the early stages of data taking in channels through $J/\psi \to \mu^+\mu^-$. As the statistics increases more decay channels will be explored to enrich our knowledge of this unique state. When sufficient statistical precision will be reached, tests with theoretical predictions will be carried out to elucidate the heavy quark dynamics sector.

The pixel detector will play a crucial role in the heavy flavour analysis; test–beam measurements of resistance to high dose assure the necessary good long term performance.

CHAPTER 1

THE LHC AND THE CMS EXPERIMENT

CMS is one of the two general purpose experiments of the CERN Large Hadron Collider (LHC).
In this chapter the LHC is introduced and the detector requirements of CMS are illustrated. After a description of the subdetectors, the CMS trigger architecture is presented.

1.1 THE LHC MACHINE

The Large Hadron Collider (LHC) is the proton-proton (p–p) collider installed in the LEP tunnel at CERN. It is designed to collide protons with a center of mass energy up to 14 TeV, with a design luminosity $L = 10^{34}\text{cm}^2\text{s}^{-1}$ and a bunch crossing of 25 ns.
A p–p collider has been chosen instead of an e^+e^- one to reduce the synchrotron radiation and to be able to accelerate the particles up to a very large energy; it was preferred to a $\bar{p}p$ collider because it allows to reach higher luminosity.
The basic layout of the machine, presented in fig 1.1, mirrors the LEP one, with eight straight sections each approximately 528 m long.
Four experiments are installed along the circumference; CMS and ATLAS are located at diametrically opposite straight sections. ALICE and LHCb are located at point 2 and point 8.
Some machine parameters relevant for the CMS operations are listed in table 1.1 [1].
The bunches are formed in the 26 GeV Proton Synchrotron (PS) with the correct 25 ns spacing. The beam is then accelerated in the Super Proton Synchrotron (SPS) and transferred to LHC. The SPS accelerates the beam to 450 GeV and transfers each batch (containing 2.4×10^{13} protons) to one or another LHC rings. Once both rings are filled, the beams are accelerated to the nominal

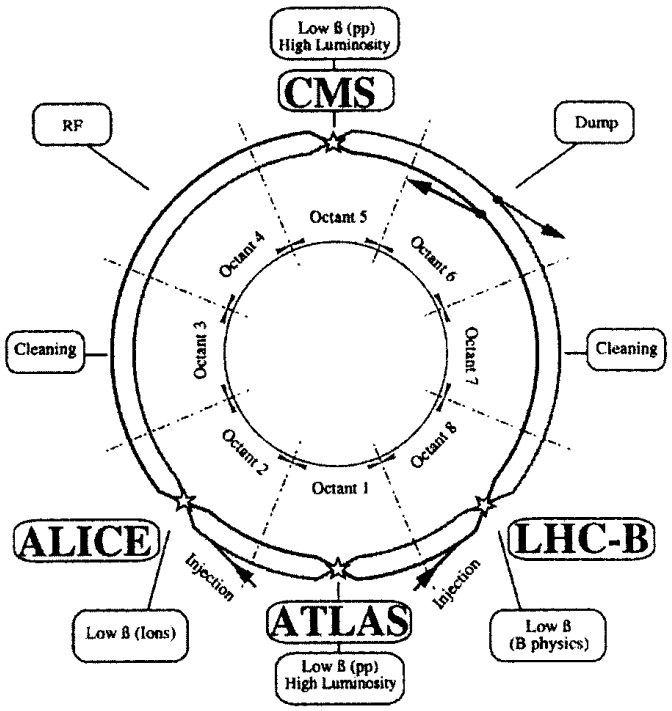

Figure 1.1.: Schematic layout of LHC.

		pp	**HI**
Energy per nucleon	E (TeV)	7	2.76
Dipole field at 7 TeV	B (T)	8.33	8.33
Design luminosity	$\mathcal{L}$ $\frac{1}{\mathrm{cm}^2\mathrm{s}}$	10^{34}	10^{27}
Bunch separation	(ns)	25	100
# of bunches	k_B	2808	592
# particles per bunch	N_p	1.15×10^{11}	7.0×10^{7}

Table 1.1.: The machine parameters relevant for the LHC detectors. – For heavy ion (HI) operation the designed luminosity for Pb-Pb is given.

collision energy [2]. For the physics runs, the number of bunches per beam is foreseen to be up to 2808, with a zero crossing angle, a transverse radius of 15 μm and and a length 7.5 cm in the beam direction.
Accelerating protons up to 14 TeV with a bending radius of $\approx$ 2878 m requires a bending magnetic field of 8.4 T. In the LHC machine this field is provided by 1232 cryodipoles. They are superconductive magnets working at 1.9 K, installed in the eight curved sections of the ring. The current inside the magnets is $\sim$11700 A and they use the two in one design where both magnetic channels

are incorporated into a single iron yoke and cryostat (fig 1.2).

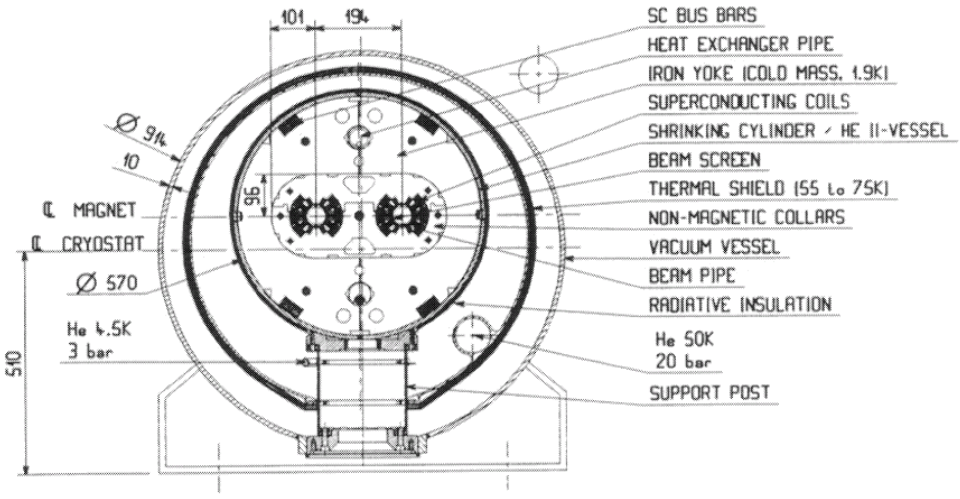

Figure 1.2.: Dipole magnet cross section.

1.2 THE CMS DETECTOR

The beam energy and the design luminosity of the LHC have been chosen in order to study physics at the TeV energy scale. A wide range of physics is potentially possible with the seven-fold increase in energy and hundred-fold increase in integrated luminosity over the previous hadron collider experiment. These condition also require a very careful design of the detector.
At the design luminosity a mean of about 20 inelastic collisions will be superimposed on the event of interest. This implies that around 1000 charged particle will emerge from the interaction point every 25 ns. The products of the interaction under study may be confused with those from other interaction in the same bunch crossing. The problem become more severe when the response time of the detector is longer than 25 ns. The effect of pile up can be reduce using high granularity detectors with good time resolution, resulting in low occupancy. This requires a large numbers of detector channels. The resulting millions of detector electronic channels require a very good synchronization.
The large flux of particles coming from the interaction region leads to high radiation levels, requiring radiation-hard detectors and front end electronics.
The detector requirements for the CMS to meet the goals of the LHC physics program can be summarized as follows:

- Good muon identification and momentum resolution over a wide range of momenta in the region $|\eta| < 2.5$; good dimuon resolution ($\approx 1\%$

at 100 GeV) and the ability to determine unambiguously the charge of muons with p < 1 TeV.

- Good charged particle momentum resolution and reconstruction efficiency in the inner tracker. Efficient triggering and offline tagging of τ and b jets, requiring pixel detectors close to the interaction region.

- Good electromagnetic energy resolution, good diphoton and dielectron mass resolution ($\approx$ 1% at 100 GeV), wide geometric coverage ($|\eta| < 2.5$), measurement of the direction of photons and/or correct localization of the primary interaction vertex, π^0 rejection and efficient photon and lepton isolation at high luminosity.

- Good E_T^{miss} [1] and dijet mass resolution, requiring a hadron calorimeter with a large hermetic geometric coverage ($|\eta| < 5$) and with a fine lateral segmentation.

CMS meets these requirements with a high field solenoid, a full silicon inner tracking system and a homogeneous scintillating crystal-based electromagnetic calorimeter [3].
The coordinate system adopted by CMS has the origin centered at the nominal collision point inside the experiment, the y-axis pointing vertically upward, and the x-axis pointing radially inward toward the center of the LHC. Thus, the z-axis points along the beam direction toward the Jura mountains from LHC Point 5. The azimuthal angle ϕ is measured from the x-axis in the x-y plane and the radial coordinate in this plane is denoted by r. The polar angle θ is measured from the z-axis. Pseudorapidity is defined as $\eta = -\ln \tan(\theta/2)$. Thus, the momentum and energy transverse to the beam direction, denoted by p_T and E_T , respectively, are computed from the x and y components.

1.2.1 THE OVERALL CONCEPT

One of the requirements for the CMS detectors is a good momentum resolution for muons, which results in a large bending power and thus the use of superconducting technology for the magnet. The magnet dimensions have driven the detector design and layout. The whole CMS detector is shown in fig 1.3.
The overall dimensions of the CMS detector are 21.6 m (length) $\times$ 14.6 m (diameter) for a total weight of 12500 tons.
A 4 T magnetic field (current value: 3.8 T) is created by a 13 m long, 6 m inner diameter superconducting solenoid. This high magnetic field was chosen in order to achieve a good momentum resolution within a compact spectrometer. The return field is large enough to saturate 1.5 m of iron, allowing 4 muon "stations" to be integrated and to ensure robustness and full geometric coverage. Each muon station consists of several layers of aluminum drift tubes (DT)

[1] The E_T^{miss} is the imbalance of energy measured in the transverse plane

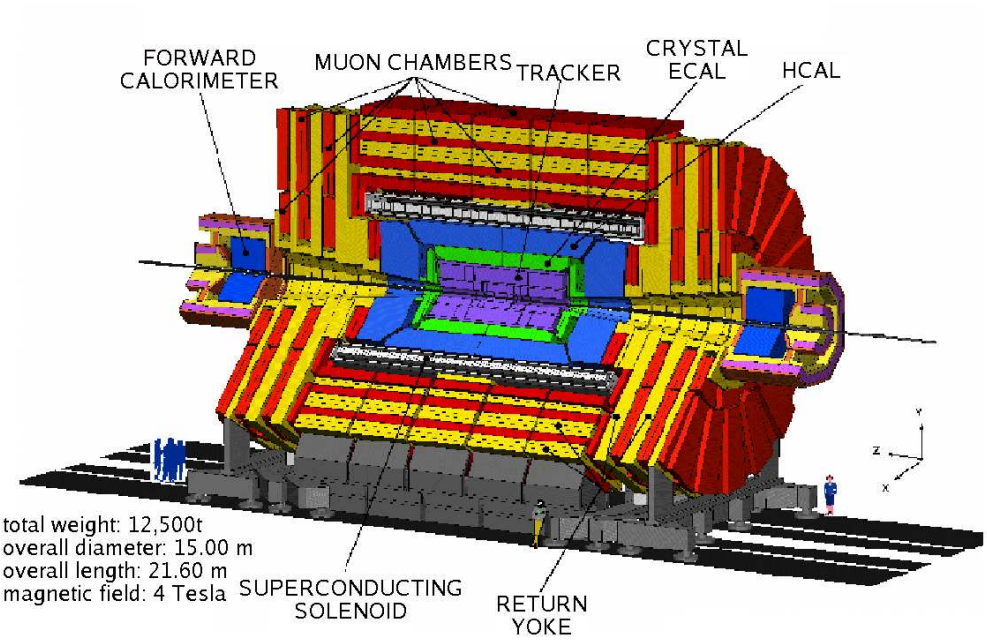

Figure 1.3.: View of the CMS detector.

in the barrel region and cathode strip chambers (CSC) in the endcap region, complemented by resistive plate chambers (RPC).
The bore of the magnet coil is large enough to accommodate the inner tracker and the calorimeter inside. The tracking volume is given by a cylinder 5.8 m long and 2.6 m in diameter. It is composed of 10 layers of silicon microstrip detectors and 3 layers of silicon pixel detectors to improve the measurement of the impact parameter of charged particle tracks and the position of secondary vertices.
The electromagnetic calorimeter (ECAL) is built with lead tungstate ($PbWO_4$) crystals and it covers a pseudorapidity region up to $|\eta| < 3.0$. The scintillation light is detected by silicon avalanche photodiodes (APD) in the barrel region and vacuum phototriodes (VPT) in the endcap regions. A preshower system is installed in front of the endcap ECAL for π^0 rejection. The ECAL is surrounded by a brass/scintillator sampling hadron calorimeter with coverage up to $|\eta| < 3.0$. The scintillation light is converted by wavelength-shifting (WLS) fibres embedded in the scintillator tiles and brought to photodetectors by means of clear fibres. The light is detected by hybrid photodiodes (HPD). This central calorimeter is completed by a "tail-catcher" in the barrel region ensuring that hadronic showers are sampled with 11 hadronic interaction lengths. Coverage up to a pseudorapidity of 5.0 is provided by an iron/quartz calorimeter. The Cherenkov light emitted in the quartz fibres is detected by photomultipliers. The forward calorimeter ensures full geometric coverage for the measurement of the transverse energy in the event.

Fig 1.4 presents the different detector parts in the transverse section in the barrel region.

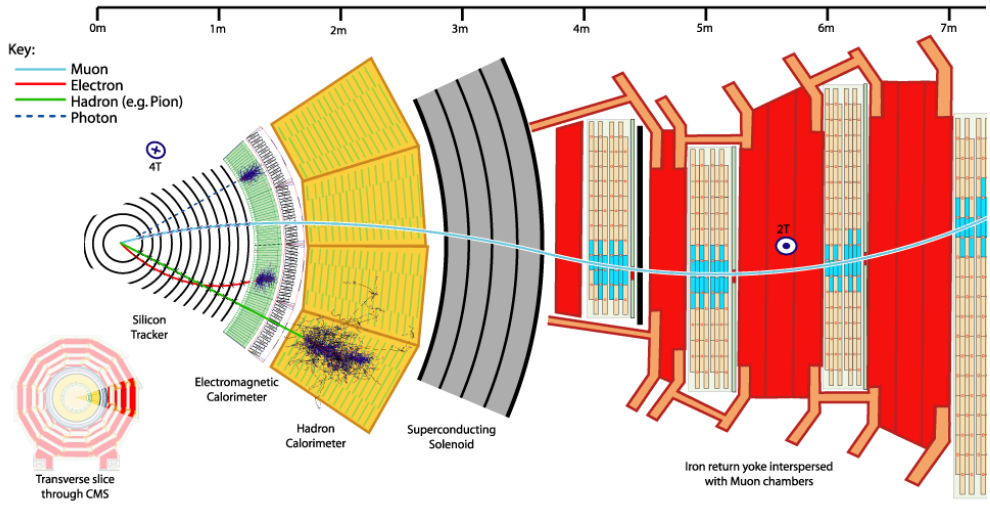

Figure 1.4.: The transverse section of the barrel region of the CMS detector with a muon track.

1.2.2 THE MUON SYSTEM

In CMS the muons produced in the central region are measured three times: in the inner tracker, after the coil and in the return flux. Three types of gaseous detectors are used to identify and measure muons [4]. The choice is driven by the different radiation environments. In the barrel region ($|\eta| < 1.2$), where the neutron induced background is small, the muon rate is low and the residual magnetic field in the chamber is low, drift tube chambers are used (fig 1.5a presents the installation into the wheels). In the two endcaps where the muon and the neutron induced background rates are high, and the magnetic field is also high, cathode strip chambers (CSC) are used and cover the region up to $|\eta| < 2.4$ (fig 1.5b). In addition to these, resistive plate chambers (RPC) are installed in both the barrel and the endcap regions as presented in fig 1.6. The RPCs operate in an avalanche mode to ensure good operation at high rates (up to 10 kHz/cm^2). RPCs provide a fast response with good time resolution but with a coarser position resolution than the DTs or CSCs. RPCs can therefore identify unambiguously the correct bunch crossing.
The DTs or CSCs and RPCs operate within the first level trigger system.
Fig 1.6 presents one quarter of the muon system. In the muon barrel (MB) region, 4 stations of detectors are arranged in cylinders interleaved with the

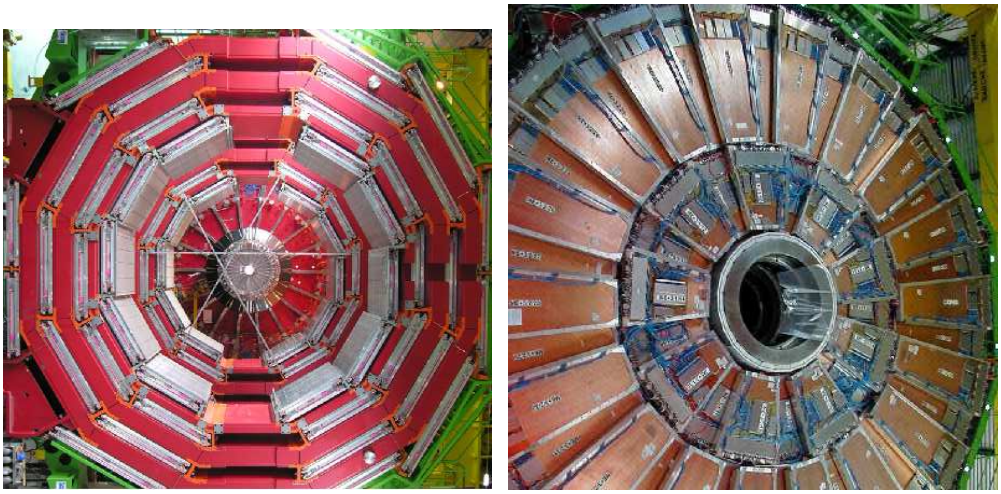

(a) (b)

Figure 1.5.: (a) Installation of the DT into the wheels. (b) Installation of the CSC chambers on one disk.

iron yoke. The segmentation along the beam direction follows the 5 wheels of the yoke. In each of the endcaps, the CSCs and the RPCs are arranged in 4 disks perpendicular to the beam, and in concentric rings, 3 rings in the innermost station, and 2 in the others. In total, the muon system contains of the order of 25000 m^2 of active detection planes, and nearly 1 million electronic channels. The expected resolution for the muon transverse momentum for different η ranges is presented in fig 1.7.

1.2.3 HADRONIC CALORIMETER

The hadronic calorimeter (HCAL) is located inside the magnet coil and surrounds the electromagnetic calorimeter (ECAL) system. The location drove the choice of the design. The HCAL design has minimized the non gaussian tails in the energy resolution providing good containment and hermeticity for E_T^{miss} measurement. There is also an additional layer of scintillators, referred to as the hadronic outer (HO) detector, lining the outside of the coil. The layout of the whole detector is in fig 1.8

Brass[2] has been chosen as the absorber material as it has a reasonably short interaction length and it is non magnetic. The innermost and the outermost absorber layers are made of stainless steel for structural reasons. The active medium consists of 17 layers of plastic scintillator tiles readout with embedded WLS fibres. The WLS fibres are spliced to high attenuation length clear fibres outside the scintillator that carry the light to the readout system. The photodetection readout is based on multi channel hybrid photodiodes. The absorber

[2]Brass # 260 with 70% copper and 30% zinc

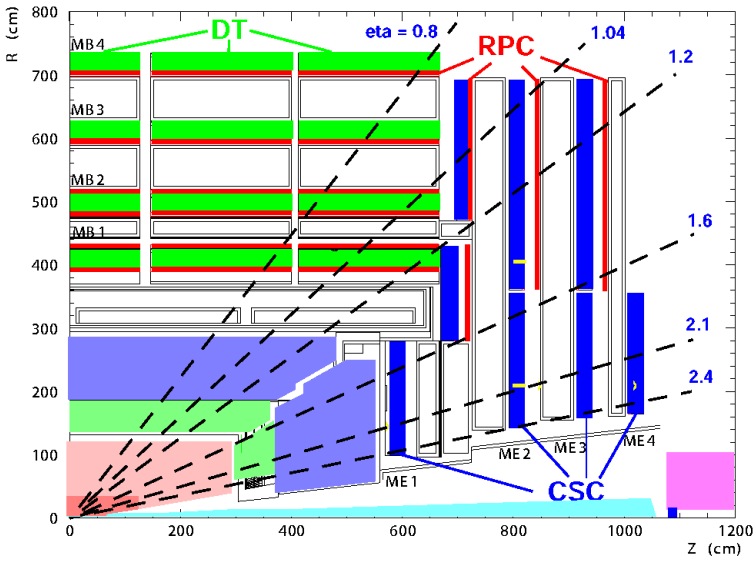

Figure 1.6.: Layout of a quarter of the CMS muon system for the initial low luminosity running. The RPC system is limited to $|\eta| < 1.6$ in the endcap, and for the CSC system only the inner ring of the ME4 (the last CSC in figure) chambers have been deployed.

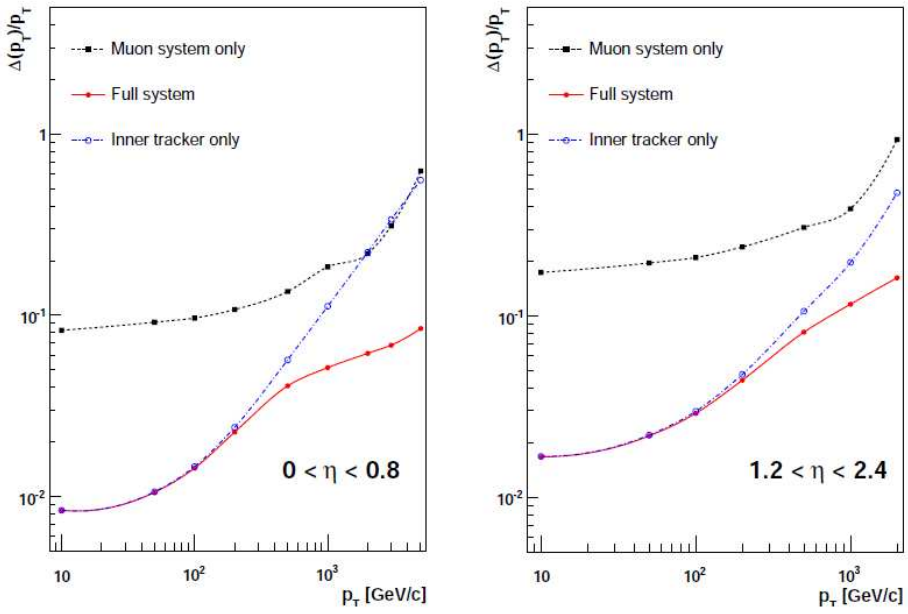

Figure 1.7.: Simulated muon p_T resolution in different η ranges

structure is assembled by bolting together precisely machined and overlapping brass plates so as to leave space to insert the scintillator plates, which have a thickness of 3.7 mm. The longitudinal profile in the barrel going from an inner radius of 177.7 cm to an outer one of 287.65 cm is the following:

- **Layer 0:** 0.9 cm scintillator / 6.1 cm stainless steel
- **Layer 1-8:** 0.37 cm scintillator / 5.05 cm brass
- **Layer 9-14:** 0.37 cm scintillator / 5.65 cm brass
- **Layer 15-16:** 0.37 cm scintillator / 7.5 cm stainless steel / 0.9 cm scintillator

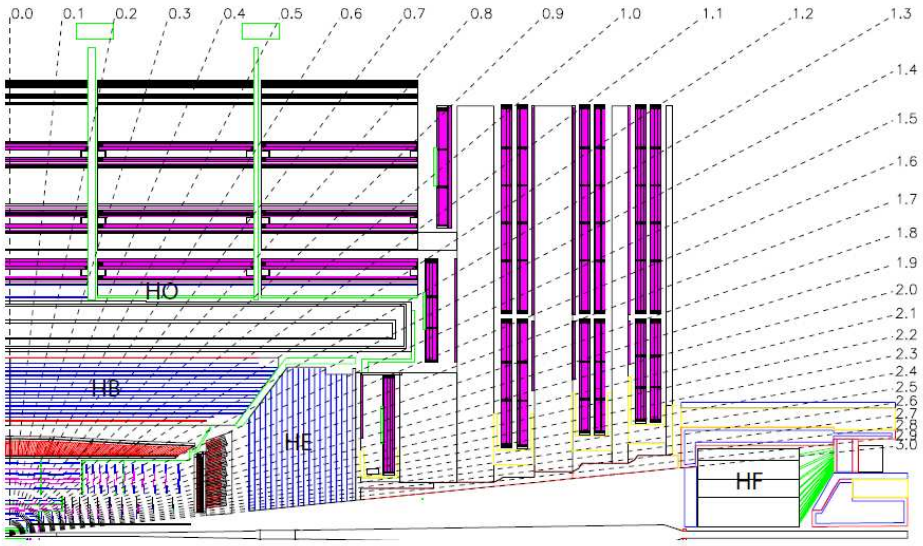

Figure 1.8.: Longitudinal view of the CMS detector showing the locations of the hadron barrel (HB), endcap (HE), outer (HO) and forward (HF) calorimeters.

where the layer number refers to the active scintillator layer. The endcap calorimeter brass absorber thickness is 7.8 cm while the scintillator one is 0.37 cm. In the endcaps there are 19 active plastic scintillator layers.
The overall assembly enables the HCAL to be built with essentially no instrumented cracks or dead areas in ϕ. The gap between the barrel (fig 1.9a) and the endcap HCAL (fig 1.9b), through which the services of the ECAL and the inner tracker pass, has an inclination of 53° and points away from the center of the detector.
The hadron outer detector (HO) is made of 1.0 cm thick scintillators, which are located outside of the outer vacuum tank of the coil and cover the region

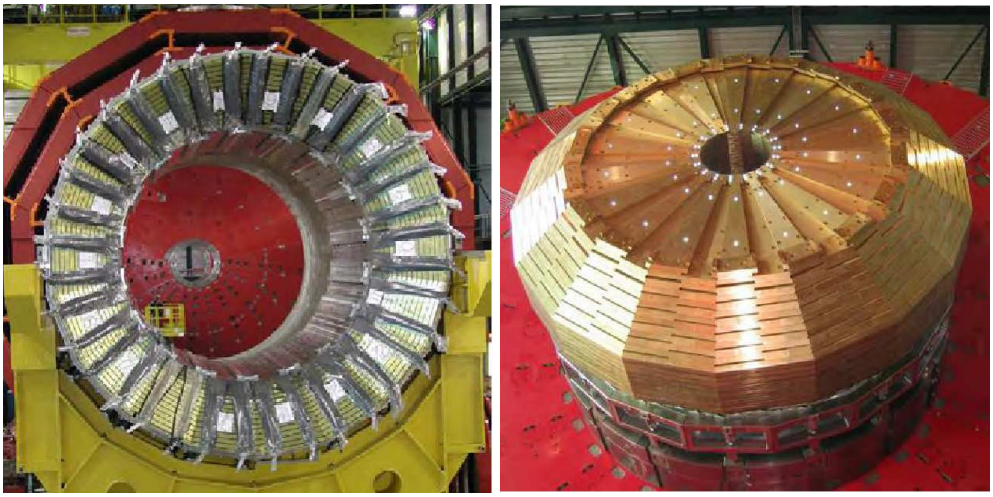

(a) (b)

Figure 1.9.: (a) The hadron barrel calorimeter. (b) The hadron endcap calorimeter.

$-1.26 < \eta < 1.26$. The tiles are grouped in 30° sectors, matching the ϕ segmentation of the DT chambers. They sample the energy of the penetrating hadron showers leaking through the rear of the calorimeters and so serve as a "tail-catcher" after the magnet coil. They increase the effective thickness of the hadron calorimeter to over 10 interaction lengths, thus reducing the tails in the energy resolution function. The HO also improves the E_T^{miss} resolution of the calorimeter itself.

Coverage between pseudorapidities of 3.0 and 5.0 is provided by the steel/-quartz fibre hadron forward calorimeter (HF). Since the neutral component of the hadron showers is sampled in the forward region, the HF design must allow narrow and short showers. The front face is located at 11.2 m from the interaction point. The depth of the absorber is 1.65 m. The signal is generated by the Cherenkov light emitted in the quartz fibres, which is then channeled by the fibres to the photomultipliers. The absorber structure is created by machining 1 mm square grooves into steel plates, which are then diffusion welded. The diameter of the quartz fibres is 0.6 mm and they are placed 5 mm apart in the square grid. The fibres, that run parallel to the beam line, have two different lengths (1.43 m and 1.65 m) and are inserted into the grooves creating two effective longitudinal samplings. The two HF modules have 1800 channels.

Jet energy resolution and Missing transverse energy resolution are usually used to gauge the performace of the HCAL. The granularity of the sampling in the 3 parts of the HCAL has been chosen such that the jet energy resolution, as a function of E_T, is similar in all 3 parts. This is illustrated in fig 1.10. The missing transverse energy (E_T^{miss}) resolution is given by $\sigma(E_T^{miss}) = 1.25\sqrt{\Sigma E_T}$,

if energy clustering corrections are not made.

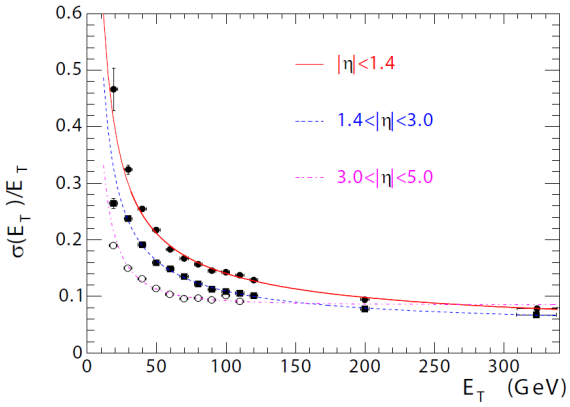

Figure 1.10.: The jet transverse energy resolution as a function of the simulated jet transverse energy for barrel jets ($|\eta|$ <1.4), endcap jets (1.4< $|\eta|$ <3.0) and very forward jets (3.0<$|\eta|$<5.0). The jets are reconstructed with the interative cone R = 0.5 algorithm [1].

1.2.4 Electromagnetic Calorimeter

The electromagnetic calorimeter (ECAL) is a hermetic, homogeneous calorimeter composed of 61200 lead tungstate ($PbWO_4$) crystals mounted in the central barrel part, closed by 7324 crystals in each of the two endcaps (fig 1.11).

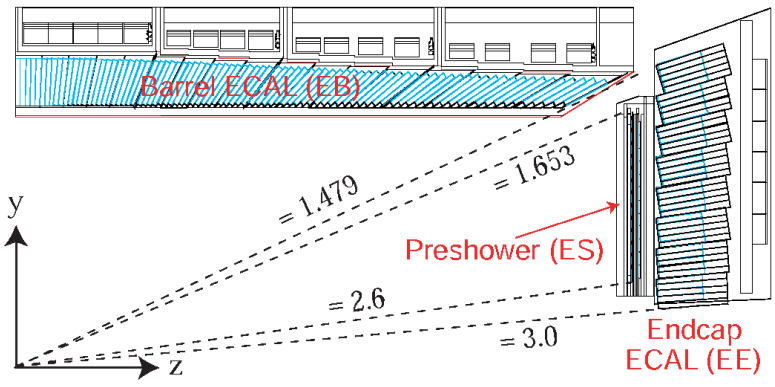

Figure 1.11.: Scheme of the ECAL detector.

The use of $PbWO_4$ has allowed the design of a compact calorimeter inside the solenoid that is fast, has fine granularity and is radiation resistant. These crystals have a small radiation length (X_0 = 0.89 cm) and Moliere radius (2.2 cm),

they are fast (80% of the light emitted within 25 ns) and radiation hard (up to 10 Mrad). They have relatively low light yield (30 γ/MeV), so photodetectors with intrinsic gain that can operate in a magnetic field are needed. Silicon avalanche photodiodes (APD) are used in the barrel, vacuum phototriodes in the endcaps. In addition sensitivity to the temperature changes of both crystals and photodetectors requires temperature stability ($\sim$ 0.1°C).
The barrel section (EB) has an inner radius of 129 cm. It is structured as 36 identical "supermodules" each covering half the barrel length and corresponding to a pseudorapidity interval of $0 < \eta < 1.479$. The crystals are quasi-projective (the axes are tilted of 3° with respect to the line from the nominal vertex position) and cover 0.0174 (i.e. 1°) in $\Delta\phi$ and $\Delta\eta$. The crystals have a face cross-section of $\approx 22 \times 22$ mm^2 and a length of 230 mm, corresponding to 25.8 X_0.
One supermodule is composed of 4 modules as shown in fig 1.12a. Each module is composed of submodules with 5 pairs of crystals contained into a thin walled glass fiber alveola structure (fig 1.12b).

(a) (b)

Figure 1.12.: (a) Photograph of the supermodule, showing the single modules. Each supermodule is composed of 4 modules. (b) Submodule of the ECAL. Each submodule consists of 10 crystals in a glass-fibre alveola structure.

Fig 1.13 presents the resolution, of a barrel supermodule, as a function of the beam energy, measured in a test beam. The energy resolution, measured by fitting a gaussian function to the reconstructed energy distribution, has been parametrized as function of energy:

$$\left(\frac{\sigma}{E}\right)^2 = \left(\frac{S}{\sqrt{E}}\right)^2 + \left(\frac{N}{E}\right)^2 + C^2 \tag{1.1}$$

where S is the stochastic term, N the noise and C the constant term. The values of these parameter are listed in fig 1.13.

The endcaps (EE) are located at a distance of 314 cm from the vertex and cover

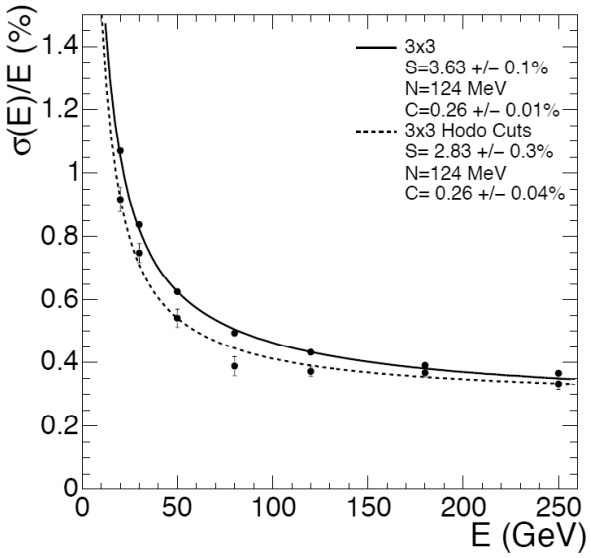

Figure 1.13.: ECAL supermodule energy resolution σ_E/E, as a function of electron energy as measured from a test beam. The upper series of point correspond to events selected to fall in a 20×20 mm^2 region, the lower series correspond to events in a 4×4 mm^2 region. The energy was measured in an array of 3×3 crystals with electrons impacting in the central crystal.

a pseudorapidity range of $1.479 < |\eta| < 3.0$; they are structured as two "Dees", consisting of semi-circular aluminum plates from which are cantilevered structural units of 5×5 crystals, known as "supercrystals". The endcap crystals point away from the nominal vertex position, but are arranged in a x-y grid. They are all identical and have a face cross section of 28.6×28.6 mm^2 and a length of 220 mm (24.7 X_0).
A preshower device is placed in front of the crystal calorimeter over much of the endcap pseudorapidity range. The active elements of this device are 2 planes of silicon strip detectors, with a pitch of 1.9 mm, which lie behind disks of lead absorber at a depth of 2 X_0 and 3 X_0.

1.2.5 INNER TRACKING SYSTEM

The inner tracking system of CMS is designed to provide a precise and efficient measurement of the trajectories of charged particles emerging from the LHC collisions, as well as a precise reconstruction of secondary vertices. It surrounds the interaction point and has a length of 5.8 m and a diameter of 2.5 m. The CMS solenoid provides a homogeneous magnetic field over the

full volume of the tracker. At the LHC design luminosity of 10^{34} cm^{-2} s^{-1} there will be on average about 1000 particles from more than 20 overlapping proton-proton interactions traversing the tracker for each bunch crossing, i.e. every 25 ns. Therefore a detector technology featuring high granularity and fast response is required, such that the trajectories can be identified reliably and attributed to the correct bunch crossing. However, these features imply a high power density of the on-detector electronics which in turn requires efficient cooling. This is in direct conflict with the aim of keeping to the minimum the amount of material in order to limit multiple scattering, bremsstrahlung, photon conversion and nuclear interactions. A compromise had to be found in this respect. The intense particle flux will also cause severe radiation damage to the tracking system. The main challenge in the design of the tracking system was to develop detector components able to operate in this harsh environment. A schematic drawing of the CMS tracker is shown in fig 1.14. The CMS tracker is composed of a pixel detector with three barrel layers at radii between 4.4 cm and 10.2 cm and a silicon strip tracker with 10 barrel detection layers extending outwards to a radius of 1.1 m. Each system is completed by endcaps which consist of 2 disks in the pixel detector and 3 plus 9 disks in the strip tracker on each side of the barrel, extending the acceptance of the tracker up to a pseudo-rapidity of $|\eta|<2.5$. With about 200 m^2 of active silicon area the CMS tracker is the largest silicon tracker ever built.

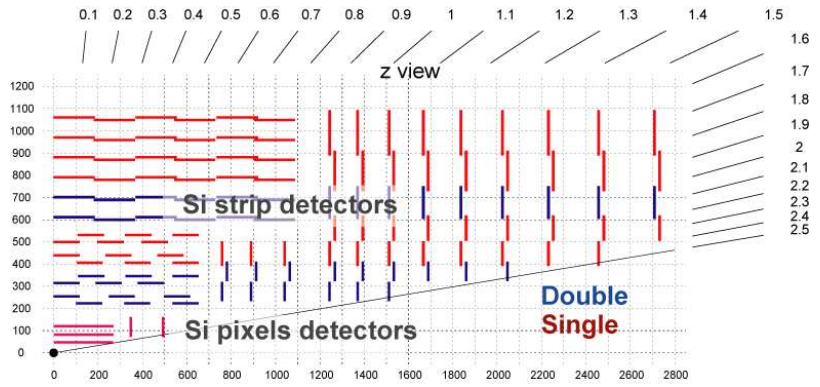

Figure 1.14.: The tracker layout. One quarter in the z view.

STRIP TRACKER

The radial region between 20 cm and 116 cm is occupied by the silicon strip tracker. It is composed of three different subsystems. The Tracker Inner Barrel and Disks (TIB/TID) extend in radius towards 55 cm and are composed of 4 barrel layers, supplemented by 3 disks at each end. TIB/TID delivers up to 4 r-ϕ measurements on a trajectory using 320 μm thick silicon micro-strip sensors

with their strips parallel to the beam axis in the barrel and radial on the disks. The strip pitch is 80 μm on layers 1 and 2 and 120 μm on layers 3 and 4 in the TIB, leading to a single point resolution of 23 μm and 35 μm, respectively. In the TID the mean pitch varies between 100 μm and 141 μm. The TIB/TID is surrounded by the Tracker Outer Barrel (TOB). It has an outer radius of 116 cm and consists of 6 barrel layers of 500 μm thick micro-strip sensors with strip pitches of 183 μm on the first 4 layers and 122 μm on layers 5 and 6. It provides another 6 r-ϕ measurements with single point resolution of 53 μm and 35 μm, respectively. The TOB extends in z between $\pm$118cm. Beyond this z range the Tracker EndCaps (TEC+ and TEC- where the sign indicates the location along the z axis) cover the region 124 cm < |z| < 282 cm and 22.5 cm < |z| < 113.5 cm. Each TEC is composed of 9 disks, carrying up to 7 rings of silicon micro-strip detectors (320 μm thick on the inner 4 rings, 500 μm thick on rings 5-7) with radial strips of 97 μm to 184 μm average pitch. Thus, they provide up to 9 measurements per trajectory.
In addition, the modules in the first two layers and rings, respectively, of TIB, TID, and TOB as well as rings 1, 2, and 5 of the TECs carry a second micro-strip detector module which is mounted back-to-back with a stereo angle of 100 mr in order to provide a measurement of the second co-ordinate (z in the barrel and r on the disks). The achieved single point resolution of this measurement is 230 μm and 530 μm in TIB and TOB, respectively, and varies with pitch in TID and TEC. This tracker layout ensures at least ≈ 9 hits in the silicon strip tracker in the full range of $|\eta| < 2.4$ with at least ≈ 4 of them being two-dimensional measurements (figure 3.2). The ultimate acceptance of the tracker ends at $|\eta| \approx 2.5$. The CMS silicon strip tracker has a total of 9.3 million strips and 198 m^2 of active silicon area. Figure 1.15a shows the material budget of the CMS tracker in units of radiation length. It increases from 0.4 0_0 at $\eta \approx 0$ to about 1.8 0_0 at $|\eta|$ 1.4, beyond which it falls to about 1 0_0 at $|\eta|$ 2.5.

PIXEL DETECTOR

The pixel system is the part of the tracking system that is closest to the interaction region. It contributes precise tracking points in r–ϕ and z and therefore is responsible for a small impact parameter resolution that is important for good secondary vertex reconstruction. With a pixel cell size of 100×150 μm^2 emphasis has been put on achieving similar track resolution in both r–ϕ and z directions. Through this a 3D vertex reconstruction in space is possible, which will be important for secondary vertices with low track multiplicity. The pixel system has a zero–suppressed read out scheme with analog pulse height read–out. This improves the position resolution due to charge sharing and helps to separate signal and noise hits as well as to identify large hit clusters from overlapping tracks.
The pixel detector covers a pseudorapidity range -2.5<η<2.5, matching the

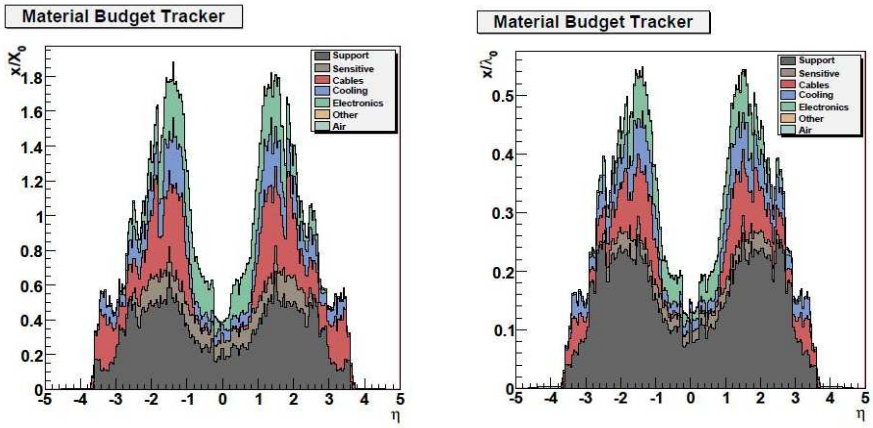

(a) (b)

Figure 1.15.: Material budget as a function of η expressed in terms of radiation length X_0 (a) and in terms of interaction length $\lambda_0 0$ (b). The peak around $|\eta|$=1.5 corresponds to the cables and services of the tracker.

acceptance of the central tracker. The pixel detector is essential for the reconstruction of secondary vertices from b and tau decays, and forming seed tracks for the outer track reconstruction and high level triggering. It consists of three barrel layers (BPix) with two endcap disks (FPix). The 53-cm-long BPix layers will be located at mean radii of 4.4, 7.3 and 10.2 cm. The FPix disks extending from $\sim$6 to 15 cm in radius, will be placed on each side at z=$\pm$34.5 and z=$\pm$46.5 cm. BPix (FPix) contain 48 million (18 million) pixels covering a total area of 0.78 (0.28) m^2. The arrangement of the 3 barrel layers and the forward pixel disks on each side gives 3 tracking points over almost the full η–range. The vicinity to the interaction region also implies a very high track rate and particle fluence that require a radiation tolerant design. For the sensor this led to an n+ pixel on n-substrate detector design that allows partial depleted operation even at very high particle fluence. For the barrel layers the drift of the electrons to the collecting pixel implant is perpendicular to the magnetic field of CMS. The resulting Lorentz drift leads to charge spreading of the collected signal charge over more than one pixel. With the analog pulse height being read out a charge interpolation allows to achieve a spatial resolution in the range of 15–20 μm. The forward detectors are tilted at 20° in a turbine-like geometry to induce charge-sharing. The charge-sharing is mainly due to the geometric effect of particles entering the detector at an average angle of 20° away from normal incidence; charge-sharing is also enhanced by the $\vec{E} \times \vec{B}$ drift. A position resolution of approximately 15 μm in both directions can be achieved with charge-sharing between neighbouring pixels. The reduction in the depletion depth or the increase in bias voltage will lead to a reduction of

charge-sharing and therefore a degradation of the spatial resolution with radiation damage.
In order to allow a replacement of the innermost layers the mechanics and the cabling of the pixel system has been designed to allow a yearly access if needed. At full LHC luminosity we expect the innermost layer to stay operational for at least 2 years. The 3 layer barrel mechanics as well as the forward disks are divided into a left and a right half. This is required to allow installation along the beam pipe and to pass beyond the beam pipe support wires at z=$\pm$1632 mm.The 6 individual mechanical pieces are referenced to each other through precisely machined rails inside the TIB cylinder. Power, cooling, the optical controls as well as the optical read-out lines are brought to the detector through supply tube shells. In case of the barrel pixel system the supply tubes have a flexible connection that needs to bend by a few degrees during insertion following the slightly curved rails around the beam pipe support ring.
The pixel system is inserted as the last sub-detector of CMS after the silicon strip tracker has been installed and after the central section of the beam pipe has been installed and baked out.

1.3 THE CMS TRIGGER

The LHC provides proton-proton collisions at a crossing frequency of 40 MHz. Depending on luminosity, several collisions occur at each crossing of the proton bunches (approximately 20 simultaneous p-p collisions at the nominal design luminosity of $10^{34}\mathrm{cm}^{-2}\mathrm{s}^{-1}$).
Since it is impossible to store and process the large amount of data associated with the resulting high number of events, a drastic rate reduction has to be achieved. This task is performed by the trigger system, which is the start of the physics event selection process.
The rate is reduced in two steps called Level-1 (L1) Trigger [5] and High-Level Trigger (HLT) [6], respectively. The Level-1 Trigger consists of custom-designed, largely programmable electronics, whereas the HLT is a software system implemented in a filter farm of about one thousand commercial processors.
The rate reduction capability is designed to be at least a factor of 10^6 for the combined L1 Trigger and HLT. The design output rate limit of the L1 Trigger is 100 kHz, which translates in practice to a calculated maximal output rate of 30 kHz, assuming an approximate safety factor of three.
The L1 Trigger uses coarsely segmented data from the calorimeters and the muon system, while holding the high-resolution data in pipelined memories in the front-end electronics. The HLT has access to the complete read-out data and can therefore perform complex calculations similar to those made in the the analysis off-line software if required for specially interesting events.

1.3.1 L1 TRIGGER

For reasons of flexibility the L1 Trigger hardware is implemented in FPGA technology where possible, but ASICs and programmable memory lookup tables are also widely used where speed, density and radiation resistance requirements are important.
A software system, the Trigger Supervisor [7], controls the configuration and operation of the trigger components. The L1 Trigger has local, regional and global components. At the bottom end, the Local Triggers, also called Trigger Primitive Generators, are based on energy deposits in calorimeter trigger towers and track segments or hit patterns in muon chambers, respectively.
Regional Triggers combine their information and use pattern logic to determine ranked and sorted trigger objects such as electron or muon candidates in limited spatial regions. The rank is determined as a function of energy or momentum and quality, which reflects the level of confidence attributed to the L1 parameter measurements, based on detailed knowledge of the detectors and trigger electronics and on the amount of information available.
The Global Calorimeter and Global Muon Triggers determine the highest-rank calorimeter and muon objects across the entire experiment and transfer them to the Global Trigger, the top entity of the Level-1 hierarchy. The latter takes the decision to reject an event or to accept it for further evaluation by the HLT.
The decision is based on algorithm calculations and on the readiness of the subdetectors and the DAQ, which is determined by the Trigger Control System. The Level-1 Accept decision is communicated to the sub-detectors through the Timing, Trigger and Control system.
The architecture of the L1 Trigger is depicted in figure 1.16. The L1 Trigger has to analyze every bunch crossing. The allowed L1 Trigger latency, between a given bunch crossing and the distribution of the trigger decision to the detector front-end electronics, is 3.2 μs[3]. The processing must therefore be pipelined in order to enable a quasi-deadtime-free operation.
The L1 Trigger electronics is housed partly on the detectors, partly in the underground control room located at a distance of approximately 90 m from the experimental cavern.

1.3.2 HIGH LEVEL TRIGGER

The CMS DAQ/HLT processes all events accepted by the Level-1 trigger in a single processor farm. There is therefore no separate Level-2 or Level-3, but a single entity, the High-Level Trigger. Nevertheless, as in a traditional multi-level trigger system, the selection of events can be optimized by rejecting events as quickly as possible.
The basic event building strategy is to reconstruct those parts of each physics object that can be used for selection while minimizing the overall CPU usage. As an example, reconstruction of an electron includes the reconstruction of a

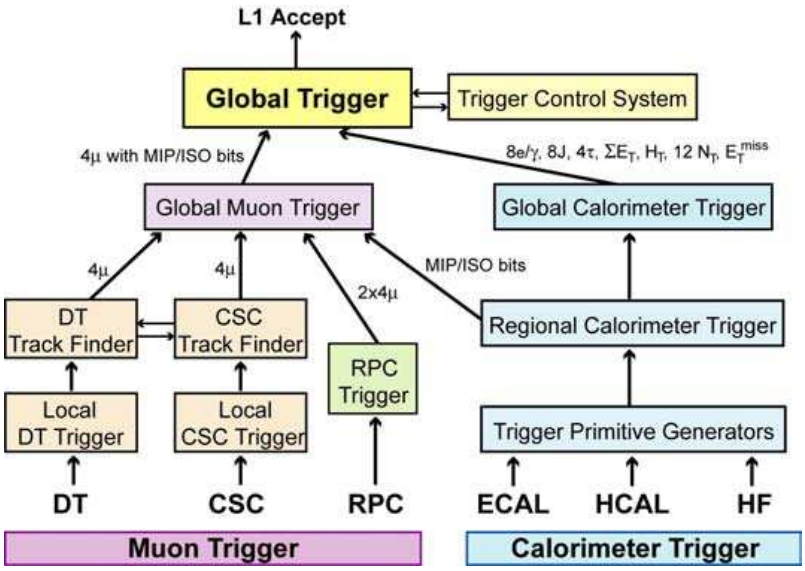

Figure 1.16.: Architecture of Level-1 Trigger [3]

cluster in the electromagnetic calorimeter, the matching of hits in the pixel detector and the subsequent reconstruction of a full charged particle track in the tracker.

At the end of each step a set of selection criteria results in the rejection of a significant fraction of the events accepted by the previous step. The rate of events that need to be processed through the remaining algorithms is decreased reducing the required CPU.

Reconstruction and selection are therefore closely intertwined in the online environment of the filter farm. For an optimal system the HLT should reconstruct the minimum amount of detector information needed to apply a set of selection criteria that reject background events while keeping the desired physics events for further processing.

The reconstruction and selection in the HLT takes place in steps which correspond roughly to what would have been distinct trigger systems, the Level-2 and Level-3 trigger systems. It is thus convenient to use the terminology, and to refer to a “Level-2 trigger”, algorithms and requirements refer to the first selection step in the HLT process, or a “level-3 step” to describe the selection algorithms and criteria of the HLT. As mentioned previously the CMS HLT architecture does not include a sharp division between these trigger steps, other than the order in which they are applied. Typically, a Level-2 trigger, which has the maximum rate of events input to it, uses only information from the calorimeter and muon detectors. In contrast, “Level-3” refers to selection that includes the reconstruction of full tracks in the tracker. Traditionally, because of the high number of channels, the complex pattern recognition and higher combinatorics, track reconstruction is a process that demands large amounts of CPU time.

Extending the terminology, in what follows there are references to “Level-2.5” triggers,which refer to algorithms that use partial tracker information, e.g. pixel hits, for a fast confirmation of the electron candidate. The numbering,“2.5”, attempts to indicate the intermediate nature of the selection, as one that occurs between the selection that is based solely on the calorimeter information, and the selection that is based on the full CMS detector information.
The performance of the HLT have been tested by running the full set of algorithms on simulated QCD events and on several signal like events. Both test yield an average time per L1-accepted event of (42.9 ± 5.6) ms, which is consistent with the capabilities of the Filter Farm [8].

CHAPTER 2

PERFORMANCE OF IRRADIATED CMS FORWARD PIXEL DETECTOR

The CMS physics program requires a precise measurement of secondary vertices and impact parameters, achieved by a tracker extending as closely as possible toward the interaction point. Owing to the extremely high particle flux at small distances, the innermost tracking layers are composed of pixel devices produced with radiation-tolerance rules to survive for several years in the harsh environment. To study the long term performance, a forward pixel detector element, previously irradiated up to 45 Mrad, was tested on a beam at Fermilab. In this chapter, after the description of the detector and test-beam setup, the results are presented and discussed.

2.1 FORWARD PIXEL DETECTOR

The CMS pixel detector covers the pseudorapidity region $|\eta| < 2.5$, matching the acceptance of the strip tracker. The pixel cell size of 100×150 μm^2 has been chosen to provide high resolution 3D space points close to the interaction point for precise vertex determination and fine granularity for charge pattern recognition.
The pixel system consists of three barrel layers (BPix) and two end cap disks (FPix) at each end of the barrel pixel detector (see figure 2.1).
The axial length of the three barrel elements is ~ 50 cm and their radii 4.4, 7.3 and 10.2 cm. The four disks are at $\pm$34.5 and $\pm$46.5 cm from the barrel center at the collision point and their inner and outer radii are 6.1 and 15.0 cm, respectively.
The forward pixel modules, called plaquettes, are arrays of different numbers of Read Out Chips (ROCs) bump-bonded to a single Si sensor of n^+/n type. The ROCs, designed by Horisberger's group at PSI, provide an analog readout

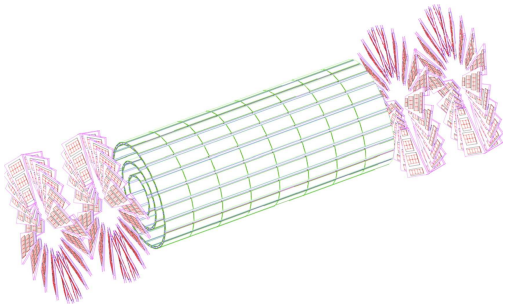

Figure 2.1.: A sketch of the CMS pixel detector with the three layers of the barrel detector and the four disks of the forward detector

of the collected charge and were produced with commercial 0.25μm CMOS technology with radiation-tolerant design rules [9].
Each ROC serves a matrix of 52×80 sensor pixel cells and is bump-bonded to the sensor with the PbSn solder technology. The Si sensors, produced by SINTEF, employ a partially open p-stop isolation technology, are 270μm thick and typically present a depletion voltage of around 50 V and a breakdown voltage well above 500 V. Details of the pixel sensors are shown in figure 2.2 [10].
These pixels consist of high dose *n*-implants introduced into a high resistance *n*-substrate. The rectifying *pn*-junction is placed on the back side of the sensor surrounded by a multi guard ring structure. This concept was chosen as the collection of electrons ensures a high signal charge at moderate bias voltages (< 600 V) after high hadron fluences.

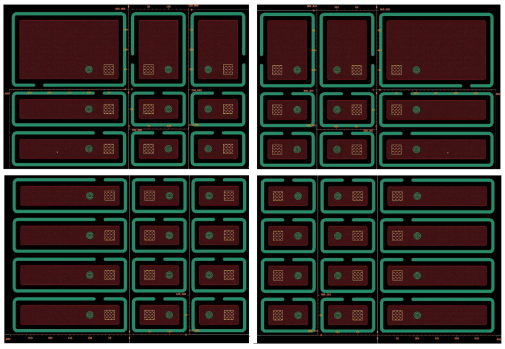

Figure 2.2.: The detailed design of a forward pixel sensor at the four corners of each ROC. In green are the p-stop rings around the pixel implants.

In fact, these detectors are expected to integrate a maximum dose of about 7 Mrad per year on the inner edge of the first disk at the full LHC design luminosity of 10^{34} cm^{-2}s^{-1} at 14 TeV center-of-mass energy. At higher radius, the integrated dose per year should decrease as $\sim r^{-1.8}$ [11].
This high radiation induces bulk damages on the detector: non-ionizing energy

loss causes modifications to the silicon crystal lattice and leads to additional energy levels in the band gap. The consequences are an increase of the leakage current, a change in the doping from *n*- to *p*-type with a corresponding change in depletion voltage (even a few hundred volts over the lifetime of the tracker) and the creation of additional trapping centers which will reduce the signal.
To study the effects of the high dose on the forward pixel detector performance, a pre-production plaquette of 2×4 ROCs was exposed to a peak dose of 45 Mrad at the Indiana University Cyclotron Facility using a 200 MeV proton beam.
During the irradiation, the beam was centered on one edge of the plaquette to produce a highly non-uniform dose profile similar to that expected in the CMS experiment. The irradiation beam was roughly Gaussian in shape with $\sigma \sim 2$ cm and 1.6×10^{15} n_{eq}/cm^2 peak-fluence[1]. The geometry and characteristics of the irradiation are clearly illustrated in figure 2.3.
Once completed the irradiation process, the plaquette was kept in a refrigerator at low temperature to avoid any annealing effect and was then tested on the test-beam at Fermilab.

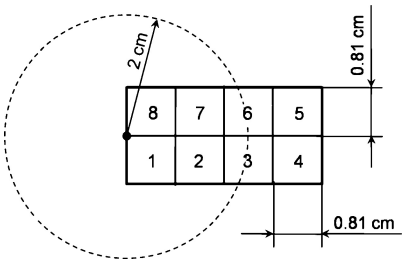

Figure 2.3.: The 2×4 irradiated plaquette. The numbers indicate the eight ROCs bump-bonded on the underlying sensor and the circle the position and the 1σ radius of the 200 MeV proton beam during the irradiation

2.2 EXPERIMENTAL SETUP

The tests were performed at the M-test facility at Fermilab with a 120 GeV proton from the Tevatron main injector.
The experimental setup was chosen in order to fully characterize the detector under test as far as charge collection, detection efficiency and charge sharing are concerned. For this reason, a silicon telescope has been used, capable of reconstructing the tracks with a precision of 4.9 μm in the x direction and 6.2 μm in the y direction.
The telescope is composed of 6 planes of pixel detectors [12] from the BTeV

[1] n_{eq} 1 MeV neutron equivalent

experiment, with a 50 μm $\times$ 400 μm pixel size, arranged in two sections. The first and the last plane of the telescope are placed with the 50 μm pixel side oriented in order to measure the vertical (y) coordinate, while all the others were oriented to measure the horizontal coordinate (x) with the small pixel side.
The planes are rotated of $\sim 10°$ to achieve an optimal resolution. The x-planes are rotated of an angle β along the y-axis, while the y-planes are rotated of an angle α around the x-axis. The detector under test was positioned in the middle and it was always in the plane orthogonal to the beam.
The trigger for the CMS detector was provided by the coincidence of two scintillator counters upstream the telescope, as in figure 2.4, while the telescope detectors don't need a trigger. An ad hoc data acquisition system based on FP-

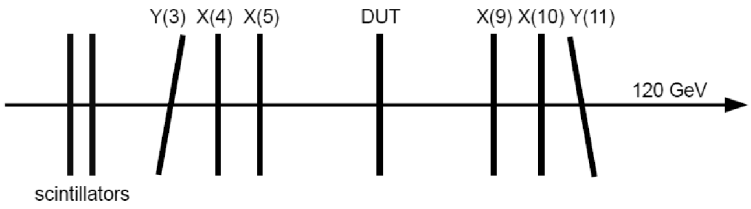

Figure 2.4.: Schematic drawing of the testbeam telescope.

GAs [13], was developed to readout simultaneously the two types of devices and to build the events on the basis of a common time-stamp value. Syncronization was obtained by clocking the readout electronics with the accelerator radiofrequency, which was divided by two for instrumental reasons, 26.5 MHz = 53 MHz/2.

2.3 RESULTS

The testbeam investigates the performance of three regions of the detector at three different levels of irradiation. The results are compared with those of a non-irradiated single ROC plaquette, used as reference. In the following paragraphs, the text refers to this plaquette as ROC0 and to the different region of the 2×4 module with ROC1, ..., 8 as labeled in figure 2.3.
The information of the charge released in the sensor is stored in a 6 bit ADC. All the pixels were electronically calibrated using the internal calibration circuitry, which injects a known amount of charge into the pixel preamplifier input. Figure 2.5a reports the ADC count as a function of VCal unit (1 VCal = 60 e^-), fitted with an hyperbolic tangent. A calibration table is obtained calculating the numerical inverse of the function for each ADC unit and for each pixel. Figure 2.5b shows the VCal value vs ADC obtained from the fit in figure 2.5a. The accuracy of the calibration is of the order of 8%.
A common threshold was set for each ROC by choosing the lowest value at

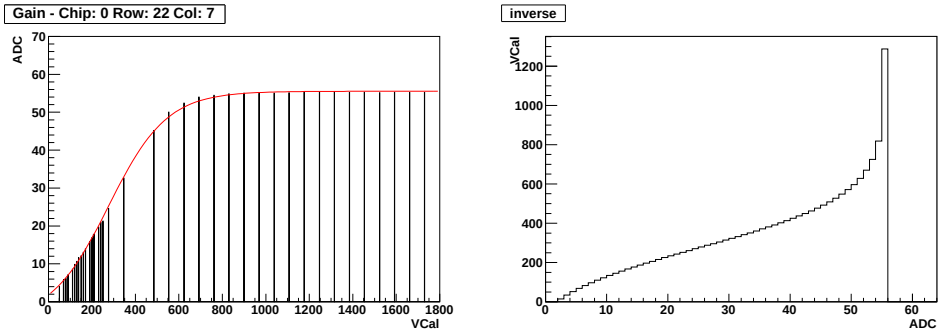

(a) (b)

Figure 2.5.: Gain curve fit and calibration histogram for the pixel in row 22 and column 7 in ROC0.

which the ROC was still practically immune from noise. Unfortunately our setup configuration was not optimal to allow for operation at low threshold. No fine tuning was done to equalize the thresholds on each channel: the resulting dispersion around the central value is about 10%. The final threshold setting was $\sim 3800\ e^-$ for the reference detector and $\sim 3300\ e^-$ for all the ROCs on the irradiated plaquette.

The bias voltage was set at 200 V for the reference detector and at the maximum allowed by the power supply, 500 V, for the plaquette. Figure 2.6 shows the peak position of the charge release by a minimum ionizing particle (MIP) as a function of the applied bias voltage. It clearly indicates that the first value is well above the depletion voltage, while the latter one is just below the depletion for the most irradiated region of the plaquette, corresponding to the ROC 8.

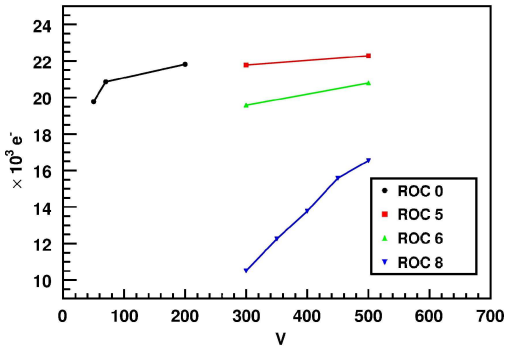

Figure 2.6.: MIP peak position at different bias voltages for the reference detector, ROC0 and three regions of the irradiated detector, ROC5, ROC6 and ROC8.

2.3.1 COLLECTED CHARGE

One of the conseguences of radiation damage is a reduction of the signal in the detector, because of the creation of additional trapping center in the silicon substrate or beacuse of the incomplete charge collection in case of partially depleted detector. Thus, the first study on the testbeam data concerns the collected charge, which is shown in figure 2.7 for the four ROCs studied in detail, namely ROC0, ROC5, ROC6 and ROC8.

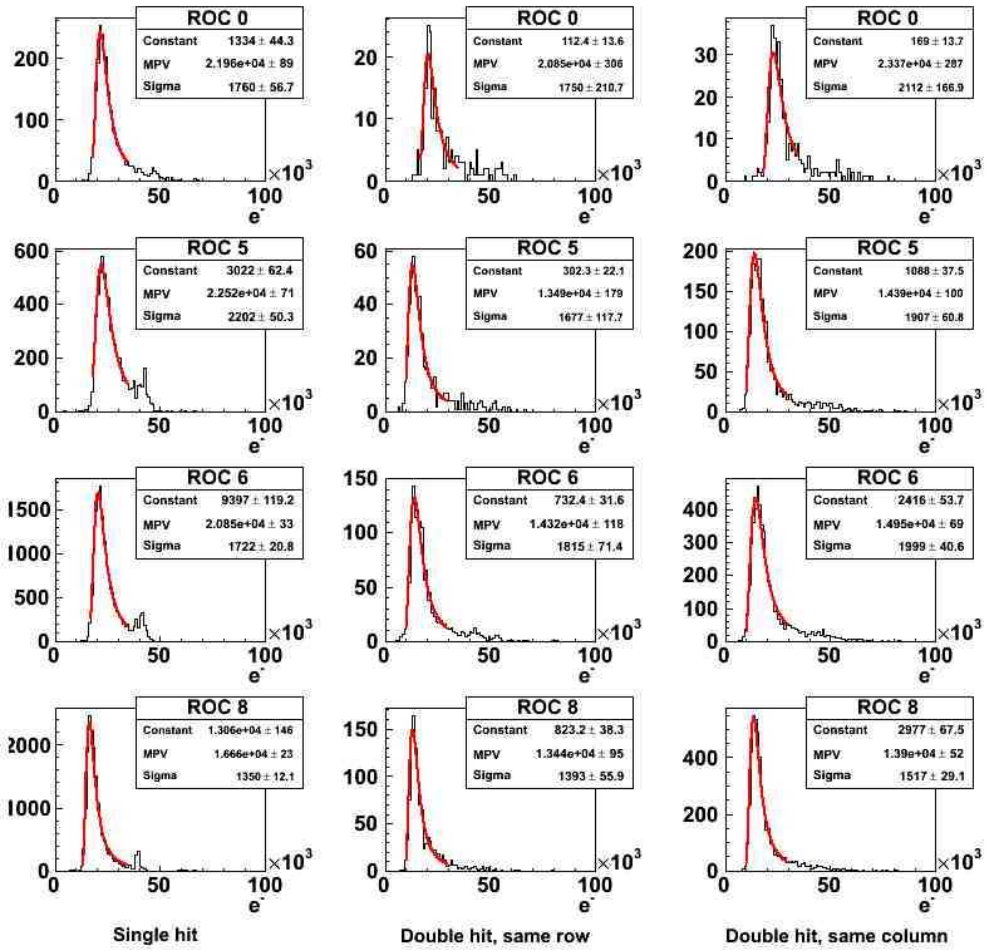

Figure 2.7.: Collected charge for the four ROCs under study.

The events are divided in tree classes to analyse separately the region of the sensor with different electric field configurations. The considered categories are: single hit events, double hit with the two active pixels on the same row and with the two pixel on the same column. Adjacent pixels on the same row and on the same column has to be considered separately because of the asymmetry in the p-stop ring.
The single-hit spectra, on the first left column, show the charge collected by

the sole pixel pointed by the telescope track when the impact point of the track is within the pixel-cell boundaries by at least 20 μm in X and 30 μm in Y. The asymmetry in this selection cut is simply due to the different resolution provided by the telescope track along X and Y-coordinates.
By way of contrast, when ever the track impact point is close to an edge by more than 20 μm in X or 30 μm in Y, but not simultaneously (to exclude the corner regions), the sum of the charges collected by the pointed pixel and the adjacent pixel is plotted in the central-column histograms, if the two adjacent pixels were on the same row, or in the right-column histograms, if they were on the same column. In either case, both of the involved pixels are required to have a signal above the threshold.
The fits for this spectra were obtained using the Landau distribution function available in the ROOT package. The most probable value and sigma results from fit are in table 2.1.

		Single-hit	Double-hit, same row	Double-hit, same column
ROC0	MPV (e^-)	21950±88	20630±295	23260±243
	$\sigma(e^-)$	1755±56	1616±201	1890±200
ROC5	MPV (e^-)	22520±70	13320±167	14340±97
	$\sigma(e^-)$	2198±50	1537±101	1857±59
ROC6	MPV (e^-)	20860±32	14310±114	14920±67
	$\sigma(e^-)$	1719±21	1777±74	1963±40
ROC8	MPV (e^-)	16680±22	13360±89	13900±50
	$\sigma(e^-)$	1311±13	1326±58	1490±31

Table 2.1.: Charge collection fit results

The resulting picture is that the region of sensor furthest away from the dose peak, ROC5, can still collect all the released charge, provided it is not shared between adjacent pixels. As soon as we move toward the most irradiated region, the reduced carrier lifetime limits the charge-collection efficiency and lowers the Landau peak to about 93% of the expected value at ROC6 and about 75% at ROC8.
A further degradation of the signals is evident whenever more than one pixel is involved in the charge-collection process. In this case the amount of charge collected by two adjacent pixels on the same column is systematically larger than that collected by two pixels on the same row. This difference is due to the break on the p-stop ring in the region between any adjacent pixels on the same column. The interruption of the p-stop, indeed, increases locally the charge collection efficiency.
There is also a clear indication that the percentage of lost charge with respect to that of the single hits diminishes moving toward the most irradiated ROC8,

from $\sim 41\%$ to $\sim 20\%$ in case of sharing between pixels on the same row. This means that, at high radiation doses, the charge collection efficiency in the region between pixels decreases with a much lower rate than near the center of the pixels. This could be attributed to the drastic changes of the electric-field expected at high radiation-doses. Indeed, the formation of a new junction on the n+ side, as a result of the type-inversion mechanism, radically changes the field configuration between adjacent pixel-implants.
The charge-collection features are further investigated in figure 2.8. Here, the average collected charge is plotted as a function of the signed distance of the track impact-point from the boundary of two adjacent pixels on the same column (figure 2.8, left column) and on the same row (figure 2.8, right column). To avoid additional sharing with other pixels, the track impact point is required to stay well within the column edges in the former case and the row edges for the latter. The usual fiducial cut of 20 μm in X or 30 μm in Y was applied.
The two types of data points refer to the charge collected by the sole pixel pointed by the track (black points) and the sum of charges collected by the two adjacent pixels (red points). Asymptotic point, far away from the divide, correspond to single hit events.
It turns out that the total amount of charge collected by ROC0 shows a marginal deficit (a few percent) in crossing the region between two adjacent pixels, where as the one collected by the irradiated detector shows a clear drop, reaching about 40% of the asymptotic (far from zero) value in the worst case. Also in this case, there is a clear evidence for an asymmetry in charge loss when comparing sharing between two pixels on the same column, that presents higher collection efficiency, and on the same row.

2.3.2 DETECTION EFFICIENCY

The second step of the study concerns the detection efficiency. Precise track and vertex reconstruction requires at least two hits in the pixel system. These reconstructed objects are the basilar components for the physics analysis. Thus, an excellent detection efficiency of the pixel detector even after several year inside the LHC is of major importance.
The detection efficiency is investigated in figure 2.9. As explained for the charge-collection study, the detection efficiency is plotted as a function of the signed distance of the track impact point from the boundary of the two adjacent pixel on the same column (figure 2.9, left column) and on the same row (figure 2.9, right column).
The usual fiducial cuts were applied to exclude additional sharing with other pixels.
Also here,the two types of data points refer to the sole efficiency of the pixel pointed by the track (black points) and the combined efficiency of the two adjacent pixels (red points). The combined efficiency is constant and does not show any appreciable degradation even in the region between pixels. The asymptotic

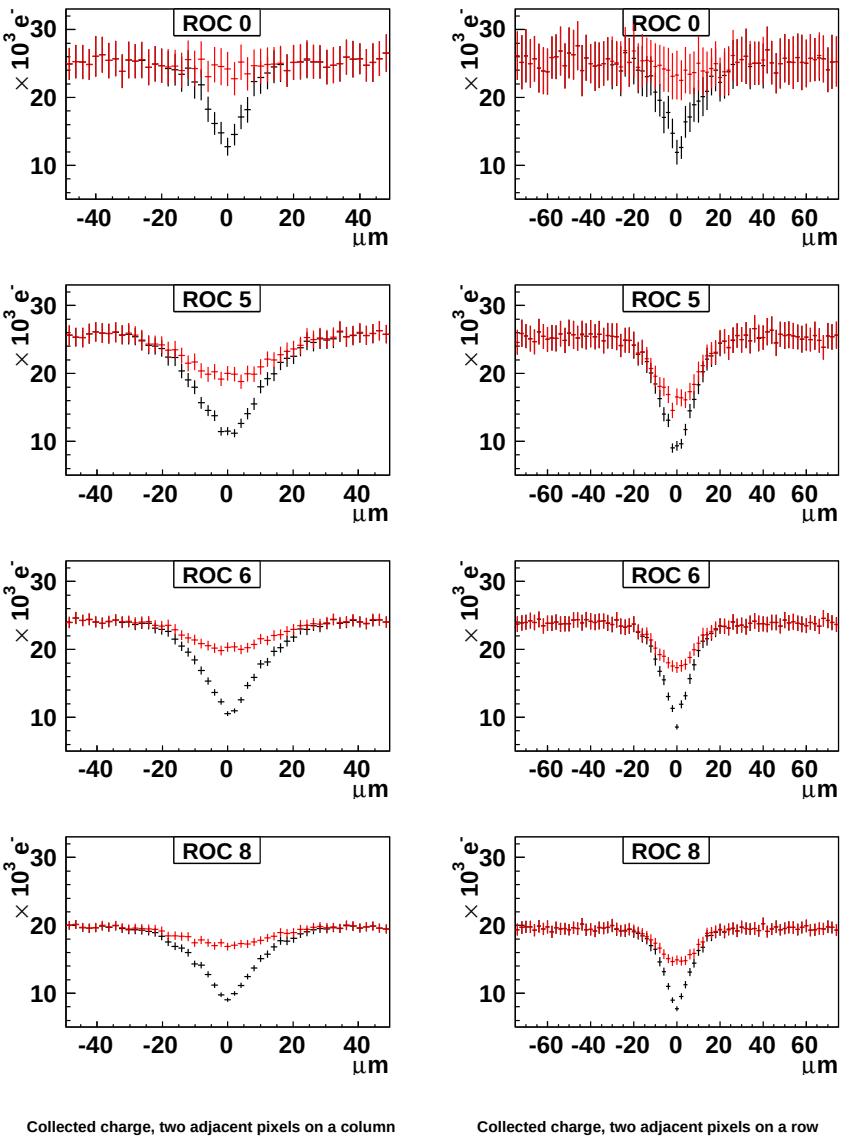

Figure 2.8.: Collected charge as a function of the distance of the track impact point from the boundary of the two adjacent pixel on the same column (histograms on the left), or on the same row (histograms on the right).

efficiency, away from the pixel edge, reaches a value around 99%, fully consistent with 100%, given the 1% systematic inefficiency of our apparatus when two or more beam particle are in the same time-stamp window.
Because of the protection built in our trigger logic, the CMS detector is blind for ~ 4 μs after a trigger. If the first particle fires the trigger but it is outside the telescope acceptance, no track will be reconstructed. In case the second

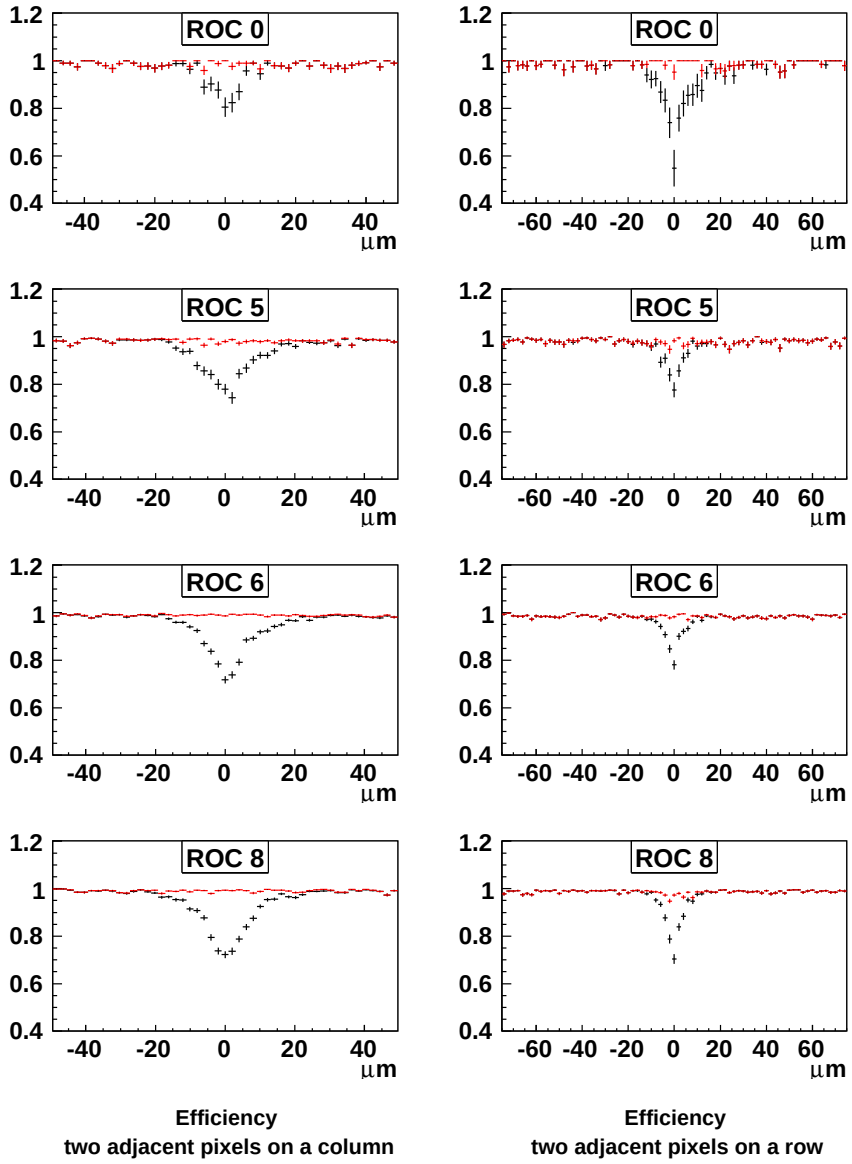

Figure 2.9.: Detection efficiency as a function of the distance track impact point from the boundary of the two adjacent pixel on the same column (histograms on the left), or on the same row (histograms on the right)

particle is detected by the BTeV pixel planes but it arrives outside the 38 ns readout gate of the CMS device, no signal will be read on this last detector. In conclusions, this small inefficiency is just an apparent effect generated by a sequence of two particle at least, which fall in the same time stamp windows (500 ns) but not in the CMS readout gate.

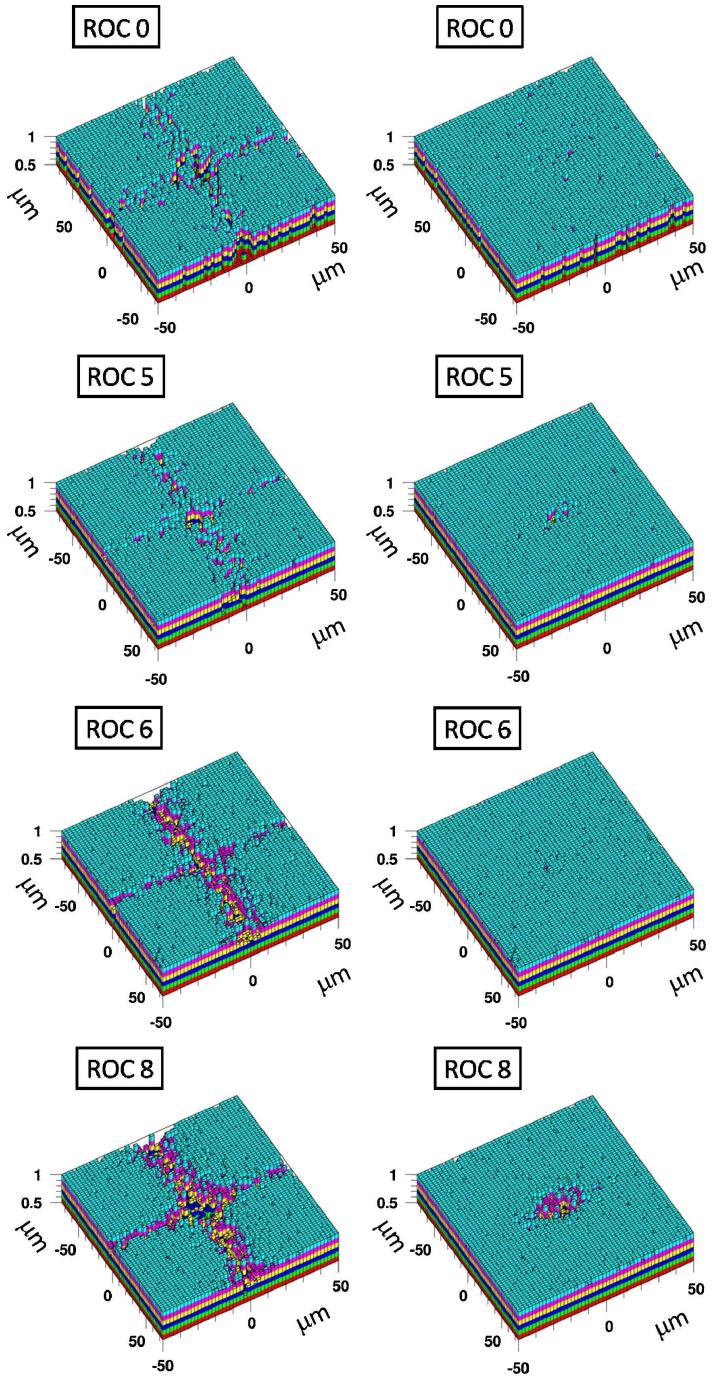

Figure 2.10.: The detection efficiency as a fuinction of the coordinates of the track impact point. On the left plots the efficiency of the sole pixel pointed by the track, on the right ones the combined detection efficiency of the four nearby pixels

Figure 2.10 shows the complete two-dimensional point detection efficiency.

Here, the efficiency of the single pixel pointed by the track is plotted together with the combined detection efficiency of the four nearby pixels. In the plots on the lefts the drops are due to the impact point uncertaninty derived from the track resolution. In fact, it is evident the difference of the resolution in the X and Y direction.
For the plots of the four pixel combined efficiency (right plot), the inefficiency is confined near the corners of the pixels, where the fractions of signal collected by the single pixels are small and could easily fall below the threshold or outside the synchronization time-window because of time-walk. The resulting global detection efficiency, summarized in table 2.2, remains very high, close to $\sim 99\%$, given the $\sim 1\%$ systematic detection inefficiency of our readout system.

ROC0	98.61±0.15 %
ROC5	97.69±0.10 %
ROC6	98.78±0.05 %
ROC8	97.46±0.06 %

Table 2.2.: Global detection efficiencies

2.3.3 CHARGE SHARING

In addition to the creation of trapping centers, the non ionizing energy loss eventually changes the substrate doping from *n*-type to *p*-type. The formation of a new junction on the n^+ side, as a result of the type-inversion, radically changes the field configuration between adjacent pixel-implants and, thus, the charge collection in the region.
The next step of the performance study analyzes the charge-sharing correlation between two adjacent pixels, plotted in figure 2.11 for cells belonging to the same column (plots on the left) and the same row (plots on the right). The two axes represent the amount of charge collected in each event by the two adjacent pixels respectively. Fiducial cuts were applied to exclude the corner regions as for the charge collection study in figure 2.8. The well-behaved characteristic exhibited by the non-irradiated detector deteriorates as one moves toward the most irradiated region corresponding to ROC8.
The second study is the position resolution achievable in case of charge-sharing between two adjacent pixels, which was investigated using the variable

$$\eta = \frac{Q_r}{Q_l + Q_r},$$

where Q_l is the charge collected by the pixel on the left side and Q_r that on the right side of their interface.
The distribution of measured η is shown in figure 2.12 for two pixels on the

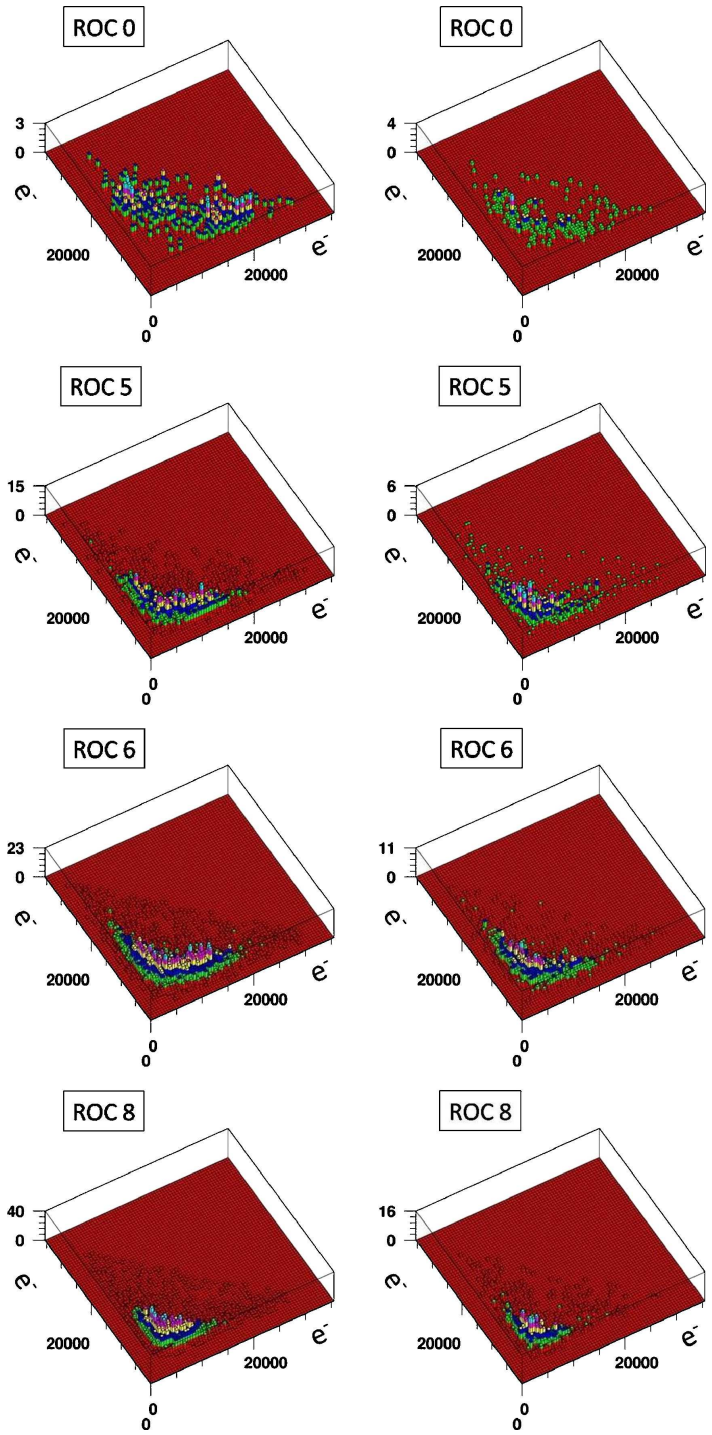

Figure 2.11.: The measured charge-sharing correlation between two adjacent pixels on the same column (plots on the left) or the same row (plots on the right).

same row (left plots) and on the same column (right plot) of the four ROCs. The fiducial cuts used for these distributions are exactly the same as those for

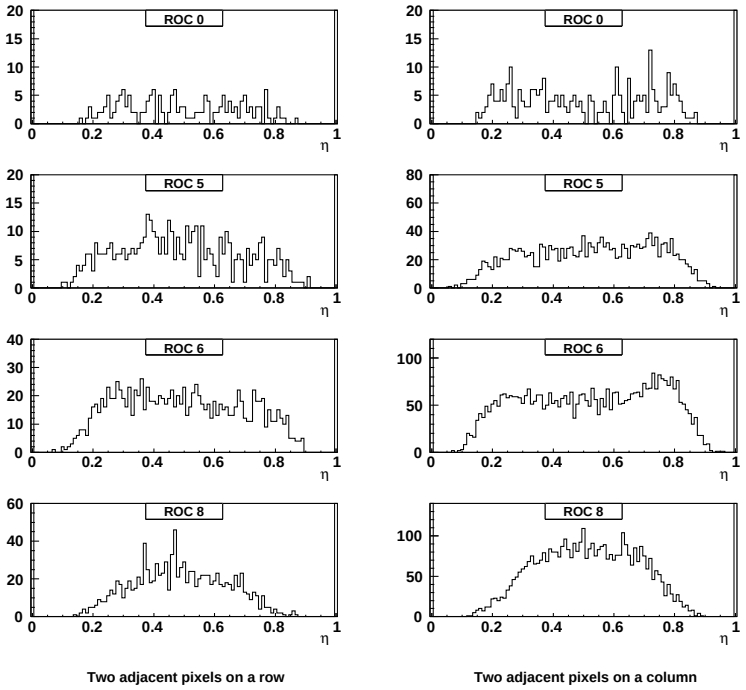

Figure 2.12.: The measured η-spectrum for the two adjacent pixel on the same row and on the same column for the four ROCs

figure 2.8: 30 μm in y for the left plots and 20 μm in x for those on the left.
The peaks at 0 and 1 are due to events with one hit only on the left or right pixel respectively, i.e., no shared charge.
The gap between the central portions of the distributions and the two peaks at 0 and 1, respectively, is caused by the threshold cut. In addition, the continuous effective increase of the threshold value, due to the loss of collected charge (as observed in figure 2.8), shrinks the central portion of the η-distribution when moving toward the most irradiated regions.
The slight asymmetry with respect to the central η-value, present, at high radiation doses, in the distributions for adjacent pixels on the same row, cfr ROC6 on the left, is due to the non-perfect orthogonality of the detector to the beam tracks. The plaquette was at an angle of about 60 mrad around X and 50 mrad around Y from the orthogonal plane. These angles tilt the flat portion of the η-distributions when the charge-collection efficiency drops moving away from the pixel electrodes as for irradiated sensors.
Another effect is an evident excess of population on the right side of η-distributions for pixels belonging to the same column on ROC6. Here, the effects of the non-orthogonality to the beam are superimposed with those due to the

p-stop break, which further unbalances the charge-sharing in favor of the pixel on the right. To support this explanation, a study was conducted isolating the tracks impinging in the region corresponding to the p-stop breaks. It was found that the asymmetry of the resulting η-distribution becomes much larger (see figure 2.13a) and that, on the complementary area, tends to vanish (see figure 2.13b).

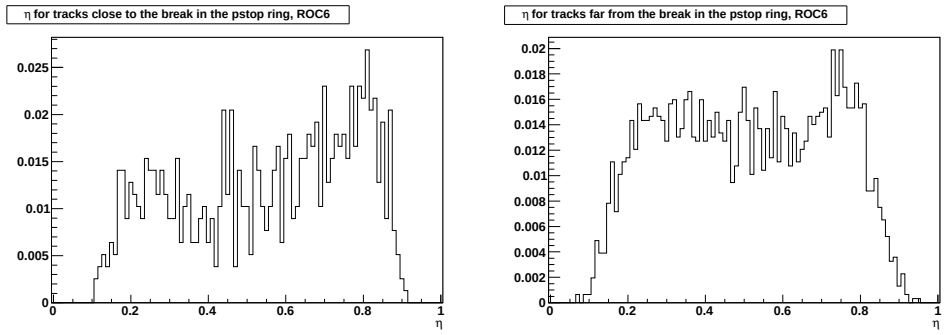

(a) (b)

Figure 2.13.: (a) η for tracks impinging in the region corresponding to the p-stop breaks ($\pm 10\mu$m from the pixel center in x direction), (b) η on the complementary area

The same kind of asymmetry, though at a lower level, is also present on ROC5. On ROC8, the most irradiated one, the potentially huge excess disappears simply because it is cut out by the high effective value of the threshold. Also in this case, in a completely analogous way with what we found for the collected charge distributions, we observe an effect which becomes stronger at higher absorbed doses and indicates a relative effective increase of the charge-collection efficiency in the region between adjacent pixels.

The last step of the charge sharing study is about the correlation between the track impact point distance from the two-pixel interface and the measured η-value. This is important because it is strictly connect with the point determination in local reconstruction. A corrupted characteristics will bias the starting points of the global tracking leading to a deterioration in track and vertex quality.

In figure 2.14, with the usual meaning of the eight plots, the mean value of the signed distance of the track impact points within a certain η-bin was directly computed.

The same correlation was also investigated using an indirect method, which relies on the assumption that, on average, a higher η-value corresponds to a higher signed distance, x, from the pixel interface. In this case, one can easily demonstrate that the signed distance for a certain value of η, $x(\eta)$, is given by:

$$\int_{-p}^{x(\eta)} \frac{dN_x}{dx} dx = \int_0^{\eta} \frac{dN_\eta}{d\eta} d\eta$$

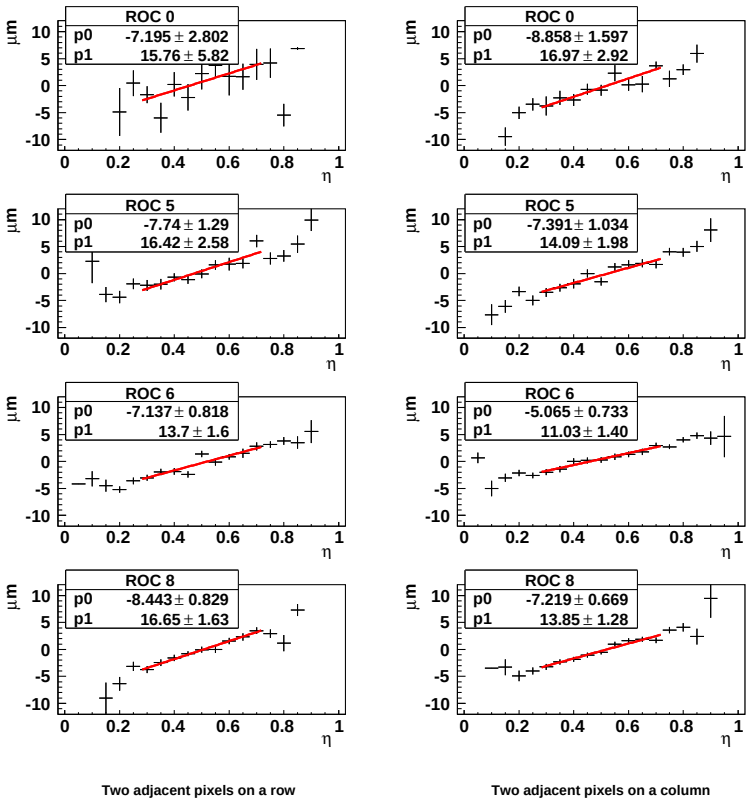

Figure 2.14.: The measured correlation between the track impact point distance from the two pixel interface and the measured η-value. The histograms on the left are for adjacent pixels on the same row, those on the right for adjacent pixels on the same column.

where p stands for one half the pitch in x direction, dNx/dx is the distribution of the signed distances, x, of the track impact point and $dN_\eta/d\eta$ that of the measured η.
The resulting correlation plots are shown in figure 2.15.
The two correlation plots obtained with the two methods substantially match each other, no drastic distorsion of the correlation characteristics and no important reduction of the charge sharing region has been observed.

2.3.4 CLUSTER SIZE

As already seen for the case of two adjacent pixels, the reconstructed position of the track hits on the pixel detector depends, in general, on the spatial distribution of the collected charge, which is directly related with the number of hits in the cluster. Losses in efficiency due to radiation damage can bias the reconstruction of the track impact point, causing a deterioration of the tracking efficiency and an increase in the fake rate. Therefore, the study of the cluster

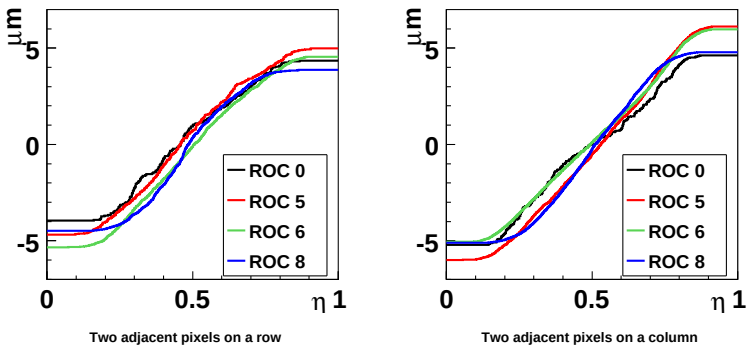

Figure 2.15.: The correlation between the track impact point distance from the two pixel interface and the measured η-value obtained by the indirect method described in the text. As for figure 2.14, the plots on the left are for adjacent pixels on the same row, whereas those on the right for adjacent pixels on the same column

size is an important information for studying possible biases in the performace of the pixel detector.
This measurement is shown in table 2.3 as percentage of occurrence of a particular cluster size with respect to the total number of clusters.
It is hard to draw any quantitative conclusion from this table. Nevertheless, one can say that, because of the lower charge-collection efficiency induced by the radiation damage and, hence, an effective higher threshold value, the amount of sharing diminishes moving from ROC5 to ROC8. On ROC8 the sharing is practically identical to that of the non-irradiated ROC0, which, indeed, had a threshold (3800 e^-) higher than that of the other ROCs (3300 e^-).

Cluster size	ROC0 (%)	ROC5 (%)	ROC6 (%)	ROC8 (%)
1	85.42±0.70	81.78±0.43	82.03±0.28	85.57±0.27
2	12.75±0.66	16.00±0.40	15.17±0.26	12.73±0.26
3	0.75±0.17	1.15±0.12	1.29±0.08	0.84±0.07
4	0.83±0.18	0.72±0.09	1.05±0.07	0.55±0.06
5	0.08±0.06	0.12±0.04	0.21±0.03	0.14±0.03
6	0.08±0.06	0.10±0.04	0.21±0.03	0.06±0.02

Table 2.3.: The percentage of occurrence of a certain cluster size is normalized to the total number of clusters

2.4 CONCLUSIONS

A precise reconstruction of primary and secondary vertices that are the base of the physics analyses in CMS requires at least two hits in the pixel system. This detector is the innermost component of CMS and it is expected to integrate a maximum dose of about 7 Mrad per year on the inner edge of the first disk at the LHC design luminosity and energy.
To study the long term performance, a module of the forward pixel detector of the CMS experiment, irradiated up to 45 Mrad, was tested on a beam at Fermilab.
The most evident sign of the radiation-induced damages at the highest dose was the reduction of $\sim 25\%$ of the signal released by a minimum ionizing particle. The detection efficiency, though, remains very high, $\sim 99\%$, even at an equivalent threshold of about 3300 e^- and just shows some marginal drop near the pixel corners at the highest absorbed dose. There is an apparent relative increase of the charge-collection efficiency in the inter-pixel region at high radiation dose, which, in presence of the p-stop breaks, alters the symmetry of the η-distributions. In principle, this should be taken into account when interpolating the charge to extract the coordinate of the track impact point.
In conclusion, despite the observed damages, the detector remains fully operational: these good results ensure the necessary performance for a precise tracking required to accomplish the CMS physics goal.

CHAPTER 3

PHYSICS OF THE B_c MESON

The existence of the third generation quark doublet was proposed in 1973 by Kobayashi and Maskawa in their model of the quark mixing matrix (CKM matrix) [14], and confirmed four years later by the first observation of a $b\bar{b}$ meson [15]. Despite this old evidence, the chapter of flavour is not completely written, even if this field has become one of the most active areas within contemporary particle physics.
It is part of the programs also in the LHC experiments. The hadron collider at CERN will produce a large amounts of b hadrons of all varieties, B_u, B_d, B_s, B_c mesons and b-flavoured baryons. Their numerous decay channels probe the flavour sector of the Standard Model (SM) and of any scenario conceived to go beyond it.

3.1 INTRODUCTION

The bound states of a $\bar{b}$ antiquark and a u, d, s or c are refered to as the B_u (B^+), B_d (B^0), B_s^0, B_c^+ mesons respectively.
Experimental studies of b decays have been performed in e^+ e^- collisions at the $\Upsilon(4S)$ resonance (ARGUS, CLEO, Belle, and BaBar), as well as at higher energies at the Z resonance (SLC and LEP) and in p-$\bar{p}$ collisions (Tevatron). Recent developments in the physics of the b-hadrons include the observation of direct CP violation, results for rare higher-order-weak decays, measurement of the B_s^0-mixing frequency, increasingly accurate determinations of the CKM matrix element V_{cb} and V_{ub}, and of the angle α and γ of the unitarity triangle.
All species of b-flavoured hadrons will be produced with a very large cross-section in high-energy p-p collisions ($\sim 500\ \mu b$ over the full 4π solid angle, at the design energy of the LHC). The total b-production cross section in hadronic collisions is an interesting test of the understanding of QCD processes. For

many years, experimental measurements resulted to be higher than predictions. With improved measurements, more accurate input parameters, and more advanced calculations, the discrepancy between theory and data is now much reduced, although the presence of inconsistencies among existing measurements makes further data desirable.
The b-quarks are abundantly produced in hadron collisions but, because of the high background, only few decay modes for which the trigger and the reconstruction are easiest have been studied so far at Tevatron. These have included final states with leptons, and the exclusive modes into all charged particles.
The advantage of the hadron colliders is the possibility, thanks to the higher energy available in the interaction, to investigate the full spectrum of b-hadrons, including those states, such as B_s, B_c, b baryons or excited states, not available at the B-factories.
Some processes could be affected by significant effects induced by new physics (NP) processes if the NP scale is not completely decoupled from the TeV scale. On the one hand, no deviations from the Standard Model predictions have been observed for the, B_d (B_u): the properties of these mesons have already been studied in detailed by the B-factories experiments, yielding an impressive agreement with the Standard Model expectations. On the other hand, the properties of the B_s mesons have not been deeply investigated; only the Tevatron can produce it, and its decays could have significant contributions from new physics effects. Moreover, the study of the B system with high statistics samples of different b hadrons can be used to further constrain the SM CP violation mechanism described by the Cabibbo-Kobayashi-Maskawa (CKM) matrix and check the SM consistency itself.

3.2 B PHYSICS AT THE LHC

A variety of B physics topics are present in the physics program of three LHC experiments. LHCb is devoted to study the physics of flavour, while the two general purpose experiments, ATLAS and CMS, could perform this kind of research in some specific channels easiest to trigger and reconstruct. The feasibility of B physics measurements at these two experiment is supported by recent results from CDF and D0 at Tevatron.
The programs of the three LHC experiments cover several different areas: leptonic decay and CP violation, cross section determination, rare decay investigations and new physics search.
Some topics of interest for the CMS experiment are mentioned in the following paragraphs; the B_c physics, is presented in a separate section (3.3).

3.2.1 CROSS SECTION FOR $b\bar{b}$ PRODUCTION

The current prediction of $\sigma(b\bar{b}) \sim 500$ μb comes from the extrapolation of Tevatron results: a precise measurement of cross section is of major importance in order to test the Monte Carlo simulations, the NLO QCD calculations used for the extrapolations and the Parton Density Functions (PDF) knowledge. For the rare decays, NP and the new particle searches the knowledge of $\sigma(b\bar{b})$ is also important to achieve a good estimate of the background level.
Inclusive and exclusive strategies can be used to measure the cross section. CMS experiment plans to use J/ψ events to measure the production rate: the muons in the decay ensure an high efficiency in triggering and reconstructing those channels. A full p_T scan can be perfomed with a statistical precision of $\sim 10\%$ in all bin at 10 fb^{-1} of integrated luminosity [16].

3.2.2 NEW PHYSICS SEARCH

At the hadron collider the new physics search proceeds through the precise measurements of SM parameters, such as the weak phase $\phi_s = 2\lambda^2\eta$ from the decay $B_S \to J/\psi\phi$, or rare decays, such as $B_S \to \mu^+\mu^-$ is one example, that are highly suppressed by the Standard Model (SM) but can receive important contributions from the physics beyond the SM.

$B_S \to J/\psi\phi$

The decay $B_S \to J/\psi\phi \to \mu^+\mu^- K^+K^-$ allows to study many properties of the B_S^0 system, such as the differences between the widths, $\Delta\Gamma_S$, and the masses, Δm_s, of the two weak eigenstates, B_S^H and B_S^L. Contrary to the B^0 system, the difference between the widths $\Delta\Gamma_s = \Gamma_H - \Gamma_L$ is expected to be large, with a relative difference compared to the mean width $\Delta\Gamma_s = (\Gamma_H + \Gamma_L)/2$, namely $\Delta\Gamma_s/\bar{\Gamma_s}$, which is predicted to be in the order of 10% in the Standard Model (SM) [17]. The current measurements from CDF and from D0 still have large errors [18]. Furthermore, this decay provides one of the best ways to determine the height of the Unitarity Triangle, η in the Wolfenstein parameterization. To first order of the Wolfenstein parameterization, the CP-violating weak phase of $B_S^0 - \bar{B_S}^0$ mixing $\phi_s = 2[arg(V_{cs}^* V_{cb}) - arg(V_{ts}^* V_{tb})]$ is vanishing, and higher order terms have to be taken, yielding a weak phase $\phi_s = 2\lambda^2\eta$. The weak phase is therefore expected to be very small, of the order of ~ 0.03 [19], and the measurement of a significantly larger phase would indicate contributions from non Standard Model processes [20].
From the experimental point of view, this decay is particularly suited for the detection and reconstruction in all the LHC experiments, since it can be efficiencly triggered thanks to the two muons from the J/ψ decay. It also has a relative large Branching ratio, i.e. $BR(B_S \to J/\psi\phi) \cdot BR(J/\psi \to \mu^+\mu^-) \cdot BR(\phi \to$

$K^+K^-) \sim 3 \cdot 10^{-5}$ [21].
The CMS experiment could contribute to this measurement reaching the SM prediction at 1.1% precision at 10 fb^{-1} of statistics.

$B_S \to \mu^+\mu^-$

The $B_S \to \mu^+\mu^-$ decay is predicted in the SM to be very rare, since it involves flavour changing neutral currents and experiences a large helicity suppression ($\sim m_\mu/m_b$), with a BR at the level of $\sim 4 \cdot 10^{-9}$ [22]. Various attempts have already been made to measure the BR: the current best limits are coming from CDF (BR $< 4.3 \cdot 10^{-8}$ at 90% CL [23]) and D0 (BR $< 4.3 \cdot 10^{-8}$ at 90% CL [24]) measurements.
The study of this decay is of particular interest when probing NP models, like the MSSM, that allows for large modifications of the BR: the contribution of a $tan^6\beta/M_A^4$ term, for example, can significantly enhance the measured value if the $tan\beta$ value is large (as suggested by other experimental results like $b \to s\gamma$, $(g-2)_\mu$ and $B \to \tau\nu$).
The measurement of the $B_S \to \mu^+\mu^-$ BR can thus play a major role in constraining (measuring) the NP contributions and even help selecting (ruling out) a given theoretical model.
The CMS experiment can carry out an upper limit about four times larger than the SM expectation, i.e. $1.4 \cdot 10^{-8}$; however, it can provide some constrains on the new physics models already at 10 fb^{-1} integrated luminosity.

3.3 B_C PHYSICS

The B_C meson, the ground state of the $(\bar{bc})$ system, is doubly heavy flavoured; in many respects it is an intermediate between $(c\bar{c})$ and $(b\bar{b})$ systems. However, because it carries open flavour, the B_C is then unique in providing a new window to study heavy-quark dynamics: with the different heavy flavours will complement the phenomenological information obtained from charmonium and bottomonium.
From the theoretical point of view, the B_C meson and its excited states are studied with the non-relativistic QCD (NRQCD). These flavoured particles have two features in common with the $b\bar{b}$ and $c\bar{c}$ quarkonia: the non-relativistic motion of the b and c quarks and the suppression of the light quark-antiquark sea. These two physical conditions are useful in the study because imply two small expansion parameters: the relative velocity v of quarks and the ratio Λ_{QCD}/m_Q of the confinement scale to the heavy quark mass. The double expansion generalizes the HQET approach [25, 26] to the NRQCD [27, 28]. The direct production of the B_C and other $(\bar{bc})$ mesons is treated within the factorization framework. Further, the $1/m_Q$ parameter is the appropriate quantity for the operator

product expansion (OPE) and also justifies the use of potential models (PM) in the calculations of hadronic matrix elements. The same arguments ensure the applicability of sum rules (SR) of QCD and NRQCD. All these three approaches are used to study the decay of ($\bar{bc}$) mesons.
At the LHC, the rich fields of study, such as spectroscopy, production mechanism and decays, can be investigated thanks to the large statistics that will be collected by the experiments. The current theoretical knowledge on spectroscopy, production and decay will be briefly explained in the following sections.

3.3.1 SPECTROSCOPY

The description of the B_C mass spectrum can test the self-consistency of the potential models and the QCD sum rules, whose parameters (the quark masses, for instance) have been fixed from the fitting of the spectroscopic data on the charmonium and bottomonium. Thus, the study of B_C-family spectroscopy can serve to improve the quantitative characteristics of the quark models and the QCD sum rules, which are intensively applied in other fields of heavy quark physics.
The family of mesons that exist within the $\bar{bc}$ system provide a rich spectroscopy of radial and angular momentum excitations, The full spectroscopy calculated using the relativized quark model [29] is shown in figure 3.1. The excited B_C states lying below *BD* threshold (minimum energy for the decay into a BD meson pair: $\sim$ 7.15 GeV) can only undergo radiative or hadronic transitions to the B_C ground state, which decays only weakly.

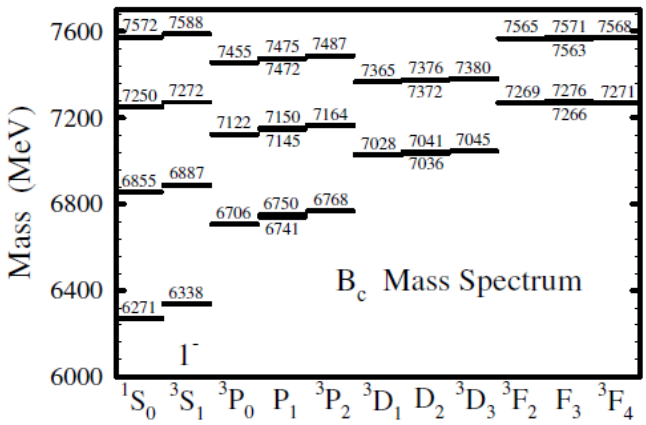

Figure 3.1.: B_C mass spectrum predicted using the relativized quark model in [29].

The most recent predition for the ground state mass has been pubblished by

the HPQCD Collaboration [30]. A three flavour (unquenched) lattice QCD numerical algorithm, that yielded the smallest theoretical uncertainty, carried out $M(B_C) = 6.304 \pm 0.012^{+0.018}_{-0}$ GeV$/c^2$ [31], where the first error is the sum in quadrature of statistical and systematic uncertainties, and the second is due to heavy quark discretization effects.

3.3.2 PRODUCTION

The production of a B_C can be thought as a three step process. First, a $\bar{b}$ and a c with small relative momentum are created by parton collision. Second, the $\bar{b}$ and the c bind to form the B_C or one of its excited states below the BD threshold. Third, the excited states all cascade down to the ground state B_C via hadronic or electromagnetic transition [32]. Thus, the total production cross section for the B_C is the sum of the direct production cross section for the B_C and its excited states.
Production of heavy quarkonia begins with a hard scattering, creating a heavy quark-antiquark pair in a specific angular momentum and color state, that can be a color singlet state, denoted by ($\bar{b}c$*(1)*), or a color-octet state, ($\bar{b}c$*(8)*). By standard spectroscopic notation, 2S+1LJ is the angular momentum state denotation.
The inclusive differential cross section for producing a B_C state in a proton-proton collision can be written as:

$$d\sigma[p_1 + p_2 \to H + X] = \sum_{ij} \int dx_1 dx_2 \, f_{i/p_1}(x_1) \, f_{j/p_2}(x_2) d\sigma[ij \to H + X] \quad (3.1)$$

where the functions $f_{k/A}$ are the parton distribution functions and the sum is over the partons i and j in the initial state hadrons, the cross section $d\sigma[ij \to H + X]$, which is the direct production of H in the collisions of partons i and j; this $d\sigma$ can be written as the sum of products of short-distance cross sections and long-distance matrix elements:

$$d\sigma[ij \to H + X] = \sum_n d\hat{\sigma}[ij \to \bar{b}c(n) + X] \langle O^H(n) \rangle \quad (3.2)$$

In the above equation, $d\hat{\sigma}[ij \to \bar{b}c(n) + X]$ is the short distance cross section for creating the $\bar{b}c$ in the color and angular momentum state n, and it can be calculated as a pertubative expansion in α_s at scales of m_c or larger.
The long-distance matrix element $\langle O^H(n) \rangle$ is non-perturbative and it encodes the probability for a $\bar{b}c$ in the state n to bind and form the meson H. This matrix element scales by the relative velocity v of the charm quark.
It's important to notice that the production mechanisms for the ($\bar{b}c$) differ in an essential way from those for ($\bar{b}b$), because two heavy quark-antiquark pairs must be created in the primary interaction. While a $\bar{b}b$ pair can be created at

order α_s^2 by the parton processes $q\bar{q},\ gg \rightarrow b\bar{b}$, the lowest order mechanisms for creating ($b\bar{c}$) are the order-α_s^4 processes $q\bar{q},\ gg \rightarrow b\bar{c}+b+\bar{c}$. At the LHC the gluonic contribution dominates.
The parton process $gg \rightarrow b\bar{c}+b+\bar{c}$ can create a ($b\bar{c}$) in either a color singlet or a color octect state. The cross section for the color octet state $b\bar{c}$ is expected to be about a factor 8 larger than that for the color singlet $b\bar{c}$, just from counting the color states. This factor can compensate any suppression factors of v from the probability for the color octect $b\bar{c}$ to bind to form a meson. Color octect contributions to the P-wave production have been recently calculated [33, 34] and have been implemented in the generator BCVEGPY [35] used for this thesis.
α_s depends on μ, where μ is the energy scale of the process. The $\alpha_s^4(\mu)$ factor introduces a large uncertainties in the theoretical predictions: there is a large ambiguity in the choice of the scale μ, since the short distance process involves several scales, including m_c, m_b, and p_T.

3.3.3 DECAY

Decays of the long-lived heavy meson B_C where considered in the pioneering paper written by Bjorken in 1986 [36]. Bjorken's report gave a unified view of the decays of hadrons with heavy quarks: mesons and baryons with a single heavy quark, the B_C meson, and baryons with two and three heavy quarks.
His estimates of total widths and various branching fractions are close to what is evaluated in a more strict manner with the modern theoretical tools.
The B_C ground state decade only weakly; various hadronic matrix elements enter in the description of decays. Conseguentely, measuring the lifetimes and branching ratios therefore provides information about non-perturbative QCD interactions.
Improvements in the non-relativistic QCD calculations impact on the determination of electroweak parameters, such as the quark masses and the mixing angles in the CKM matrix, which enter constraints on the physics beyond the Standard Model. The accumulation of more data on hadrons with heavy quarks will provide greater accuracy and confidence in the understanding of the QCD dynamics that is necessary to isolate the electroweak parameters.
As already said, the decay is studied with OPE, PM and SR. At present, all three approaches give similar results for the lifetime and inclusive decay modes of the B_C for similar sets of input parameters.

B_C LIFETIME AND INCLUSIVE DECAY RATES

The B_C meson decay processes can be subdivided into three classes:

- the $\bar{b}$-quark decay with the spectator c-quark,
- the c-quark decay with the spectator $\bar{b}$-quark and

· the annihilation channel $B_c \to l + \nu_l$ $(c\bar{s}, u\bar{s})$, where $l = e, \mu, \tau$.

In the first case, the specific process $\bar{b} \to \bar{c}c\bar{s}$ (where the $c\bar{s}$ is the product resulting from the W^+ decay) must be separated in the total width calculation due to the Pauli Interference (PI) with the charm quark from the initial state.
In accordance with the given classification, the total width is the sum over the partial widths

$$\Gamma(B_c \to X) = \Gamma(b \to X) + \Gamma(c \to X) + \Gamma(ann.) + \Gamma(PI). \tag{3.3}$$

Due to the three different possible decay channels, the B_c meson has an expected lifetime that is roughly on third shorter than other B mesons. The expected contribution for each decay path can be calculated using several different theoretical models.
For the annihilation channel, the $\Gamma(ann.)$ width can be reliably estimated in the framework of inclusive approach, summing up the widths from the $\bar{b}c$ annihilating into a W^+ and then into quarks and leptons. For the quarks decay modes, the hard gluon corrections to the effective four-quark interaction of weak currents have to be take into account and results in an enhancement factor a_1 ($a_1 = 1.22 \pm 0.04$). The factor a_1 is introduced in the factorization approach by Bauer, Stech and Wirber [37] to circumvent the problem of the scale dependence: in the effective four quark interaction lagrangian the Wilson coefficients are replaced by phenomenological constants a_1 and a_2.
This estimate of the quark-contribution does not depend on a hadronization model, since a large energy release of the order of the meson mass takes place. From the following expression, one can see that the contribution by light leptons and quarks can be neglected,

$$\Gamma(ann.) = \sum_{i=\tau,c} \frac{G_F^2}{8\pi} |V_{cb}|^2 f_{B_c}^2 M m_i^2 (1 - m_i^2/m_{B_c}^2)^2 \cdot C_i, \tag{3.4}$$

where $C_\tau = 1$ for the $\tau^+\nu_\tau$ channel and $C_c = 3|V_{cs}|^2 a_1^2$ for the $c\bar{s}$ channel, the estimated decay constant $f_{B_c} \approx 400$ MeV.
For the non annihilation channel, QCD corrections need to be applied and these decays are studied in the already mentioned OPE, PM and QCD SR models. Table 3.1 summarizes the prediction of different model: the dominant contribution to the B_c lifetime is expected to be the charmed quark decays ($\sim 65\%$), while the b-quark decays and the weak annihilation add about 25% and 10%, respectively.
The OPE approach takes into account the α_s correction to the free quarks decay and uses the quark hadron duality for the final states. In this approach, the matrix element for the transition operator over the bound meson state has to be considered: the effects caused by the motion and virtuality of decaying quark inside the meson because of the interaction with the spectator is accounted in this way. In this way the $\bar{b} \to \bar{c}c\bar{s}$ decay mode turns out to be suppressed almost

B_C decay mode	OPE %	PM %	SR %
$\bar{b} \to \bar{c} l^+ \nu$	3.9±1.0	3.7±0.9	2.9±0.3
$\bar{b} \to \bar{c} u \bar{d}$	16.2±4.1	16.7±4.7	13.1±1.3
$\sum \bar{b} \to \bar{c}$	25.0±6.2	25.0±6.2	19.6±1.9
$c \to s l^+ \nu$	8.5±2.1	10.1±2.5	9.0±0.9
$c \to s u \bar{d}$	47.3±11.8	45.4±11.1	54.0±5.4
$\sum c \to s$	64.3±16.1	65.6±16.4	72.0±7.2
$B_c^+ \to \tau^+ \nu_\tau$	2.9±0.7	2.0±0.5	1.8±0.2
$B_c^+ \to c \bar{s}$	7.2±1.8	7.2±1.8	6.6±0.7

Table 3.1.: The branching ratios (BR) of the B_c decay modes calculated in the framework of inclusive OPE approach, by summing up the exclisive mode in the potential model [38–40] and according to the semi-inclusive estimates in sum rules of QCD and NRQCD[41, 42]

completely due to the Pauli interference with the charm quark from the initial state. Besides, the c quark decay with the spectator $\bar{b}$ quark are essentially suppressed in comparison with the free quark decays because of a large bound energy in the initial state.
The main source of uncertainty in the OPE calculations is the strong dependence of the width prediction from the quark masses. The lifetime dependence on the b quark mass can be eliminated by the relation [43]:

$$m_b = m_c + 3.5 \text{ GeV}.$$

The above heavy quark mass relation comes from the fact that for any value of m_c, m_b is obtained by matching the results of the B_d meson lifetime calculation to that of the experimentally measured value of τ_{B_d}. However, large change in lifetime are predicted when the c quark mass value is varied (see table 3.2).

Parameters, GeV	$\sum \bar{b} \to \bar{c}$, ps^{-1}	$\sum c \to s$, ps^{-1}	PI, ps^{-1}	WA, ps^{-1}	τ_{B_c}, ps
$m_b = 5.0, m_c = 1.5, m_s = 0.20$	0.694	1.148	-0.115	0.193	0.54
$m_b = 4.8, m_c = 1.35, m_s = 0.15$	0.576	0.725	-0.132	0.168	0.75
$m_b = 5.1, m_c = 1.6, m_s = 0.45$	0.635	1.033	-0.101	0.210	0.55
$m_b = 5.1, m_c = 1.6, m_s = 0.20$	0.626	1.605	-0.101	0.210	0.43
$m_b = 5.05, m_c = 1.55, m_s = 0.20$	0.623	1.323	-0.107	0.201	0.48
$m_b = 5.0, m_c = 1.5, m_s = 0.15$	0.620	1.204	-0.114	0.193	0.53

Table 3.2.: B_c lifetime and width predictions for various c quark mass choices [43]. The partial widths are listed in ps^{-1} and the lifetimes in ps.

Another framework, used in calculations on non-annihilation channels, is the exclusive approach. Here, to obtain the total width, it is necessary to sum up widths of different decay modes calculated in the potential models (PM).

In the semileptonic decays, i.e. the $\bar{b} \to \bar{c}l + \nu_l$ and $c \to sl + \nu_l$ transitions, the hadronic final states are practically saturated by the lightest bound 1S-state in the $(\bar{c}c)$-system, i.e. by the η_c and J/ψ particles, and the 1S-states in the $(\bar{b}s)$-system, i.e. B_S and B_S^*. Further, the $\bar{b} \to \bar{c}u\bar{d}$ channel, for example, can be calculated through the given decay width of $\bar{b} \to \bar{c}l + \nu_l$ with account for the color factor and hard gluon corrections to the four-quark interaction.
Calculations for the total B_C width in the inclusive OPE and exclusive PM approaches give values consistent with each other if the most significant uncertainty related to the choice of the quark masses is considered; the results is:

$$\tau(B_C)_{OPE,PM} = 0.55 \pm 0.15 \text{ ps}, \tag{3.5}$$

The third theoretical approach is that of QCD SR [42, 44]. In contrast to OPE, where the basic uncertainty is given by the variation of heavy quark masses, in QCD SR calculation these parameters are fixed by the two-point sum rules for bottomonia and charmonia. The accurancy for the total width of B_C is determined by the choice of scale μ for the hadronic weak lagrangian in decays of charmed quark. This dependence is shown in figure 3.2, where $m_c/2 < \mu < m_c$ and the dark shaded region corresponds to the scales preferred by data on the charmed meson lifetimes.
Supposing the preferable choice of scale in the $c \to s$ decays of B_C to be equal to $\mu_{B_c}^2 \approx (0.85\text{GeV})^2$, putting $a_1(\mu_{B_c}) = 1.20$ and neglecting the contributions caused by nonzero a_2 in the charmed quark decays [42], in the framework of semi-inclusive sum-rule calculations the lifetime prediction is

$$\tau(B_C)_{SR} = 0.48 \pm 0.05\text{ps}, \tag{3.6}$$

EXCLUSIVE DECAY RATES

The exclusive decays can be divided into two classes: the leptonic and semileptonic modes and the non-leptonic modes. The predictions of QCD SR for the exclusive decays of B_C are summarized in table 3.3 at the fixed values of factors $a_{1,2}$ and lifetime.

The semileptonic decay rates are studied usign QCD SR and PM. The absolute values of semileptonic widths are presented in table 3.4. In practice, the most constructive information is given by the J/ψ mode, since this charmonium is clearly detected in experiments due to the pure leptonic decays [47]. In addition to the investigation of various form factors and their dependence on the transfer squared, the measurement of decay to the excited state of charmonium, i.e. ψ', could answer the question on the reliability of QCD predictions for the decays to the excited states. At the moment, the finite energy sum rules predict the width of $B_C^+ \to \psi' l^+ \nu$ decays in a reasonable agreement with the potential models.
The dominant leptonic decay of B_C is given by the $\tau\nu$ mode (see table 3.1).

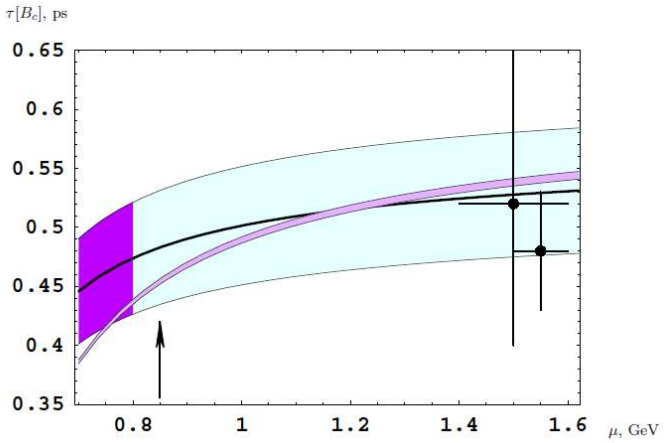

Figure 3.2.: The B_C lifetime calculated in QCD sum rules versus the scale of hadronic weak Lagrangian. The shaded region shows the uncertainty of estimates, the dark shaded region is the preferable choice as given by the lifetimes of charmed mesons. The points represent the values in OPE approach taken from [45]. The narrow shaded region represents the result obtained by summing up the exclusive channels with the variation of hadronic scale in the decays of beauty anti-quark in the range of $1 < \mu_b < 5$ GeV. The arrow points to the preferable prescription of $\mu = 0.85$ GeV as discussed in[42]

However, it has a low experimental efficiency of detection because of the hadronic background in the τ decays, the absence of the secondary vertex and a missing energy, due to the presence of the undetected neutrino. Recently, in [53] the enhancement of muon and electron channels in the radiative modes was studied. The additional photon allows one to remove the helicity suppression for the leptonic decay of pseudoscalar particle, which leads, say, to the double increase of muonic mode.

The non-leptonic two body B decays can be described using the Bauer Stech and Wirber model; in addition to the factorization, the BSW model uses hadronic currents instead of quark currents and allows the coefficient a_1 and a_2 of the product of the currents to be free parameter determined by experimental data [54]. The processes with different behavior in the color lines can be divided into three classes according to the coefficient a_1 and a_2 in the effective lagrangian: direct transitions with no permutation in the color line depends on a_1 only (class I processes), transitions with permutations in the color line depend on a_2 only and are classified as class II processes, the inteference of the two previous process depends on both a_1 an a_2 (class III process).

The B_C non leptonic modes are interesting to test the factorization approach and extract the coefficients. The QCD SR and PM predictions are in agreement for class I processes but, in contrast, the SR estimates are significantly enhanced in

Mode	BR %	Mode	BR %	Mode	BR %
$B_c^+ \to \eta_c e^+ \nu$	0.75	$B_c^+ \to J/\psi K^+$	0.011	$B_c^+ \to B_s^0 K^+$	1.06
$B_c^+ \to \eta_c \tau^+ \nu$	0.23	$B_c \to J/\psi K^{*+}$	0.022	$B_c^+ \to B_s^{*0} K^+$	0.37
$B_c^+ \to \eta_c' e^+ \nu$	0.041	$B_c^+ \to D^+ \overline{D}^0$	0.0053	$B_c^+ \to B_s^0 K^{*+}$	–
$B_c^+ \to \eta_c' \tau^+ \nu$	0.0034	$B_c^+ \to D^+ \overline{D}^{*0}$	0.0075	$B_c^+ \to B_s^{*0} K^{*+}$	–
$B_c^+ \to J/\psi e^+ \nu$	1.9	$B_c^+ \to D^{*+} \overline{D}^0$	0.0049	$B_c^+ \to B^0 \pi^+$	1.06
$B_c^+ \to J/\psi \tau^+ \nu$	0.48	$B_c^+ \to D^{*+} \overline{D}^{*0}$	0.033	$B_c^+ \to B^0 \rho^+$	0.96
$B_c^+ \to \psi' e^+ \nu$	0.132	$B_c^+ \to D_s^+ \overline{D}^0$	0.00048	$B_c^+ \to B^{*0} \pi^+$	0.95
$B_c^+ \to \psi' \tau^+ \nu$	0.011	$B_c^+ \to D_s^+ \overline{D}^{*0}$	0.00071	$B_c^+ \to B^{*0} \rho^+$	2.57
$B_c^+ \to D^0 e^+ \nu$	0.004	$B_c^+ \to D_s^{*+} \overline{D}^0$	0.00045	$B_c^+ \to B^0 K^+$	0.07
$B_c^+ \to D^0 \tau^+ \nu$	0.002	$B_c^+ \to D_s^{*+} \overline{D}^{*0}$	0.0026	$B_c^+ \to B^0 K^{*+}$	0.015
$B_c^+ \to D^{*0} e^+ \nu$	0.018	$B_c^+ \to \eta_c D_s^+$	0.86	$B_c^+ \to B^{*0} K^+$	0.055
$B_c^+ \to D^{*0} \tau^+ \nu$	0.008	$B_c^+ \to \eta_c D_s^{*+}$	0.26	$B_c^+ \to B^{*0} K^{*+}$	0.058
$B_c^+ \to B_s^0 e^+ \nu$	4.03	$B_c^+ \to J/\psi D_s^+$	0.17	$B_c^+ \to B^+ \overline{K^0}$	1.98
$B_c^+ \to B_s^{*0} e^+ \nu$	5.06	$B_c^+ \to J/\psi D_s^{*+}$	1.97	$B_c^+ \to B^+ \overline{K^{*0}}$	0.43
$B_c^+ \to B^0 e^+ \nu$	0.34	$B_c^+ \to \eta_c D^+$	0.032	$B_c^+ \to B^{*+} \overline{K^0}$	1.60
$B_c^+ \to B^{*0} e^+ \nu$	0.58	$B_c^+ \to \eta_c D^{*+}$	0.010	$B_c^+ \to B^{*+} \overline{K^{*0}}$	1.67
$B_c^+ \to \eta_c \pi^+$	0.20	$B_c^+ \to J/\psi D^+$	0.009	$B_c^+ \to B^+ \pi^0$	0.037
$B_c^+ \to \eta_c \rho^+$	0.42	$B_c^+ \to J/\psi D^{*+}$	0.074	$B_c^+ \to B^+ \rho^0$	0.034
$B_c^+ \to J/\psi \pi^+$	0.13	$B_c^+ \to B_s^0 \pi^+$	16.4	$B_c^+ \to B^{*+} \pi^0$	0.033
$B_c^+ \to J/\psi \rho^+$	0.40	$B_c^+ \to B_s^0 \rho^+$	7.2	$B_c^+ \to B^{*+} \rho^0$	0.09
$B_c^+ \to \eta_c K^+$	0.013	$B_c^+ \to B_s^{*0} \pi^+$	6.5	$B_c^+ \to \tau^+ \nu_\tau$	1.6
$B_c^+ \to \eta_c K^{*+}$	0.020	$B_c^+ \to B_s^{*0} \rho^+$	20.2	$B_c^+ \to c\overline{s}$	4.9

Table 3.3.: Branching ratios [46] of exclusive B_c^+ decays at the fixed choice of factors: $a_1^c = 1.20$ and $a_2^c = -0.317$ in the non-leptonic decays of c quark, and $a_1^b = 1.14$ and $a_2^b = -0.20$ in the non-leptonic decays of b quark. The lifetime of B_C is appropriately normalized by $\tau(B_c) \approx 0.45$ ps.

comparison with the value calculated in the PM for the class II transitions. The two approaches, instead, agree for the class III predictions. Taking into account the negative value of a_2 with respect to a_1, the characteristic values of effects caused by the interference is about 35-50%. The branching ratio, predicted by SR, for the $\bar{b}$ decay to the doubly charmed states is

$$\mathrm{Br}[B_c^+ \to \bar{c}c\,c\bar{s}] \approx 3.26\%,$$

so that, in the absolute value of width, it can be compared with the estimate of spectator decay [45],

$$\begin{aligned} \Gamma[B_c^+ \to \bar{c}c\,c\bar{s}]\big|_{\mathrm{SR}} &\approx 48 \cdot 10^{-15}\,\mathrm{GeV}, \\ \Gamma[B_c^+ \to \bar{c}c\,c\bar{s}]\big|_{\mathrm{spect.}} &\approx 90 \cdot 10^{-15}\,\mathrm{GeV}, \end{aligned}$$

Mode	Γ [46]	Γ [48]	Γ [49]	Γ [50]	Γ [51]	Γ [52]
$B_c^+ \to \eta_c e^+ \nu$	11	11.1	14.2	14	10.4	8.6
$B_c^+ \to \eta_c \tau^+ \nu$	3.3			3.8		2.9
$B_c^+ \to \eta_c' e^+ \nu$	0.60		0.73		0.74	
$B_c^+ \to \eta_c' \tau^+ \nu$	0.050					
$B_c^+ \to J/\psi e^+ \nu$	28	30.2	34.4	33	16.5	18
$B_c^+ \to J/\psi \tau^+ \nu$	7.0			8.4		5.0
$B_c^+ \to \psi' e^+ \nu$	1.94		1.45		3.1	
$B_c^+ \to \psi' \tau^+ \nu$	0.17					
$B_c^+ \to D^0 e^+ \nu$	0.059	0.049	0.094	0.26	0.026	
$B_c^+ \to D^0 \tau^+ \nu$	0.032			0.14		
$B_c^+ \to D^{*0} e^+ \nu$	0.27	0.192	0.269	0.49	0.053	
$B_c^+ \to D^{*0} \tau^+ \nu$	0.12			0.27		
$B_c^+ \to B_s^0 e^+ \nu$	59	14.3	26.6	29	13.8	15
$B_c^+ \to B_s^{*0} e^+ \nu$	65	50.4	44.0	37	16.9	34
$B_c^+ \to B^0 e^+ \nu$	4.9	1.14	2.30	2.1		
$B_c^+ \to B^{*0} e^+ \nu$	8.5	3.53	3.32	2.3		

Table 3.4.: Exclusive widths of semileptonic B_c^+ decays, Γ in 10^{-15} GeV. Prediction in the first column are from QCD SR, the others are from PM.

and have a suppression factor of about $1/2$. This result is in agreement with the estimate in OPE [45], where a strong dependence of negative term caused by the Pauli interference on the normalization scale of non-leptonic weak lagrangian was emphasized, so that at large scales one gets approximately the same suppression factor of $1/2$, too.
The factorization parameters a_1 and a_2 can be extract by measuring the branching ratios in the c-quark decays:

$$\begin{aligned} &\frac{\Gamma[B_c^+ \to B^+ \bar{K}^0]}{\Gamma[B_c^+ \to B^0 K^+]} = \frac{\Gamma[B_c^+ \to B^+ \bar{K}^{*0}]}{\Gamma[B_c^+ \to B^0 K^{*+}]} = \\ &\frac{\Gamma[B_c^+ \to B^{*+} \bar{K}^0]}{\Gamma[B_c^+ \to B^{*0} K^+]} = \frac{\Gamma[B_c^+ \to B^{*+} \bar{K}^{*0}]}{\Gamma[B_c^+ \to B^{*0} K^{*+}]} = \frac{\Gamma_0}{\Gamma_+} = \left|\frac{V_{cs}}{V_{cd}^2}\right|^2 \left(\frac{a_2}{a_1}\right)^2 . \end{aligned} \tag{3.7}$$

This procedure can give the test for the factorization approach itself and shed light to the characteristics of the non-leptonic decays.
In conclusions, measuring lifetime and branching ratio provides information about non-perturbative QCD interactions, on both the mass of charm and beauty quarks and on the normalization point of weak lagrangian in the B_C decay. Precise measurements could, thus, enforce the theoretical understanding of what really happens in the heavy quark decays at all.

CHAPTER 4

$B_c \to J/\psi\pi$ ANALYSIS

Since the first phase of the experiment, the B-physics study is one of the main topic of the CMS physics program, in term of detector commissioning and physics investigations.
The interest is in the direction of exploiting the potential of this sector in the new physics search through rare decays, such as $B_S \to \mu^+\mu^-$ and $B_S \to \phi\mu^+\mu^-$, and of enriching the heavy quark spectroscopy with the non yet well known system, such as B_c meson and b baryons.
The B_c will be abundantly produced at the LHC at $\sqrt{s} = 10$ TeV; the expected cross section is one order of magnitude larger than that at Tevatron.
In this chapter, after a review of the current B_c measurements, the analysis of the channel $B_c \to J/\psi\pi$ in CMS is presented and mass and lifetime results are reported.

4.1 CURRENT EXPERIMENTAL MEASUREMENTS

In spite of several theoretical predictions, described in chapter 3, the results from experimental investigation of the B_c meson are still limited to two channels:

$$B_c \to J/\psi l\nu \qquad \text{and} \qquad B_c \to J/\psi\pi$$

with the J/ψ decay in two muons.
The first observation of the B_c meson was made in 1998 by the CDF (Run I) experiment, in the $B_c \to J/\psi l\nu$ channel [47]. The statistics was 110 pb^{-1} of integrated luminosity of $p\bar{p}$ collisions at $\sqrt{s}$=1.8 TeV. The analysis was based on $20.4^{+6.2}_{-5.5}$ signal events and led to a B_c mass measurement of $M(B_c) = 6.40 \pm 0.39(stat) \pm 0.13(sys)$ GeV/c^2.
The B_c lifetime was measured to be $\tau = 0.46^{+0.18}_{-0.16}(stat) \pm 0.03(syst)$ ps from

the distribution of trilepton intersection point in the plane transverse to the beam direction.
A more precise measurement of the B_c mass was recently performed by the CDF experiment with 2.4 fb^{-1} of data in the fully reconstructed decay mode $B_c \to J/\psi\pi$, with the J/ψ decaying into two muons [55]. The data sample, collected by the CDF J/ψ trigger, contained $\sim$17 millions J/ψ candidates reconstructed with an average mass resolution of 0.013 GeV/c^2. The total B_c candidate events were estimated to be 108 ± 15 and the mass was measured to be $6.276 \pm 0.003(stat) \pm 0.003(sys)$ GeV/c^2.
A mass measurement, in the $B_c \to J/\psi\pi$ channel, was also made by the D0 experiment [56]: 1.3 fb^{-1} integrated luminosity of data yields 54 ± 12 B_c events and a mass=$6.300 \pm 0.014(stat) \pm 0.005(sys)$ GeV/c^2.
CDF and D0 have also recently updated the B_c lifetime measurement; CDF signal selections act on a sample of 1 fb^{-1} of di-muon candidates compatible with the J/ψ. The invariant mass of the two muons and the additional track, electron or muon, is required to be in the region 4–6 GeV/c^2. Because of the undetected neutrino, only the visible mass is, in fact, reconstructed and predicted in 4–6 GeV/c^2.
Events satisfying the above requirement are subjected to the lifetime measurement which results to be $\tau(B_c^{\pm}) = 0.475^{+0.053}_{-0.049}(stat.) \pm 0.018(syst.)$ ps ($c\tau = 142.5^{+15.8}_{-14.8}(stat.) \pm 5.5(syst.)\mu$m [57]).
The CDF result is compatible with that from D0, obtained with 1.3 fb^{-1} of data [58]. D0 analysis yields a signal of $881 \pm 80(stat.)$ candidates and a lifetime measurement of $\tau(B_c^{\pm}) = 0.448^{+0.038}_{-0.036}(stat.) \pm 0.032(syst.)$ ps.

4.2 THE B_C ANALYSIS IN THE CMS EXPERIMENT

CMS is a general purpose experiment and the detector is designed to reconstruct objects at high transverse momentum. The spectrometer acceptance excludes the possibility to investigate the high η region where the b production is larger. However, the efficient muon identification and the excellent resolution in track and vertex reconstruction allow analyses of the b particles decaying into muons: the channel $B_c \to J/\psi\pi$, with the subsequent decay $J/\psi \to \mu^+\mu^-$ which provides a clean mass signature, can be analysed even in absence of a dedicated particle ID detector using the information by the muon chambers and the tracker.

4.3 B_C PRODUCTION: BCVEGPY

The production cross section of the B_c is $\sim 10^3$ less than that of the $b\bar{b}$. In PYTHIA the production rate of B_c is $\sim 10^{-6}$ in a mininum bias production. Thus, it is necessary to enhance the event generation efficiency with a dedi-

cated generator. A well documented, based on PYTHIA, generator is available on the authors' web site: BCVEGPY [59, 60].
The first step of this work has been the integration of the generator in the CMS simulation package (CMSSW); a more detailed description can be found in chapter 5.
BCVEGPY emulates a matrix element generator and the generation can be stopped at "parton" level. An output file, containing the B_c, b and $\bar{c}$ information, is written out in the Les Houches Accord format[1] (file LHE), which can be easily interfaced with different hadronizing models.
The analysed Monte Carlo samples have been generated in a private production on the Milano-Bicocca computer cluster using PYTHIA as hadronizer in the official software CMSSW[2]. The predicted B_c production cross section is $\sim 0.8\ \mu$b at the LHC energy [61], thus, in 1 fb^{-1} integrated luminosity, the number of expected B_c events decaying in $J/\psi\pi$ is:

$$\begin{aligned} N &= \sigma \times L \times BR(B_c \to J/\psi\pi) \times BR(J/\psi \to \mu^+\mu^-) \\ &= 0.8\mu b \times 1 fb^{-1} \times 1.3 \cdot 10^{-3} \times 5.93 \cdot 10^{-2} \\ &\simeq 6 \cdot 10^4 \end{aligned} \tag{4.1}$$

$\sim 13\%$ of the total, i.e. 7777 of them, will be in the CMS acceptance. These numbers can be easily scaled to the expected luminosity for the first year of LHC running; in 200 pb^{-1} integrated luminosity (2009 Chamonix schedule [62]) $\sim 1.2 \cdot 10^4$ B_c mesons will be produced and decay in the exclusive channel of interest and 1558 will be in the CMS spectrometer.

4.4 BACKGROUND PRODUCTION

As the final state under investigation contains one J/ψ, the backgrounds that can yield this meson have been considered. At the hadrons colliders, the J/ψ production could occur mainly through the decay of the B-mesons and baryons or through direct production (prompt-J/ψ). Background samples have been generated in the Summer08 official production [63]; namely they are:

- /BtoJpsiMuMu/Summer08_IDEAL_V9_v2/GEN-SIM-RECO for the inclusive-b decaying into J/ψ, available integrated luminosity: 100 pb^{-1}.

- /JPsi/Summer08_IDEAL_V9_v1/GEN-SIM-RECO for the prompt-J/ψ sample, available integrated luminosity: 14.7 pb^{-1}

[1] Standard file format proposed to store process and event information, primarily output from parton-level event generators for further use by general-purpose Monte Carlo
[2] PYTHIA6.416 in the CMSSW_2_1_9 version

4.4.1 INCLUSIVE-b PRODUCTION

The inclusive-b sample collects different b hadrons (B, B^0, B_s, Λ_b, etc.), all decaying into J/ψ, with the subsequent decay J/$\psi \to \mu^+\mu^-$. This sample has been generated with EvtGenLHC, a modified version for hadron collider of EvtGen[64]. The original code was developed at the B-factories and it implements many detailed models that are important for the physics of b hadron. The novel idea in EvtGen is that decay amplitudes, instead of probabilities, are used for the simulation of decays.
In the simulation process, the p-p event is generated by PYTHIA up to the quark hadronization and EvtGenLHC is invoked only for b particles. Their decay is ruled by a decay table, included in the EvtGen package, DECAY.DEC, which provides an extensive list of decays and is updated with the available experimental and theoretical information. This table contains the branching ratio, the list of final state particles and specifies the process used to simulate [65]. In addition to the DECAY.DEC table, the output of EvtGen may be controlled via a user decay file, which is parsed after the standard table, in order to redefine the particle decays of interest for one of the two b particles produced in the interaction. Thus, for this specific sample, a b particle is forced to decay in charmonium channel according to the inclusive b decay file and the other follows the default DECAY.DEC. The available luminosity of 100 pb^{-1} corresponds to 2.4 millions of b hadrons in charmonium channels. The user file for this production has been developed by the LHCb experiment. This file collects the B hadron decays in charmonium channels (J/ψ, $\psi(2S)$, $\psi(3770)$, χ_{c0}, χ_{c1}, χ_{c2} and h_c) with the branching ratio properly rescaled.

4.4.2 PROMPT-J/ψ PRODUCTION

QCD production mechanisms of charmonium states are described by the color singlet and the color octect models. In the color singlet model (CSM), charmonium production begins with the production of a $c\bar{c}$ quark-antiquark pair in the colorless state. The process of forming the bound states preserves the quantum numbers of the initial pair. In this model, the J/ψ production is dominated by feed-down from χ_c production. Other sources of prompt J/ψ and $\psi(2S)$ mesons are expected to be negligible. However, this was not enough to explain the J/ψ behaviour observed at Tevatron [66, 67]: the rate is higher than expectation and p_T spectrum different from prediction. A possible extention to explain the discrepancy of the theoretical prediciton is the “color octect” production mechanism in the framework of non relativistic QCD (NRQCD). In this formalism, the production proceeds via intermediate $c\bar{c}$ states with different quantum number than those of the physical charmonium; the color octect states collapse to the singlet states by the emission of soft (nonperturbative) gluons. This model has been recently integrated in PYTHIA; the validation procedure is explained in [68]. Table 4.1 gives a summary of all the available subpro-

cesses for color-singlet and color-octet production contained within PYTHIA. The values of the NRQCD matrix elements used in the Summer08 production have been extracted from the validation paper and previously tuned on Tevatron data. The produced J/ψ sample has no polarization and the branching ratios for the radiative decay of the χ-states into J/ψ are updated to the most recent PDG values.

Charmonium color-singlet/octet production in PYTHIA	
421	$g+g \to c\bar{c}[^3S_1^{(1)}]+g$
422	$g+g \to c\bar{c}[^3S_1^{(8)}]+g$
423	$g+g \to c\bar{c}[^1S_0^{(8)}]+g$
424	$g+g \to c\bar{c}[^3P_J^{(8)}]+g$
425	$g+q \to q+c\bar{c}[^3S_1^{(8)}]$
426	$g+q \to q+c\bar{c}[^3S_0^{(8)}]$
427	$g+q \to q+c\bar{c}[^3P_J^{(8)}]$
428	$g+\bar{q} \to g+c\bar{c}[^3S_1^{(8)}]$
429	$g+\bar{q} \to g+c\bar{c}[^1S_0^{(8)}]$
430	$g+\bar{q} \to g+c\bar{c}[^3P_J^{(8)}]$
431	$g+g \to c\bar{c}[^3P_0^{(1)}]+g$
432	$g+g \to c\bar{c}[^3P_1^{(1)}]+g$
433	$g+g \to c\bar{c}[^3P_2^{(1)}]+g$
434	$g+q \to q+c\bar{c}[^3P_0^{(1)}]$
435	$g+q \to q+c\bar{c}[^3P_1^{(1)}]$
436	$g+q \to q+c\bar{c}[^3P_2^{(1)}]$
437	$g+\bar{q} \to c\bar{c}[^3P_0^{(1)}]+g$
438	$g+\bar{q} \to c\bar{c}[^3P_1^{(1)}]+g$
439	$g+\bar{q} \to c\bar{c}[^3P_2^{(1)}]+g$

Table 4.1.: Color-singlet/octect charmonium production sub-processes along with the corresponding ISUB indices in PYTHIA

As an aside, the promt-J/ψ measurements are part of the analysis program with the first data. With a sufficient statistics, these analyses will confirm or clash with the theoretical prediction of the color octet model and, in case, will allow to tune the theoretical calculation of the NRQCD matrix elements.

4.5 ADDITIONAL BACKGROUND

Beside the dominant background, the QCD contamination needs to be investigated. The muon generator-level filter used in the prompt-J/ψ and inclusive-b samples does not filter on muons from the decay in flight of pions and kaons, since the necessary code was not present in the simulation configuration files. Therefore, QCD background is studied using a $pp \rightarrow \mu X$ sample that is available in the Summer08 official production /InclusivePPmuX/Summer-08_IDEAL_V9_v4/GEN-SIM-RECO with an effective integrated luminosity of 0.044 pb^{-1}. This sample collects minimum bias events having at least one muon with $p_T > 2.5$ Gev and $|\eta| < 2.5$.

4.6 HIGH LEVEL TRIGGER

In CMS each event has to get through the two steps (L1 and HLT) of the trigger procedure to be accepted and recorded for the analysis (see section 1.3). Thus, the first step of this analysis is a positive response of the muonic high level trigger (HLT).
In the first phase of the experiment, the low luminosity allows loose requirements in trigger selections and a single muon trigger with a threshold $p_T > 3$ GeV/c is foreseen [69–71]. In the higher luminosity phase, this will be removed and replaced with an higher threshold single muon trigger. A trigger requiring two muons (threshold $p_T > 3$ GeV/c) will be more convenient at this point.
This double muon trigger is already present in the low luminosity phase table but, at the moment, is under study and not yet optimized: in the software version used for these sample production and analysis, the trigger fails when two muons are close to each other (small ΔR)[3]. This failure is due to the tracking procedure in the HLT algorithm: the match of the standalone muon tracks to the silicon tracks is done through a inside to outside algorithm. It uses the pixel seeds, which are no longer available for the second tracks if they are already used for the first one. This tracking procedure has been changed in the new software release: an outside to inside approach has been preferred and the pixel seeds are not needed anymore. Preliminary results from validation show, in fact, a higher efficiency.
With the software release used for the sample and the analysis of this thesis, the use of the double muon trigger would just imply an unrealistic reduction of the signal events and, thus, the single muon HLT has been preferred for the analysis. However, for completeness, a study was performed to verify the consistency of the results with the two muon trigger configuration. A summary can be found in the end of the chapter (section 4.9).

[3] $\Delta R = \sqrt{\Delta\eta^2 + \Delta\phi^2}$

4.7 $B_C \to J/\psi\pi$ ANALYSIS WITH 1 fb^{-1} OF DATA

The $B_C \to J/\psi\pi$ Tevatron analyses are based on some fb^{-1} of data. At the same level of integrated luminosity, CMS is expected to collect a higher number of B_C mesons decaying in the same channel; a new measurement of lifetime could be carried out in this fully reconstructed decay mode.
A luminosity of 1 fb^{-1} is thus chosen as benchmark value to performe the $B_C \to J/\psi\pi$ feasibility study in CMS.

4.7.1 SAMPLE RECONSTRUCTION AND B_C MASS DETERMINATION

The signal selection starts from the J/ψ reconstruction. The requests for the two muons are:

- $|\eta|$<2.5 [4]
- Global Muons[5];
- p_T> 3 GeV/c;
- common secondary vertex;
- invariant mass compatible with the J/ψ.

The vertex is reconstructed using the two muon tracks in a Kalman Filter technique (KalmanVertexFitter routine in CMSSW [72]) and the vertex confidence level (CL) is required to be higher than 0.05 to remove fake J/ψ candidates.
This procedure leads to 2705 J/ψ, reconstructed in 1 fb^{-1} of integrated luminosity of the B_C sample. Only 15 of them come from the B or χ_{1c} hadrons created by the b and $\bar{c}$ quarks accompanying the B_C production.
The event reconstruction proceeds through the pion search. The CMS experiment has no detector for particle ID. As a consequence, each track, that is not a muon, i.e. it has not associated hits in the muon system, is considered a pion candidate.
A cut on the p_T has been applied to reject the background while preserving the signal events. The p_T threshold is chosen at 10 GeV/c to reject most of the prompt-J/ψ(see figure 4.1).
Thus, the criteria to select the pion candidate are:

- $|\eta|$<2.5
- p_T> 10 GeV/c;

[4] Pseudorapidity $\eta = -ln\, tan\left(\frac{\theta}{2}\right)$ where θ is the angle relative to the beam axis

[5] See Appendix A.1 for definitions of this and following item

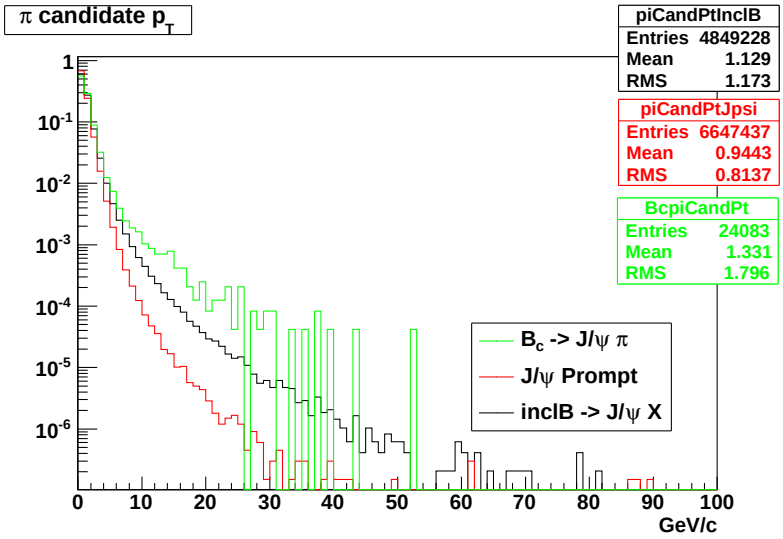

Figure 4.1.: p_T spectrum of the pion candidate for signal and backgrounds. The samples are normalised.

· common vertex with the two muons.

The three track vertex is reconstructed using the Kinematic Constrained Vertex Fitter, an algorithm based on the Kalman filter that improves the resolution of experimental measurements by introducing constraints derived from physics law [73, 74]: here the invariant mass of the two muons is constrained to the nominal mass of the J/ψ. The vertex C.L. is required to be higher than 0.05.
529 B_C events are reconstructed and the mass spectrum is shown in figure 4.2; 481 are expected in the B_C mass region. All the reconstructed candidates in this region are true B_C decaying into J/$\psi\pi$, 48 events at higher mass are caused by combinatorial of a J/ψ with a particle in the event not originating from the B_C.
At the integrated luminosity of the samples, 10 background events meet the selection, 5 from the inclusive-b and 5 from prompt-J/ψ. These numbers need to be rescaled to 1 fb^{-1}; $\sim$ 50 events from inclusive-b and $\sim$ 340 from prompt-J/ψ are thus expected to survive.
No events from QCD background survive the signal selection; however, the effective integrated luminosity of the QCD sample is 0.044 pb^{-1}, insufficient to reach a strong conclusions on its potential feed-through. A cross-check can be performed on the same sample loosing the cut selection; only events from B^0 decays meet the requirements. These events are already accounted for in the specific inclusive-b sample. At this level of statistics the QCD background can be considered thus negligible.
The remaining background events from inclusive-b and prompt-J/ψ have to be added to the invariant mass distribution of B_C candidates to perfom a complete analysis. The background distributions are shown in figure 4.3. The spectrum

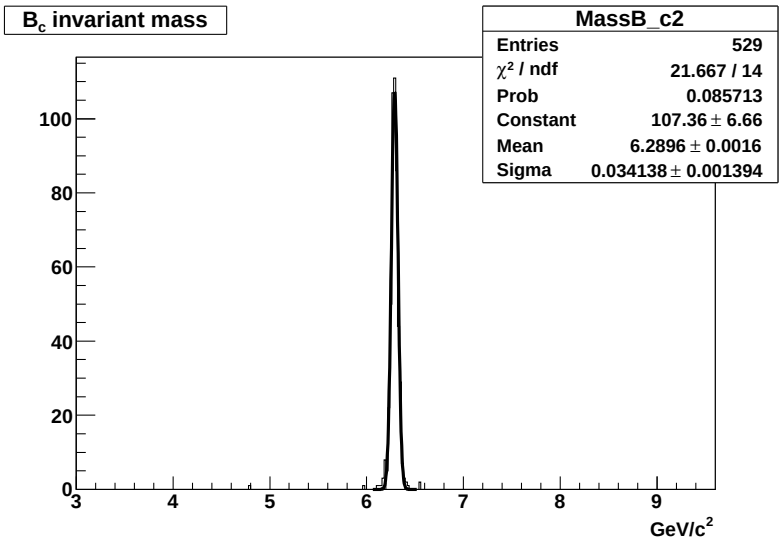

Figure 4.2.: B_C signal invariant mass distribution

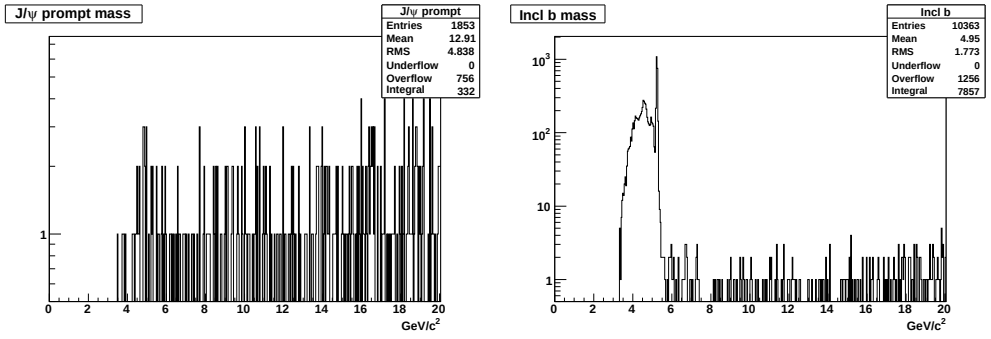

(a) (b)

Figure 4.3.: Background contaminations for (a) inclusive b and (b) prompt-J/ψ samples.

corresponding to 1 fb^{-1} is generated according to a flat distribution in the 6.1–6.5 GeV/c^2 region.

The resulting signal and background invariant mass distribution at the integrated luminosity of 1fb^{-1} is in figure 4.4. A fitting fuction, obtained combining a gaussian plus a polynomial, is used in the 6.15–6.45 GeV/c^2 region. This fit yields 451 ± 27 events, a mass $M(B_C) = 6.287 \pm 0.002 GeV/c^2$, well compatible with the input value of 6.286 GeV/c^2 from PDG [75], a width $\Gamma(B_C) = 0.032 \pm 0.002$ GeV/c^2 and a $S/N = 2.07 \pm 0.24$, where S is the number of B_C and N of background events calculated from the fit in the 3σ region. This results are summarised in table 4.2.

This result is competitive with the current Tevatron statistics: the measured yield is, in fact, $\sim$4 times larger than that pubblished from the CDF experiment

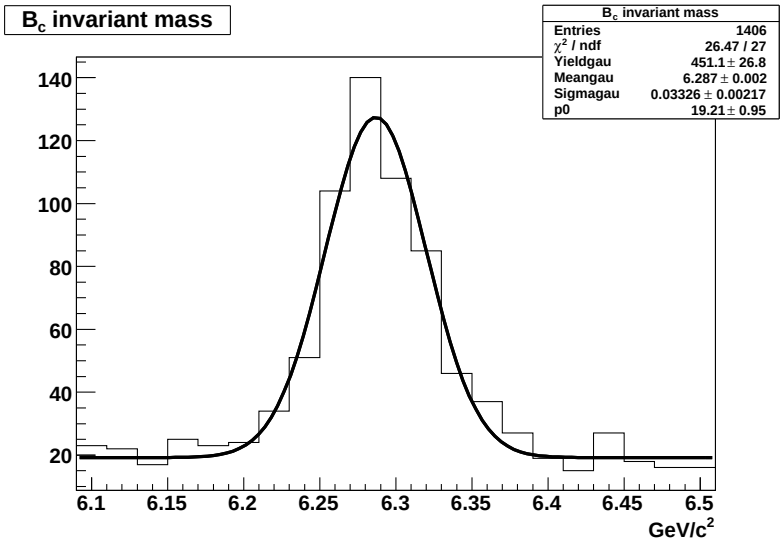

Figure 4.4.: Signal and background reconstructed invariant mass.

Yield	451±27
S/N	2.1±0.2
M(B_C)	6.287±0.002
$\Gamma(B_C)$	0.033±0.002

Table 4.2.: Mass fit results at 1fb^{-1}

and ∼8 times that from D0.
After the mass determination, the analysis proceed toward the lifetime measurement; additional cuts can be implemented to further reduce the background contamination.
The first selection is based on the event directionality: the vector pointing from the primary to the secondary vertex is aligned with the momentum for the well reconstructed events. Only events with $cos\theta > 0.8$ are considered, θ being the opening angle between the detachment vector and the B_C reconstructed momentum vector (both of them considered in the transverse plane), as schematized in figure 4.5.
The cosine distribution for signal and backgrounds is shown in figure 4.6; the applied cut is the dashed line in green. This cut removes the ∼73% of background from prompt-J/ψ, ∼20% from inclusive-b and rejects only ∼7% of the B_C sample.
The signal events which are poorly reconstructed and have the detachment vector opposite to the momentum are removed by the "signed" cosine. In these events, in fact, the resolution of the reconstructed track and vertex makes the secondary vertex to lay upstream of the primary. Simply cutting on the absolute value of the cosine would essentially preserve the signal but introduce a great amount of background (+6.5% form inclusive b and +95.4% from prompt-J/ψ).

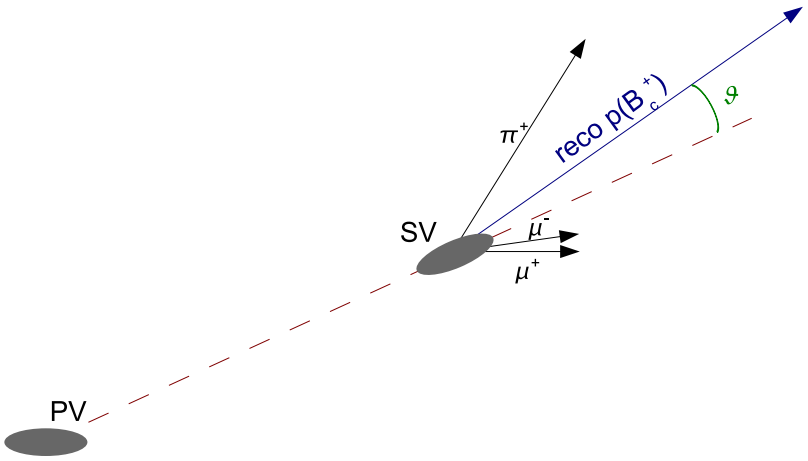

Figure 4.5.: A sketch of the typical $B_C \to J/\psi\pi$ event. θ is the the opening angle between the detachment vector and the B_C reconstructed momentum vector.

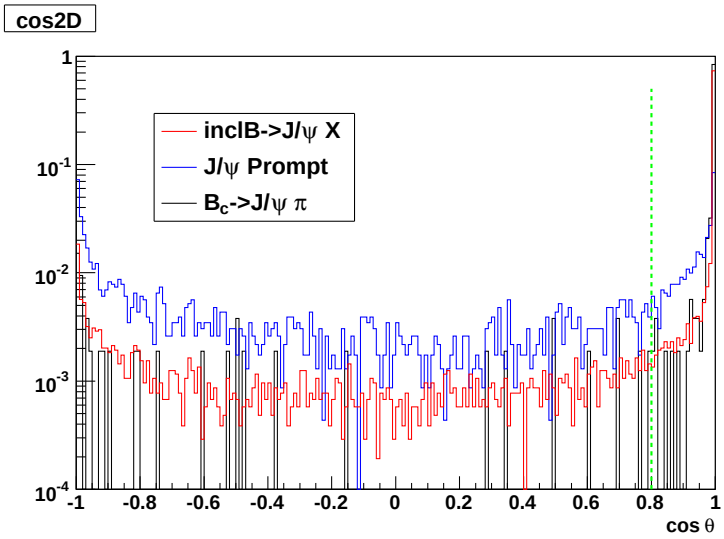

Figure 4.6.: Cosine distributions for signal and background samples. The dashed green line represent the applied cut.

After this selection, $\sim$ 654 events survive: 468 true B_C, $\sim$ 50 events from inclusive-b and $\sim$ 136 from prompt-J/ψ.
The next cut acts on the L/σ information. L is the proper decay length and σ is its resolution, computed from the full covariance matrix. 353 B_C and $\sim$ 40 inclusive-b events only survive the requirement $L/\sigma > 3$. According to our Monte Carlo the contamination from prompt-J/ψ has been completely removed at this point.
The global selection efficiency is 0.59%. The efficiency of the selection re-

quest for the B_c sample and the background rejections at each simple cuts are reported in table 4.3 and 4.4 respectively.

	Events	Efficiency %
Generated Event	60000	
Generation Filter	7777	12.96
HLT	5672	72.93
Reconstruced J/ψ	2705	47.69
Reconstructed B_c	481	17.78
$cos\theta > 0.8$	468	97.30
$L/\sigma > 3$	353	75.43

Table 4.3.: Single cut efficiencies for B_c sample. The total efficency is 0.59%

	inclusive-b	prompt-J/ψ	QCD
Generated (filtered)	2.4×10^6	1.9×10^6	5×10^6
HLT	1.5×10^6	919058	855306
J/ψ	544483	320372	511
B_c	5	5	0
$cos\theta > 0.8$	5	2	0
$L/\sigma > 3$	4	0	0

Table 4.4.: Background events at different cuts

The S/N ratio of this higher purity sample is $S/N = 17.9 \pm 6.8$. The mass is $M(B_c) = 6.289 \pm 0.002\,GeV/c^2$ and the width $\Gamma(B_c) = 0.034 \pm 0.002 GeV/c^2$. The statistical precision of 0.03% on the mass value is competitive with the 0.05% from the CDF experiment.
The CMS detector is designed to measure transverse quantities with high efficiency and excellent resolution since the first phase of data taking. The results presented so far refer to a transverse plane analysis. However, while investigating the vertex reconstruction the resolution in the z-direction was found to be quite good ($\sim 90\ \mu$m) suggesting the feasibility of the analysis in the 3D space. Both the cosine and the L/σ cut can be implemented using three dimensional quantities. An improvement in the precision of the measurement and in the background rejection efficiency is expected introducing the additional information of the third coordinate even though the limited statistics of the background sample does not allow to appreciate a major difference with respect of the 2D analysis. The mass results for the full space analysis are summarized in table 4.5.

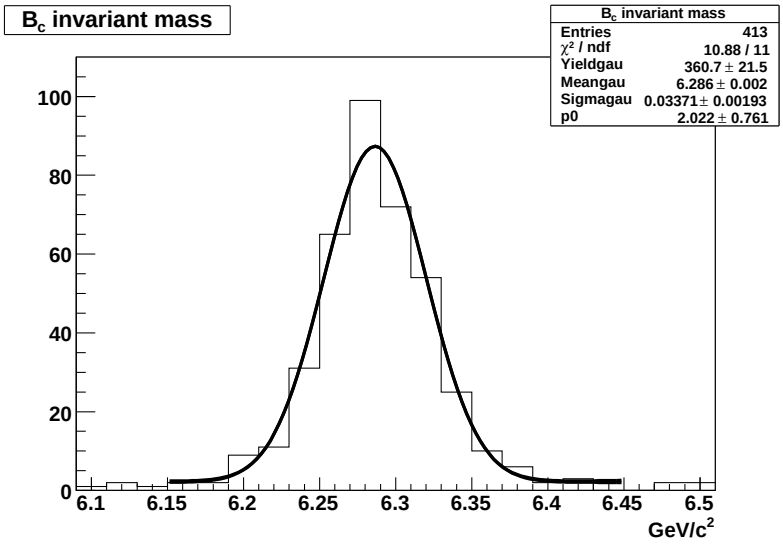

Figure 4.7.: Signal and background invariant mass distribution after the selection cuts at 1fb^{-1}.

	2D	3D
Yield	364±22	361±21
S/N	17.9±6.8	17.5±6.6
$M(B_C)$	6.289±0.002	6.286±0.002
$\Gamma(B_C)$	0.034±0.002	0.034±0.002

Table 4.5.: Mass and yield fit results from the analysis in the transverse plane (2D) and in the full space (3D)

4.7.2 B_C LIFETIME

As already recalled, lifetime results from Tevatron are carried out so far in the semileptonic $B_C \to J/\psi l\nu$ channel only; the presence of the undetected neutrino requires a Monte Carlo correction in the proper time distribution [57, 58]. A benefit of the $B_C \to J/\psi\pi$ channel is that it can be fully reconstructed, avoiding this correction.
The B_C lifetime determination proceeds selecting the events in the mass peak (see figure 4.7), within 3σ from the B_C mass nominal value ($6.2 - 6.4\ \text{GeV}/c^2$). The proper decay time can be calculated from L according to:

$$\begin{aligned} t_{2D} &= \frac{m_{B_c} L_{xy}}{c p_T}, \\ t_{3D} &= \frac{m_{B_c} L_{xyz}}{c p}. \end{aligned} \tag{4.2}$$

As already mentioned, L is the vector pointing to the secondary vertex from the primary. The decay vertex is obtained from the Kinematic Constrained Vertex Fitter and the interaction point from the Offline Primary Vertex Fitter.
In performing a lifetime analysis the effect of the acceptance, reconstruction efficiency and analysis cuts has to be taken into account. Figure 4.8 shows that these effects drastically reduce the reconstruction efficiency at short t.

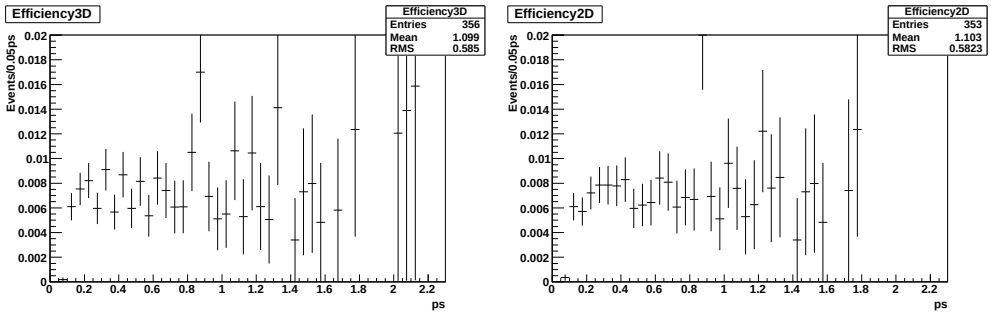

(a) (b)

Figure 4.8.: Efficency distribution in function of t, (a) 2D and (b) 3D analysis

Instead of the proper time variable t, the reduced proper time t' has been preferred, since the acceptance function is more uniform.
The reduced proper time

$$t'_{2D} = \frac{m_{B_c}(L_{xy} - N\sigma_{L_{xy}})}{cp_{\mathrm{T}}},$$
$$t'_{3D} = \frac{m_{B_c}(L_{xyz} - N\sigma_{L_{xyz}})}{cp}. \tag{4.3}$$

"starts the clock" at the minimum allowed time, after $N\sigma/c\beta\gamma$. The lifetime follows the same exponential wherever one chooses to start. So t' will follow an exponential with the same lifetime of t. The acceptance distributions, calculated as function of t' are shown in figure 4.9 for the 2D and 3D analysis.

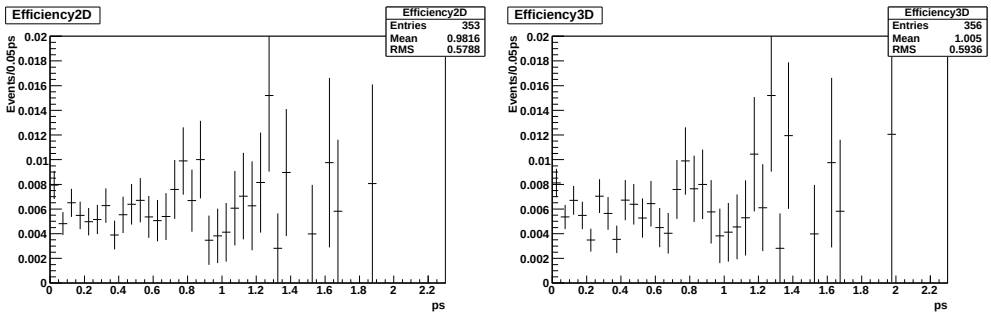

(a) (b)

Figure 4.9.: Efficency distribution in function of t', (a) 2D and (b) 3D analysis

A first estimate of the lifetime is performed using a binned maximum likelihood fit with a fitting function of the form:

$$F(t') = \varepsilon(t') \cdot e^{-\frac{t'}{\tau}+a} \tag{4.4}$$

where a is constant.
As shown in figure 4.9, the $\varepsilon(t')$ function is essentially constant and formula 4.4 reduces to a pure exponential. The resulting fit to the signal reduced proper time distribution is shown in figure 4.10.

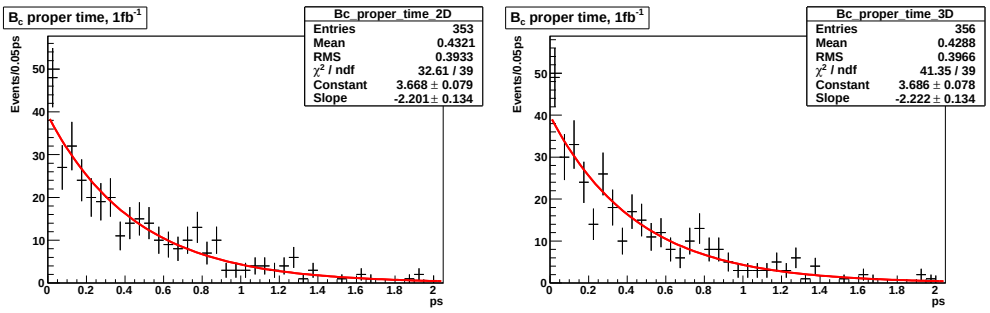

(a) (b)

Figure 4.10.: Signal reduced proper time distributions with exponential fit. (a) 2D and (b) 3D analysis. The fitted parameter *Slope* is equal to $-\frac{1}{\tau}$.

The pure signal lifetimes for the 2D and 3D analyses are $\tau_{2D} = 0.454 \pm 0.028$ ps and $\tau_{3D} = 0.450 \pm 0.027$ ps respectively.
A more precise estimate with the real data should take into account also the small deviation from the constant value of the acceptance distribution. A correction function is usually extracted from a detailed and high statistics Monte Carlo simulation.
In view of the real data analysis this procedure has been performed also in this study. However, because this method requires a large Monte Carlo sample (usually 100 times the data sample to avoid MC statistical fluctuations) the correction fuction has been obtained dividing the B_C sample in 2 subsets of 500 pb^{-1} of integrated luminosity each: the first is used to extract the correction function $f(t')$ (figure 4.11a and 4.11b), the other is used as data sample.
The observed number of events in a reduced proper time bin i is given by:

$$n_i = N_s \frac{f(t'_i)e^{-\frac{t'}{\tau}}}{\sum_i f(t'_i)e^{-\frac{t'}{\tau}}} \tag{4.5}$$

where N_s is the number of events in the signal region and $f(t'_i)$ is the correction function [76]. The calculated error of the reduced proper time is plotted in

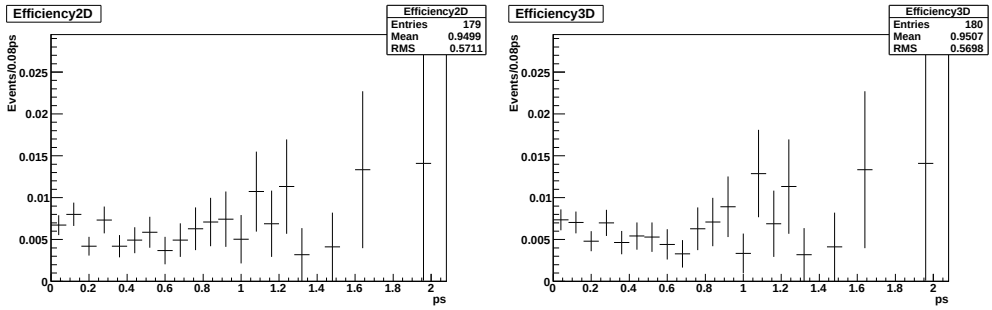

(a) (b)

Figure 4.11.: Correction function for t' in 2D (a) and 3D (b) analysis

figure 4.12. The mean value of $\sim$40 fs is $\sim 1/10$ of the B_c lifetime and this justifies the use of a multiplicative $f(t'_i)$ correction rather than an integral over a resolution factor. The $f(t')$, in figure 4.11, is obtained by dividing the simulated reconstructed B_c yield in each bin by the input decay exponential.

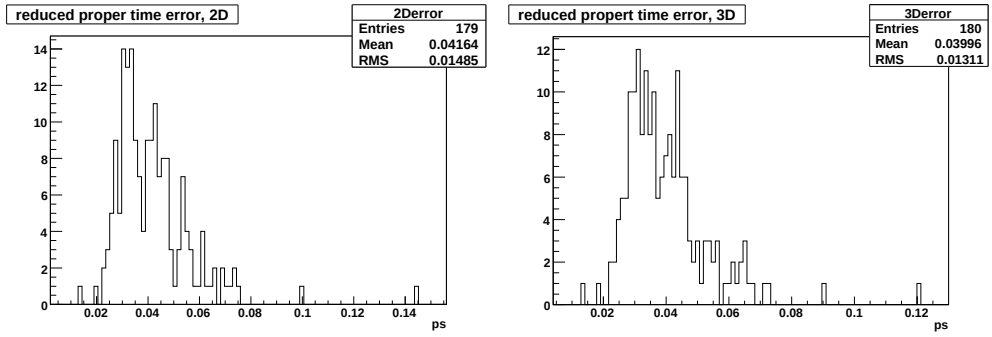

(a) (b)

Figure 4.12.: $\sigma(t')$ calculated for 2D (a) and 3D (b) analysis

A binned maximum likelihood fit to the 500pb^{-1} sample with the function

$$F(t') = N_s \frac{f(t') \cdot e^{-\frac{t'}{\tau}}}{\sum_i f(t'_i) \cdot e^{-\frac{t'_i}{\tau}}}$$

leads to

$$\tau_{2D} = 0.484 \pm 0.045 \text{ ps} \qquad \text{and} \qquad \tau_{3D} = 0.473 \pm 0.043 \text{ps}.$$

These results are influenced by the reduced statistics and the uncertainties of the correction function that determine the large error of the measurement ($\frac{\sigma(\tau)}{\tau} \sim 9\%$). Efficiency corrected data are shown in figure 4.13; the exponential function returned by the fit is superimposed.
These results are obtained for the signal sample only. In the real data analysis

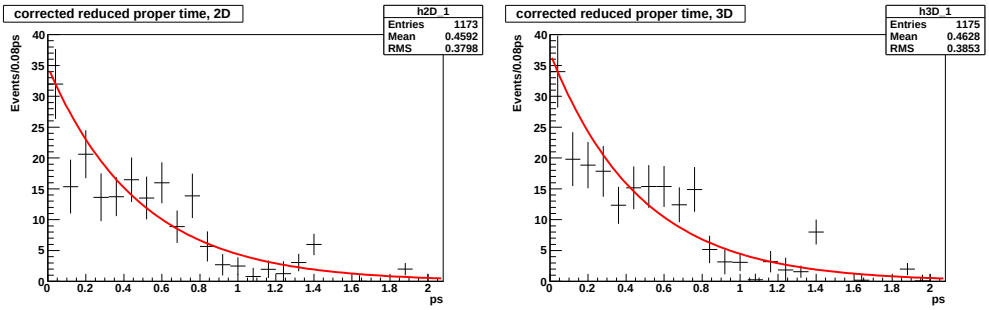

(a) (b)

Figure 4.13.: Efficiency corrected reduced proper time distribution and fitted exponential function, for 2D (a) and 3D (b) analysis

the proper time distribution will be composed of signal and background events. The binned likelihood allows direct use of the proper time distribution of the data above and below the B_C mass peak to represent the background underneath the signal. Thus, the number of events n_i in a reduced proper time bin i is given by:

$$n_i = (N_s - B)\frac{f(t_i')e^{-\frac{t'}{\tau}}}{\sum_i f(t_i')e^{-\frac{t'}{\tau}}} + B\frac{b_i}{\sum_i b_i} \tag{4.6}$$

where N_s is the total number of events in the signal region, B is the total number of background events in the signal region and b_i is the observed numbers of events in a reduced proper time bin i in the sideband histograms. The fit parameters are B and τ.

This method will be used with the real data sample. In the meanwhile, $f(t')$ is considered constant and the following results are based on this assumption (uncorrect analysis on the full 1 fb^{-1} statistics).

20 events of inclusive-b background have to be included in the analysis. These background events could be rejected by a stronger L/σ cut, i.e. $L/\sigma > 7$. These cut of course would reduce the B_C signal. To avoid the $\sim 30\%$ estimated loss in the signal yield, the cut is not applied and a background treatment has been preferred.

The origin of these events has been investigated through a Monte Carlo truth matching; the reconstructed J/ψ comes from the B (or B^0) while the third track, pion candidate, comes from the other b hadron or directly from the primary vertex. This leads to select only short living events and the proper time distribution has not the decay constant of B mesons.

The background behavior is, in general, inferred from the sideband regions; the poor statistics of our background sample unfortunately does not allow a simple treatment. The distribution shape can be obtained only relaxing the selection requirement: third track p_T >5 GeV/c in the mass range 5.5 – 7.1 GeV/c^2. The obtained distribution is in figure 4.14; it resembles an exponential with decay

constant $\sim 7\ \text{ps}^{-1}$.

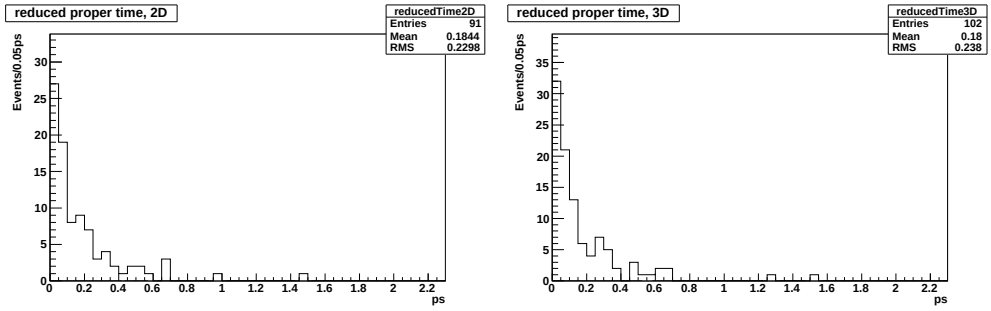

(a) (b)

Figure 4.14.: Inclusive-b background t' distribution from the looser selection (a) 2D and (b) 3D analysis.

From these histograms 20 events are randomly generate and added to the signal sample[6]. Other 20 different events are generated to be used as representative of the sideband regions. The fitting model, in equation 4.7, is composed of an exponential function and the background pdf from the sidebands.

$$M(t'|fsig) = N\left[fsig \cdot e^{-\frac{t'}{\tau}} + (1-fsig)\cdot HistPdf\right] \tag{4.7}$$

$fsig = \dfrac{S}{S+N}$ is the signal fraction (expected 0.946).
The fit returns

$$\tau_{2D} = 0.463 \pm 0.033 \text{ ps}, \qquad fsig = 0.941 \pm 0.037$$

and

$$\tau_{3D} = 0.459 \pm 0.032 \text{ ps}, \qquad fsig = 0.943 \pm 0.037.$$

These results are in a very good agreement whit the input values. The fitted distributions are shown in figure 4.15.
To complete the analysis, some additional studies are carried out. The influence of bin width, L/σ and $fsig$ are investigated to check the stability of the result. Figure 4.16 shows the lifetimes obtained varying the bin width from 30 to 120 fs. Table 4.6 reports lifetime measurements for different L/σ, from 1 to 5. No dependence on bin width and L/σ is visible at this statistical level.
The third study concerns the level of background, i.e. different $fsig$ value; it is generally expected that the real backgrounds encountered in collision data could be much higher than that predicted by Monte Carlo.
Before proceeding, few considerations on the sources and samples are necessary. The QCD $pp \to \mu X$ has too low statistics to draw final conclusions for this

[6]The class RooHistPdf of RooFit [77] has been used to obtain the pdf.

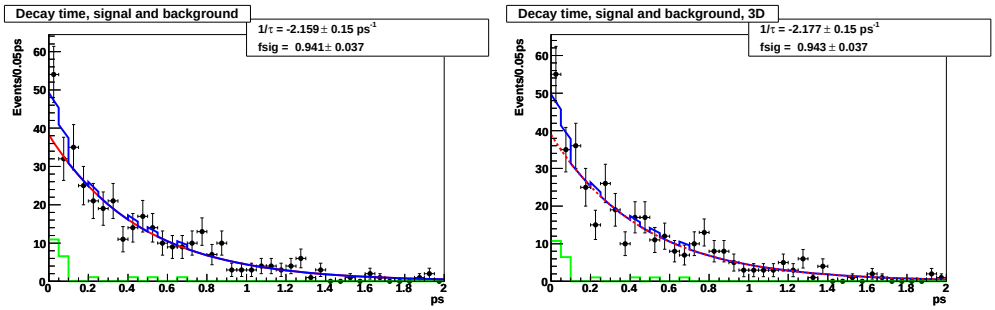

(a) (b)

Figure 4.15.: Signal plus background reduced proper time distribution in (a) 2D and (b) 3D analysis. The blue line corresponds to the fitting model, the red line is the exponential fuction and in green is the background histogram pdf

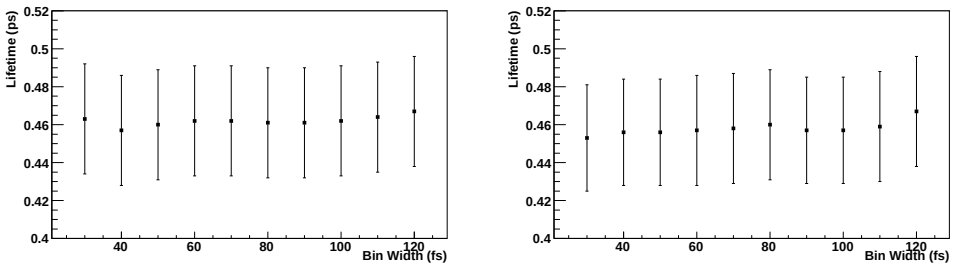

(a) (b)

Figure 4.16.: Lifetime results from bin width scan, $fsig$ is fixed to the expected value (0.946)

L/σ	lifetime 2D (ps)	lifetime 3D (ps)
1	0.460±0.026	0.455±0.026
2	0.470±0.029	0.460±0.028
3	0.461±0.029	0.459±0.029
4	0.473±0.032	0.470±0.031
5	0.471±0.033	0.471±0.033

Table 4.6.: Lifetime results from L/σ scan, $fsig$ is fixed to the expected values

analysis. As already pointed out, a looser selection study has been performed to investigate possible unaccounted QCD like background: events surviving the relaxed cuts come from b hadrons and are already included in the inclusive-b contribution. It seems, thus, reasonable to attribute possible large background

contamination to the inclusive-b source only.
Of course real data analysis could reveal additional contribution which will need to be carefully investigated before getting results.
For the purpose of this analysis, the inclusive-b contamination only has been raised up to $S/N = 1$, i.e. $fsig = 0.5$. Even in this disfavoured situation the lifetime measurement seems to be feasible; the result is compatible with the expected value within the error, precisely 0.475 ± 0.034 ps for both the 2D and the 3D analysis.
In presence of such a high contamination it would be interesting to gauge the level of background in some alternative way. An analytical parametrization is indeed possible. The final fit would then be performed using a function with a background modelled with τ_{bkg} exponential decay constant as obtained from sidebands: $\sim 1/7$ ps.

$$M(t'|fsig) = N\left[fsig \cdot e^{-\frac{t'}{\tau}} + (1 - fsig) \cdot e^{-\frac{t'}{\tau_{bkg}}}\right] \tag{4.8}$$

This parametrization leads to $\tau_{2D} = 0.454 \pm 0.032$ ps and $\tau_{3D} = 0.453 \pm 0.032$ ps. The fitted model is reported in figure 4.17; the single components are individually shown.

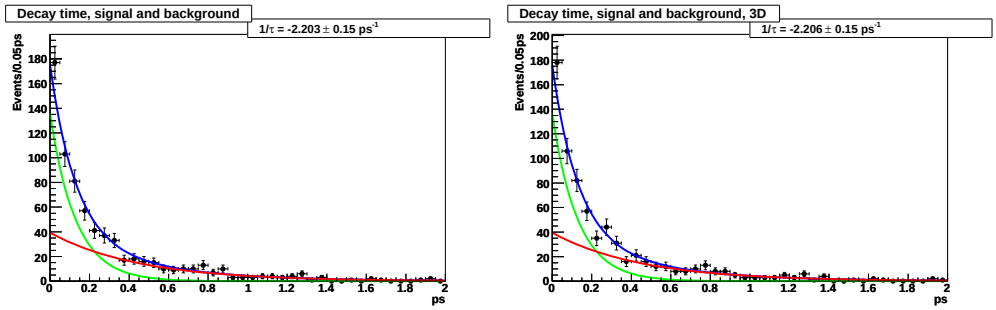

(a) (b)

Figure 4.17.: Signal plus background proper time distribution in presence of large($fsig = 0.5$) background for (a) 2D and (b) 3D analysis. The blue line corresponds to the fitting model, the red line is the B_C exponential fuction and in green is the background exponential function

A general remark is relevant here: the $\tau(B_C)$ input value is based on Tevatron results. It has been already recalled that this measurements were performed after a Monte Carlo correction. It is worth investigating the feasibility of the analysis in CMS for different lifetime; the shorter the lifetime is, the more complicated is the disentangle of the signal and background component.
A lifetime of 0.23 ps (half of the PDG value) is considered. The analysis of 1fb^{-1} events processed through the full simulation chain leads to ~ 215 B_C

mesons: $\tau_{2D}^{Short} = 0.220 \pm 0.016$ ps and $\tau_{3D}^{Short} = 0.218 \pm 0.016$ ps.
The addition of the background events does not compromize the analysis. The results are:

$$\tau_{2D}^{Short} = 0.228 \pm 0.020 \text{ ps} \qquad \text{and} \qquad fsig = 0.853 \pm 0.125$$

and

$$\tau_{3D}^{Short} = 0.225 \pm 0.019 \text{ ps} \qquad \text{and} \qquad fsig = 0.891 \pm 0.103.$$

The distributions are plotted in figure 4.18

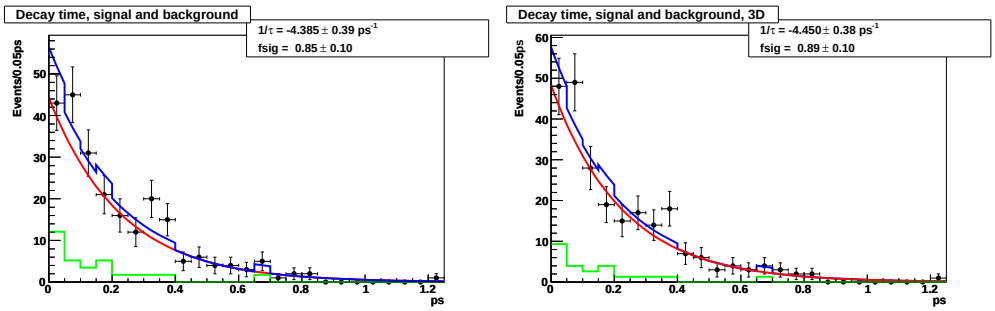

(a) (b)

Figure 4.18.: Short living B_C signal and background reduced proper time distribution for (a) 2D and (b) 3D analysis. The blue line corresponds to the fitting model, the red line is the B_C exponential fuction and in green is the background exponential function

If $fsig$ is fixed to the true value (0.915) a slightly better precision can be obtained, as expected; in facts, the fit returns $\tau_{2D}^{Short} = 0.224 \pm 0.016$ ps and $\tau_{3D}^{Short} = 0.223 \pm 0.016$ ps.
In conclusion, these result support the feasibility of the analysis and its robustness at 1 fb^{-1}. The B_C mass determination can be carried out with a yield at least 4 times larger than those from Tevatron and the lifetime can be measured, for the first time in the $B_C \to J/\psi\pi$ channel, with a statistical precision of $\sim 7\%$.

4.8 ANALYSIS AT 200 pb^{-1}

According to the 2009 Chamonix schedule, the collected statistics of the first year will be $\sim$200 pb^{-1}. At this integrated luminosity $\sim$ 12000 B_C mesons will be produced and decay in the exclusive channel $B_C \to J/\psi\pi$, $J/\psi \to \mu^+\mu^-$, over the full B_C p_T spectrum and in the full 4π solid angle.
The results at 1fb^{-1} suggest that a competitive analysis could be performed in the B_C sector already at 200pb^{-1}. A complete study for this luminosity is here presented.

4.8.1 MASS MEASUREMENT

$\sim$100 B_C and $\sim$78 background events (68 prompt-J/ψ and 10 inclusive-b) are expected just after the three track vertex reconstruction. The invariant mass distribution is shown in figure 4.19: the final signal yield is 100 ± 18 B_C, $S/N = 4.05 \pm 1.90$, the mass and Γ are 6.289 ± 0.006 GeV/c^2 and 0.044 ± 0.008 GeV/c^2 respectively (see table 4.7).

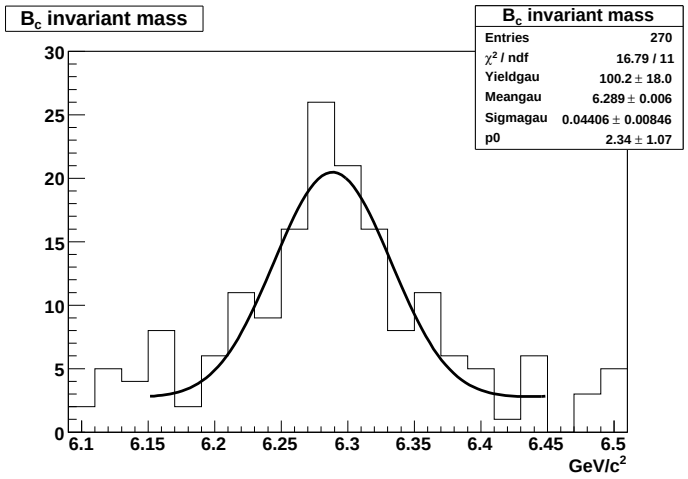

Figure 4.19.: Signal and background invariant mass distribution at 200 pb^{-1}

The additional request on cosine and L/σ selects $\sim$ 65 B_C and 8 background

Yield	100$\pm$18
S/N	4.05$\pm$1.90
M(B_C)	6.289$\pm$0.006
Γ(B_C)	0.044$\pm$0.008

Table 4.7.: Mass fit results at 200 pb^{-1}

events.
Figure 4.20 shows the mass distribution of events surviving the complete selection. The measured yield is 62 ± 10, $S/N = 7.2 \pm 5.5$ and a mass $M(B_C) = 6.283 \pm 0.004$ GeV/c^2 and $\Gamma(B_C) = 0.032 \pm 0.006$ GeV/c^2, reported in table 4.8.1.
This B_C yield, and conseguentely the statistical precision, are comparable to the current CDF and D0 collected sample, namely $\sim$ 100 and $\sim$ 50 mesons.

4.8.2 LIFETIME MEASUREMENT

The lifetime study on the B_C sample gives:

$$\tau_{2D} = 0.467 \pm 0.067 \text{ ps} \qquad \text{and} \qquad \tau_{3D} = 0.459 \pm 0.065 \text{ ps},$$

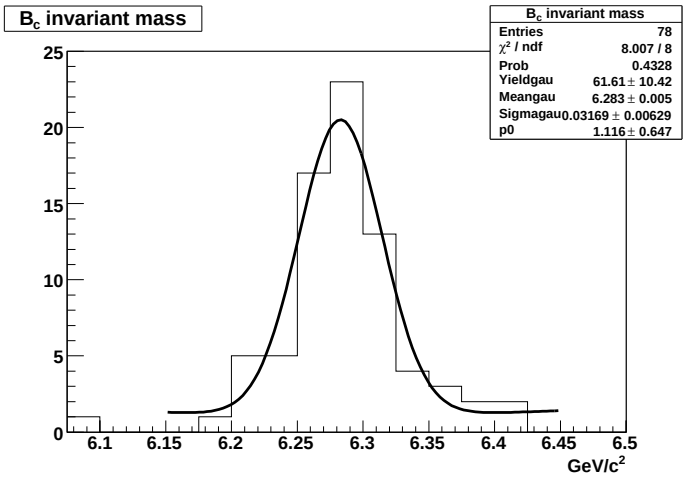

Figure 4.20.: Signal and background invariant mass distribution after all the selection cuts at 200 pb^{-1}.

	2D	3D
Yield	62±10	63±11
S/N	7.2±5.5	7.4±6.2
M(B_c)	6.284±0.005	6.283±0.004
$\Gamma(B_c)$	0.034±0.005	0.032±0.006

Table 4.8.: Mass fit results at 200 pb^{-1} after all the selection cuts

the fitted reduced proper time distribution is shown in figure 4.21

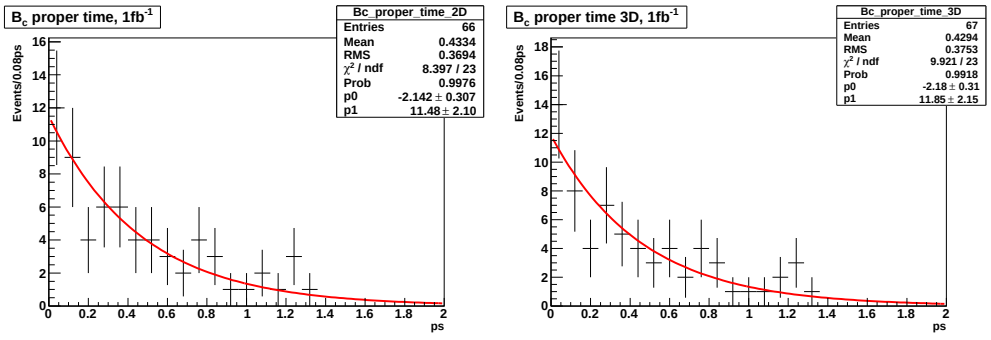

(a) (b)

Figure 4.21.: Signal reduced proper time at 200 pb^{-1}

9 ± 6 background events from inclusive-b are expected from the fit to the mass invariant plot the mass plot in figure 4.20. Fixing $fsig$ to its expected value (0.878), the results obtained for the 2D and 3D analyses are:

$$\tau_{2D} = 0.456 \pm 0.064 \text{ ps} \qquad \text{and} \qquad \tau_{3D} = 0.449 \pm 0.062 \text{ ps}.$$

The low statistics does not allow to let the fsig parameter freely floating in the fit. $fsig$ is thus moved within its error (0.878 ± 0.083) to gauge the possible variation in the lifetime measurement.
The lifetime spread is found to be small and within the error. In particular, for the extreme $fsig$ values ($fsig$=0.80 and $fsig$=0.96), the results are:

$$\tau_{2D} = 0.479 \pm 0.072 \text{ ps}, \qquad \tau_{3D} = 0.470 \pm 0.069 \text{ ps},$$
$$\tau_{2D} = 0.455 \pm 0.063 \text{ ps}, \qquad \tau_{3D} = 0.447 \pm 0.061 \text{ ps}.$$

It is particularly relevant at this luminosity to investigate the capability to extract the signal even in presence of a higher background. Following the same procedure adopted for the lifetime measurement at 1 fb^{-1} the inclusive-b contribution has been raised $S/N = 1$ ($fsig = 0.5$). The lifetime result is $\tau = 0.481 \pm 0.075$ ps for both 2D and 3D analyses.
In conclusion, at 200 pb^{-1} of integrated luminosity, a signal of $\sim 65 - 100$ events, according to the different cuts, can be reconstructed in CMS. Yield and mass measurements are competitive with the current Tevatron results in the same channel. A preliminary determination of lifetime in the full reconstructed $J/\psi\pi$ mode seems to be feasible with a statistical precision of $\sim 15\%$

4.9 DOUBLE MUON TRIGGER RESULTS

As anticipated in section 4.6, just after a first phase with the single muon trigger threshold set at $p_T > 3$ GeV/c, a double muon trigger will be more convenient for this analysis. The single muon HLT has been preferred for this study because of the ongoing optimization of the HLT_DoubleMu3.
However, for completeness and in view of the real data analysis, a study was performed to verify the consistency of the results with the double muon trigger. This analysis clones the HLT_Mu3 study on 1 fb^{-1}luminosity.
After all the selection cuts, 272 B_C events are reconstructed. The reduction of the final signal yield is $\sim 25\%$. This can be abscribed to the HLT_DoubleMu3 trigger. Indeed, ~ 2000 J/ψ are filtered by the trigger itself which have to be compared with ~ 2700 reconstructed through the HLT_Mu3 plus the J/ψ mass request. Signal and background invariant mass is shown in figure 4.22 and in table 4.9
The lifetime determination is performed on the reduced proper time distribution for signal plus background shown in figure 4.23.
The fitted parameters are:

$$\tau_{2D} = 0.449 \pm 0.035 \text{ ps} \qquad \text{and} \qquad fsig = 0.955 \pm 0.040$$

for the 2D analysis and

$$\tau_{3D} = 0.445 \pm 0.035 \text{ ps} \qquad \text{and} \qquad fsig = 0.958 \pm 0.041$$

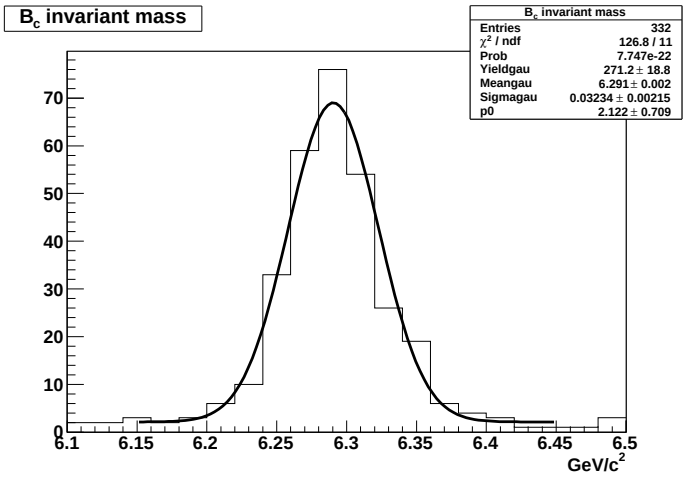

Figure 4.22.: Signal and background invariant mass distribution after all the selection cuts usign the HLT_DoubleMu3.

	2D	3D
Yield	271±19	273±19
S/N	16.3±7.3	16.9±7.4
M(B_C)	6.291±0.002	6.291±0.002
$\Gamma(B_C)$	0.032±0.002	0.032±0.002

Table 4.9.: Mass fit results after all the selection cuts using the trigger Double_Mu3 .

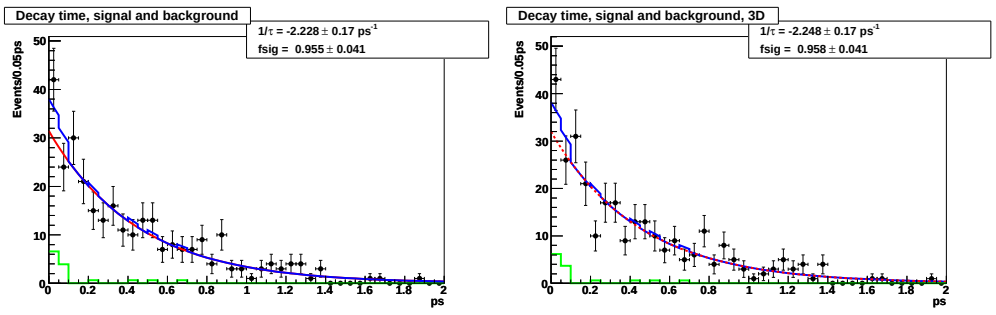

(a) (b)

Figure 4.23.: Signal and background reduced proper time distribution using the HLT_DoubleMu3 in the (a) 2D and (b) 3D analysis. The blue line corresponds to the fitting model, the red line is the exponential fuction and in green is the background pdf

from the tridimensional study.
Fixing the signal fraction to the expected values $fsig = 0.932$, the lifetime results are:

$$\tau_{2D} = 0.457 \pm 0.033 \text{ ps} \qquad \text{and} \qquad \tau_{3D} = 0.455 \pm 0.032 \text{ ps}.$$

In the extreme condition of a background equal to the signal ($\sim$ 215 background events), fixing $fsig = 0.5$, the measured lifetime is

$$\tau_{2D} = 0.478 \pm 0.039 \text{ ps} \qquad \text{and} \qquad \tau_{3D} = 0.480 \pm 0.039 \text{ ps}.$$

The analysis carried out with HLT_DoubleMu3 does not show any inconsistency with respect to the HLT_Mu3. The double muon trigger inefficiency is currently under study and will be hopefully recovered in the next software releases. This study has checked that the B_C analysis can be successfully performed with the HLT_DoubleMu3 as well, which is the trigger configuration foreseen for the CMS physics runs.

CHAPTER 5

BCVEGPY IN CMSSW

The B_C production rate, requiring the simultaneus presence of a b-$\bar{b}$ and a c-$\bar{c}$ couple, is $\sim 10^{-3}$ with respect to the b-$\bar{b}$ production; thus, in PYTHIA only one B_C is produced out of $\sim 10^6$ p-p interactions. In order to study the B_C physics a dedicated generator is necessary to enhance the event generation efficiency. A generator is actually available: BCVEGPY [59]; the hadronic production of the B_C meson proceeds through the dominant subprocess $gg \rightarrow B_C\ (B_C^*) + \bar{c} + b$.
The integration in the official simulation software of the CMS experiment has been developed during this thesis and BCVEGPY is now a package of CMSSW[1]. The procedure is presented here after a brief introduction of the original generator.

5.1 BCVEGPY

BCVEGPY is a hadronic production program for B_C (B_C^*) mesons based on a complete calculation approach: the B_C production is computed at the lowest order (α_s^4) in terms of the dominant subprocess of perturbative QCD (pQCD) $gg \rightarrow B_C(B_C^*) + \bar{c} + b$. The calculation does not need any experiemental input, the estimates of the production are totally from theoretical predictions. The non-perturbative part, the c and $\bar{b}$ quarks combining into B_C (B_C^*), is calculated by means of the potential model for heavy quark-antiquark systems.
According to pQCD there is another production mechanism by quark pair annihilation subprocess $q\bar{q} \rightarrow B_C\ (B_C^*) + \bar{c} + b$. Nevertheless, the contribution from this mechanism is negligible compared to the dominant one: the "luminosity" of gluons is much higher than that of quarks in pp collisions (LHC) and there is a suppression factor due to the virtual gluon propagator in the annihilation.
To make the program compact, the authors extend the symmetries for the am-

[1] Available since CMSSW_3_1_0

plitudes corresponding to the Feynman diagrams for the process $gg \to B_C(B_C^*) + \bar{c} + b$, neither considering the color factors nor distinguishing the flavours of the fermion lines, and grouping these diagrams into only a few typical ones. Then the fermion lines are simplified by spinor products. The detailed description can be found in the generator paper[59]. The resulting program is very compact and potentially reduces the execution time significantly.
It is written in form of a Fortran package in the format of PYTHIA6 (the Fortran version of PYTHIA [78, 79]). The variables are stored in the same common block and it is, thus, easy to implement in PYTHIA6 as an external generator.

5.2 CUSTOMIZED VERSION

The first step for using BCVEPGY in the CMS simulation package has been the integration of the last version of the generator (available on the author's web site [80]) in a customized version of CMSSW installed on the computer cluster in Milan.
Before doing this, the generator has been run as a stand alone program to reproduce the published distributions [60] (here reported in figure 5.1). The reference plots are compared to the distributions in figure 5.2, obtained running the generator at the Tevatron energy. The plots are in very good agreement, so the generator has been set and run in the proper way.

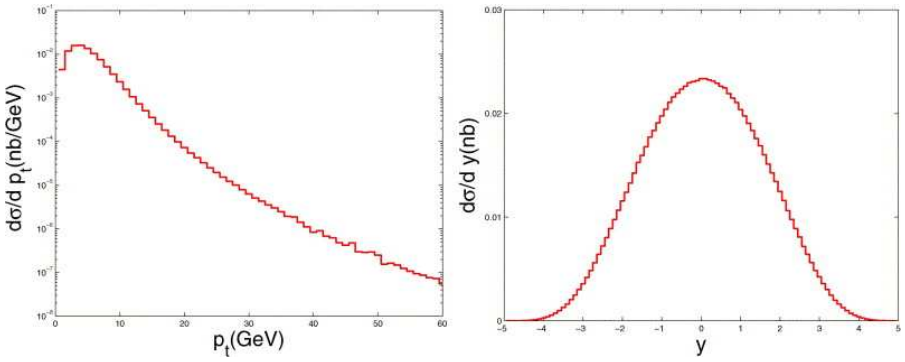

Figure 5.1.: $\frac{d\sigma}{dp_T}$ and $\frac{dy}{dp_T}$ from [60]

A first attempt to incorporate BCVEGPY into CMSSW was done without introducing any modification in the original program: all the Fortran routines are included in `Pythia6Interface` package and the interface to PYTHIA6 is modified to accomodate the BCVEGPY use. The generator is activated and controlled by the user through the CMSSW configuration file.
Thanks to the generator format, that is the same as PYTHIA6, the B_C events are stored in the PYTHIA6 common blocks.
The output of the B_C generation using this new interface is compared to the output of the BCVEGPY generator (run as a stand alone program and simu-

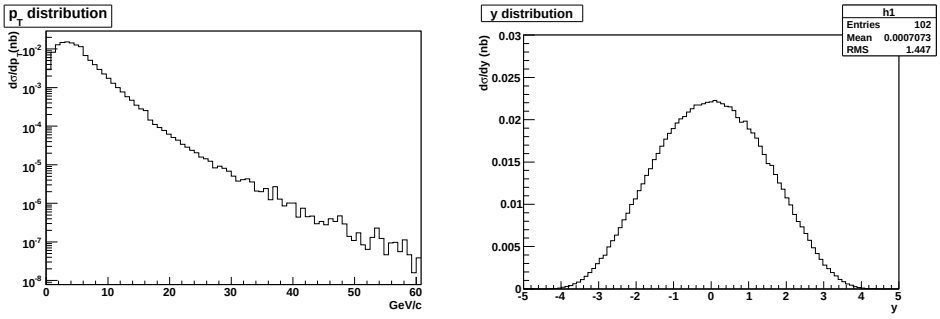

(a) (b)

Figure 5.2.: $\frac{d\sigma}{dp_T}$ and $\frac{dy}{dp_T}$ from the generator

lating p-p interactions). The p_T and the η distributions are considered at the generation level before of any detector simulation. From figure 5.3, one can reasonably conclude that the inclusion in CMSSW has been safely and correctly done without modifying the generator output.

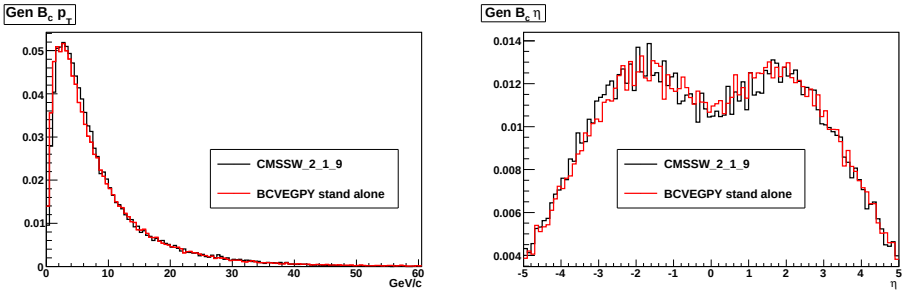

(a) (b)

Figure 5.3.: p_T and η from the generator in CMSSW (black) and the generator run as stand alone (red).

5.3 BCVEGPY IN CMSSW

The initial idea for the integration in the CMS official software reflected the local implementation scheme: the creation of a library with the fortran routines and the modification of the PythiaSource.cc. This approach was completely changed interacting with the Generator Working Group (Generator WG) of the CMS Collaboration which suggests to separate the B_C production from the hadronization process to allow an easy interface to different hadronizer models. Since BCVEGPY emulates a matrix element (ME) generator, the new idea is to use it to generate "parton" configuration (that is $B_C + \bar{c} + b$) only and feed it to

PYTHIA6 for the hadronization in a second step. The "parton" information are written out in a file in the Les Houches Accord format (file LHE, figure 5.4): a standard file format proposed to store process and event information. These information are primarily output from parton level generator for further use by the general-purpose Monte Carlo programs.
Even if the output file contains a bound state, the B_C meson, it can be read and hadronized by the Pythia6Interface.

5.3.1 PACKAGE GENEXTENSIONS

BCVEGPY is integrated in CMSSW in the package `GenExtensions`.
All the code is in the `bin/BCVEGPY` subdirectory and the program, named BcGenerator, is built as a binary. The generator parameters are passed to BCVEGPY through a namelist: `bcvegpy_set_par.nam`
These parameters (see figure 5.5) control the energy of the beam, the type of the beam (p-p or p-$\bar{p}$), the mass of the quarks, inibit or not the shower with PYTHIA and write the LHE file, set the number of events and the precision of the calculation in VEGAS.
VEGAS [81] is a program used for the calculation of the square of amplitudes of the diagrams. It optimizes the sampling of the phase space points for integration but this requirement is highly CPU time consuming. Higher values of `NVEGCALL` and `NVEGITMX` will make the result more accurate. More specific description of the parameter can be found in [82].
Using the parameter set in figure 5.5, the LHE file, containing 250000 events, will be produced in 1.5 hour on a dual Intel Xeon quadcore with 16Gb RAM.
Then the output file is read by PYTHIA for the hadronization. To check that the interface to CMSSW does not compromize anything of the original generator, the usual distributions of p_T and η are compared to those obtained with the local customized version of CMSSW. The distributions in figure 5.6 show that the interface has been performed correctly.
In conclusion, the integration of BCVEGPY has been performed successfully and the generator is available in the official software since CMSSW_3_1_0. In addition, it is worth noting that this generator has been the first package written in this new two step (generation-hadronization) scheme and has been used as template for the other external generators (HARDCOL [83] and EDDE [84]).

```
<LesHouchesEvents version="1.0">
<!--
File generated with PYTHIA 6.419
-->
<init>
    2212    2212  5.000000E+03  5.000000E+03     0     0    7    7    3    1
  3.514408E+06  0.000000E+00  0.000000E+00  1001
</init>
<event>
     5  1001  1.000000E+00  8.226610E+00  0.000000E+00  2.096463E-01
       21   -1    0    0  503  502  0.00000000000E+00  0.00000000000E+00  1.69714629l9E+01  1.69714629l9E+01  0.00000000000E+00 0. 9.
       21   -1    0    0  502  501  0.00000000000E+00  0.00000000000E+00 -2.39715023l4E+01  2.39715023l4E+01  0.00000000000E+00 0. 9.
      541    1    1    2    0    0  7.75035986666E-01  5.25001342l5E+00 -1.18686013l8E+01  1.44409423l1E+01  6.28600000000E+00 0. 9.
        5    1    1    2  503    0 -5.83608948l2E-01 -3.60443978l5E+00  1.49715846l3E+01  1.61706812l7E+01  4.90000000000E+00 0. 9.
       -4    1    1    2    0  501 -1.91427037l5E-01 -1.64557364l0E+00 -1.01030227l0E+01  1.03313416l5E+01  1.38600000000E+00 0. 9.
</event>
<event>
     5  1001  1.000000E+00  6.477926E+00  0.000000E+00  2.232967E-01
       21   -1    0    0  503  502  0.00000000000E+00  0.00000000000E+00  1.89543451l0E+01  1.89543451l0E+01  0.00000000000E+00 0. 9.
       21   -1    0    0  502  501  0.00000000000E+00  0.00000000000E+00 -1.71389319l2E+01  1.71389319l2E+01  0.00000000000E+00 0. 9.
      541    1    1    2    0    0  1.42774578l0E+00 -6.41305102l2E-01 -1.24537757l5E+01  1.40378080l4E+01  6.28600000000E+00 0. 9.
        5    1    1    2  503    0 -1.17528206l9E+00  1.56199749l2E+00  1.75729486l7E+01  1.83477423l1E+01  4.90000000000E+00 0. 9.
       -4    1    1    2    0  501 -2.52463719l4E-01 -9.20692394l6E-01 -3.30375971l9E+00  3.70772661l3E+00  1.38600000000E+00 0. 9.
</event>
```

Figure 5.4.: LHE events produced by the B_C generator in CMSSW

```
$bcvegpy_set_par
  ENERGYOFTEVA = 1.96d+3
  ENERGYOFLHC  = 1.00d+4
  pmassb       = 4.9d0
  pmassc       = 1.386d0
  naccel       = 2
  i_shower     = 0
  i_mix        = 1
  NUMOFEVENTS  = 250000
  NVEGCALL     = 50000
  NVEGITMX     = 10
  ibcrandom    = 19780505
$End
```

Figure 5.5.: Content of bcvegpy_set_par.nam

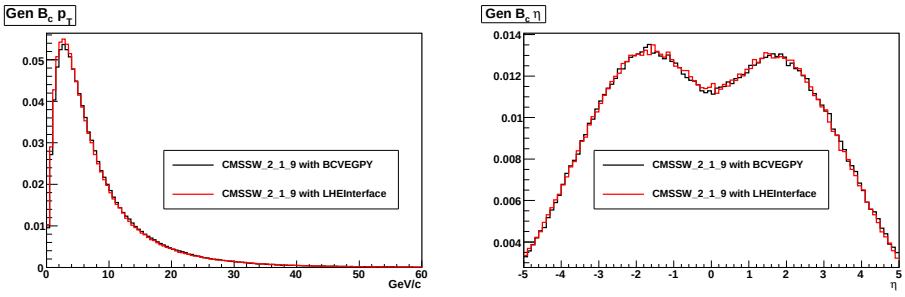

(a) (b)

Figure 5.6.: p_T and η from the generator in the local customized CMSSW (black) and using the LHE file (red).

CONCLUSIONS

The CMS forward pixel detector perfomance at high absorbed dose and the feasibility study of the B_C meson analysis in the CMS experiment have been treated in this thesis.
The forward pixel detector is close to the interaction point and, due to the short distances, lives in a harsh environment. To investigate the long term performance a detector module has been tested on a beam at Fermilab, after an irradiation up to 45 Mrad.
The major deterioration is a reduction of $\sim 25\%$ of the signal released by a minimum ionizing particle. Despite this, the detection efficiency remains very high, $\sim 99\%$, even at an equivalent threshold of $\sim 3300\ e^-$ and shows only a marginal drop near the pixel corners for the most irradiated region. An apparent increase of the charge collection efficiency has been observed in the inter-pixel region at high absorbed dose; in the presence of the p-stop ring break it alters the symmetry of the η-distribution. In principle, this effect has to be taken into account in the extraction of the coordinate from the spatial charge distribution. Despite these damage the pixel detector remains fully operational after years inside the LHC. This good long term performance assures the precise vertex and track reconstruction necessary to perform the CMS physics program.
The B physics is one of the main topics of this program since the first phase of the experiment. The advantage of the hadron collider is the possibility, thanks to the energy available in the interaction, to investigate the full spectrum of b-hadrons including those states, such B_S, B_C and b-baryons not available at the B-factories.
The feasibility of the $B_C \to J/\psi\pi$ analysis has been investigated in the second part of this thesis.
Thanks to the high efficiency in muon identification and reconstruction, the analysis starts from the J/ψ reconstruction and, in a second step, a third non-muonic track is added to form the B_C decay vertex.
According to the Monte Carlo predictions, in 1 fb^{-1} of integrated luminosity, a mass measurement $M(B_C) = 6.287 \pm 0.002$ GeV with a width $\Gamma(B_C) = 0.032 \pm 0.002$ GeV can be carried out with an expected yield of 451 ± 27 B_C, that corresponds to a total efficiency of $0.75 \pm 0.05\%$.
A lifetime measurement can be performed for the first time in the fully recon-

structed decay channel $B_C \to J/\psi\pi$ and resulted to be $\tau = 0.463 \pm 0.033$ ps.
CMS can obtain a preliminary result at 200 pb^{-1}: ~ 100 B_C leads to a mass measurement $M(B_C) = 6.289 \pm 0.006$ with a width $\Gamma(B_C) = 0.044 \pm 0.008$ GeV already competitive with the current from Tevatron. A lifetime of $\tau = 0.456 \pm 0.064$ ps can be extracted from the proper time distribution of the B_C candidates.
Concluding, the CMS experiment can collect a B_C sample comparable to the pubblished statistics in the $B_C \to J/\psi\pi$ channel already at 200 pb^{-1} of integrated luminosity.
At 1 fb^{-1} the estimated yield is approximatively four time bigger than that analysed by CDF for the mass measurement in this channel, and the lifetime is expected to be measured with a statistical precision of $\sim 7\%$.
These promising results suggest that the CMS experiment can contribute to shed some light onto the heavy flavour dynamics sector.

APPENDIX A

CMSSW DEFINITIONS

A.1 MUONS

GLOBAL — For each standalone muon track, a search for tracks matching it among those reconstructed in the inner tracking system (referred to as "tracker tracks", "inner tracks" or "silicon tracks") is performed, and the best-matching tracker track is selected.

STAND ALONE — Objects reconstruct using track fits in the muon system, which are performed using segments and hits from DTs, CSCs and RPCs and are based on the Kalman filter technique.

TRACKER — An approach complementary to the global-muon reconstruction consists in considering all tracker tracks to be potential muon candidates and in checking this hypothesis by looking for compatible signatures in the calorimeters and in the muon system. Tracker tracks identified as muons by this method are referred to as "tracker muons".The default criteria for tagging a tracker track as "tracker muon" are very loose: every track with p > 3 GeV and pT > 1.5 GeV matched with at least one segment in the muon stations.

A.2 HLT

All the HLT require particles (one or more) in the η acceptance of the detector. For muons, it is limited from the CSC L1 Trigger that covers the region:

- η_{MIN} : -2.4

· η_{MAX} : 2.4

HLT_DoubleMu3	Muon HLT requiring: Number of muons: 2, p_T threshold (GeV): 3
HLT_Mu3	Muon HLT Number of muons: 1, p_T threshold (GeV): 3

APPENDIX B

ACRONYMS

ADC	Analog to Digital Converter
APD	Avalanche PhotoDiode
ASIC	Application Specific Integrated Circuit
BR	Branching Ratio
CKM	Cabibbo-Kobayashi-Maskawa
CMS	Compact Muon Solenoid
COM	Color Octet Model (in NRQCD)
CSC	Cathode Strip Chamber
CSM	Color Singlet Model (in NRQCD)
DAQ	Data AcQuisition
DT	Drift Tube
EB	Electromagnetic Barrel calorimeter
ECAL	Electromagnetic CALorimeter
EE	Electromagnetic Endcap
FSI	Final State Interaction
FPGA	Field Programmable Gate Array
FPIX1	Chip from the BTeV experiments. Used as telescope detector

HCAL	Hadron CALorimeter
HF	Hadron Forward detector
HI	Heavy Ion
HO	Hadronic Outer detector
HPD	Hybrid PhotoDiode
HQET	Heavy Quark Effective Theory
ID	IDentifier
LHC	Large Hadron Collider
LHE	Les Houches Event
MB	Muon Barrel
ME	Matrix Element
MSSM	Minimal Supersymmetric Standard Model
NLO	Next to Leading Order
NP	New Physics
NRQCD	Non Relativistic Quantum Chromo Dynamics
OPE	Operator Product Expansion
PDF	Parton Distribution Function
PM	Potential Model
pQCD	Perturbative QCD
PS	Proton Synchrotron
QCD	Quantum Chromo Dynamics
ROC	ReadOut Chip
RPC	Resistive Plate Chamber
SM	Standard Model
S/N	Signal to Noise ratio
SPS	Super Proton Synchrotron

SR	Sum Rules
TEC	Tracker EndCap
TIB	Tracker Inner Barrel
TID	Tracker Inner Disk
TOB	Tracker Outer Barrel
VPT	Vacuum PhotoTriode
WG	Working Group
WLS	WaveLength-Shifter

BIBLIOGRAPHY

[1] D. Acosta *et al.*, Cms physics technical design report volume i: Detector performance and software, 2006.

[2] D. Boussard *et al.*, *The Large Hadron Collider: conceptual design*, CH-1211 Geneve 23, Suisse, 1995.

[3] The CMS collaboration, Journal of Instrumentation **3**, S08004 (2008), doi: 10.1088/1748-0221/3/08/S08004.

[4] CMS collaboration, *The Muon Project Technical Design Report*, CH-1211 Geneve 23, Suisse, 1997.

[5] CMS collaboration, The TriDAS project, technical design report. Volume 1: The level-1 trigger, http://cdsweb.cern.ch/record/706847, CERN-LHCC-2000-038.

[6] CMS collaboration, The TriDAS project, technical design report. Volume 2: Data acquisition and high-level trigger technical design report, http://cdsweb.cern.ch/record/578006, CERN-LHCC-2002-026.

[7] I. Magrans de Arbril, C.-E. Wulz, and J. Varela, IEEE Trans. Nucl. Sci. **53**, 474 (2006).

[8] R. Covarelli, CERN Report No. CMS-CR-2009-188. CERN-CMS-CR-2009-188, 2009 (unpublished).

[9] H. Kästli *et al.*, Nuclear Instruments and Methods in Physics Research Section A: Accelerators, Spectrometers, Detectors and Associated Equipment **565**, 188 (2006), Proceedings of the International Workshop on Semiconductor Pixel Detectors for Particles and Imaging - PIXEL 2005.

[10] G. Cerati *et al.*, Nucl. Instr. and Meth. **A600**, 408 (2009).

[11] P. Bhat, N. Mokhov, and A. Singh, Beam radiation simulation in CMS, CMS Internal Report, 2007.

[12] L. Uplegger *et al.*, Nuclear Science Symposium Conference Record, 2004 IEEE **1**, 1 (2004).

[13] D. Menasce, M. Turqueti, and L. Uplegger, Nuclear Instruments and Methods in Physics Research Section A: Accelerators, Spectrometers, Detectors and Associated Equipment **579**, 1141 (2007).

[14] M. Kobayashi and T. Maskawa, Prog. Theor. Phys. **49**, 652 (1973).

[15] S. W. Herb *et al.*, Phys. Rev. Lett. **39**, 252 (1977).

[16] A. De Roeck, A. Ball, M. Della Negra, L. Foà, and A. Petrilli, *CMS physics: Technical Design Report* (CERN, Geneva, 2006).

[17] M. Battaglia *et al.*, The CKM Matrix and the Unitarity Triangle, CERN-2003-002-corr, hep-ph/0304132.

[18] CDF/D0 $\Delta\Gamma_s$, β_s Combination Working Group, Combination of D0 and CDF Results on $\Delta\Gamma_s$ and the CP-Violating Phase $\beta^{J/\psi\phi_s}$, 2009, D0 Note 5928-CONF.

[19] R. Fleischer, Physics Reports **370**, 537 (2002).

[20] N. Magini, Nuclear Physics B - Proceedings Supplements **170**, 146 (2007), Proceedings of the 11th International Conference on B-Physics at Hadron Machines - Beauty 2006.

[21] Particle Data Group, http://pdg.lbl.gov.

[22] M. Artuso *et al.*, Eur. Phys. J. C **57**, 309 (2008).

[23] CDF collaboration, Search for $B_s^0 \to \mu^+\mu^-$ and $B_d^0 \to \mu^+\mu^-$ decays in 3.7fb^{-1} of $p\bar{p}$ collisions with CDF II, 2009, CDF Public Note 9892.

[24] D0 collaboration, A new expected upper limit on $b(B_s^0 \to \mu^+\mu^-)$ using 5fb^{-1} of RunII data, 2009, D0 Note 5906-Conf.

[25] M. Neubert, Physics Reports **245**, 259 (1994).

[26] I. Bigi, M. A. Shifman, and N. Uraltsev, Ann. Rev. Nucl. Part. Sci. **47**, 591 (1997).

[27] G. T. Bodwin, E. Braaten, and G. P. Lepage, Phys. Rev. D **51**, 1125 (1995).

[28] T. Mannel and G. A. Schuler, Z. Phys. **C67**, 159 (1995).

[29] Godfrey, Stephen, Phys. Rev. D **70**, 054017 (2004).

[30] HPQCD Collaboration, http://www.physics.gla.ac.uk/HPQCD/.

[31] Allison, Ian F. and Davies, Christine T. H. and Gray, Alan and Kronfeld, Andreas S. and Mackenzie, Paul B. and Simone, James N., Phys. Rev. Lett. **94**, 172001 (2005).

[32] K. Anikeev *et al.*, *B* physics at the Tevatron: Run II and beyond, 2001, hep-ph/0201071.

[33] Chang, Chao-Hsi and Wang, Jian-Xiong and Wu, Xing-Gang , Phys. Rev. D **70**, 114019 (2004).

[34] Chang, Chao-Hsi and Qiao, Cong-Feng and Wang, Jian-Xiong and Wu, Xing-Gang , Phys. Rev. D **71**, 074012 (2005).

[35] C.-H. Chang, J.-X. Wang, and X.-G. Wu, Computer Physics Communications **175**, 624 (2006).

[36] J. D. Bjorken, Estimate of decay branching ratios for hadrons containing charm and bottom quarks, draft report, 1986.

[37] M. Bauer, B. Stech, and M. Wirbel, Z. Phys. **C34**, 103 (1987).

[38] V. V. Kiselev, Mod. Phys. Lett. **A10**, 1049 (1995), hep-ph/9409348.

[39] V. V. Kiselev, Int. J. Mod. Phys. **A9**, 4987 (1994).

[40] V. V. Kiselev, A. K. Likhoded, and A. V. Tkabladze, Phys. At. Nucl. **56**, 643 (1993).

[41] V. V. Kiselev, A. K. Likhoded, and A. I. Onishchenko, Nucl. Phys. **B569**, 473 (2000), hep-ph/9905359.

[42] V. V. Kiselev, A. E. Kovalsky, and A. K. Likhoded, Nuclear Physics B **585**, 353 (2000), arXiv:hep-ph/0002127.

[43] A. I. Onishchenko, (1999), hep-ph/9912424.

[44] V. V. Kiselev and A. E. Kovalsky, Physics of Atomic Nuclei **63**, 1640 (2000).

[45] I. Bigi, Physics Letters B **371**, 105 (1996).

[46] V. V. Kiselev, Exclusive decays and lifetime of B_c meson in QCD sum rules, 2002, hep-ph/0211021.

[47] CDF Collaboration, Physical Review Letters **81**, 2432 (1998).

[48] A. Abd El-Hady, J. H. Munoz, and J. P. Vary, Phys. Rev. **D62**, 014019 (2000), hep-ph/9909406.

[49] C.-H. Chang and Y.-Q. Chen, Phys. Rev. **D49**, 3399 (1994).

[50] M. A. Ivanov, J. G. Korner, and P. Santorelli, Phys. Rev. **D63**, 074010 (2001), hep-ph/0007169.

[51] D. Scora and N. Isgur, Phys. Rev. **D52**, 2783 (1995), hep-ph/9503486.

[52] A. Y. Anisimov, I. M. Narodetsky, C. Semay, and B. Silvestre-Brac, Phys. Lett. **B452**, 129 (1999), hep-ph/9812514.

[53] P. Colangelo and F. De Fazio, Mod. Phys. Lett. **A14**, 2303 (1999), hep-ph/9904363.

[54] T. E. Browder, K. Honscheid, and D. Pedrini, Ann. Rev. Nucl. Part. Sci. **46**, 395 (1996), hep-ph/9606354.

[55] CDF Collaboration, Physical Review Letters **100**, 182002 (2008).

[56] D0 collaboration, Physical Review Letters **101**, 012001 (2008).

[57] CDF Collaboration, Measurement of the B_C Lifetime in $B_C \to J/\psi + l + X$ Decays, http://www-cdf.fnal.gov, 2008, CDF note 9294.

[58] D0 collaboration, Physical Review Letters **102**, 092001 (2009).

[59] C. Chang, C. Driouichi, P. Eerola, and X. Wu, Computer Physics Communications **159**, 192 (2004).

[60] C. Chang, J. Wang, and X. Wu, Computer Physics Communications **159**, 241 (2006).

[61] I. P. Gouz, V. V. Kiselev, A. K. Likhoded, V. I. Romanovsky, and O. P. Yushchenko, Phys. Atom. Nucl. **67**, 1559 (2004), hep-ph/0211432.

[62] C. Carli, Chamonix 2009 Workshop on LHC Performance Proceeding, 2009, http://cdsweb.cern.ch/record/1161742.

[63] http://cmssw.cvs.cern.ch/cgi-bin/cmssw.cgi/CMSSW/Configuration/-GenProduction/python/PYTHIA6_JPsi_10TeV_cff.py?view=markup.

[64] https://twiki.cern.ch/twiki/bin/view/CMS/EvtGenInterface.

[65] A. Ryd *et al.*, *EvtGen: A Monte Carlo Generator for B-Physics*, EVTGEN-V00-11-07.

[66] F. Abe *et al.*, Phys. Rev. Lett. **69**, 3704 (1992).

[67] S. Abachi *et al.*, Physics Letters B **370**, 239 (1996).

[68] M. Bargiotto and V. Vagnoni, Heavy Quarkonia sector in PYTHIA6.324: tuning, validation and perspectives at LHC(b), 2007, Public Note: LHCb-2007-042.

[69] https://twiki.cern.ch/twiki/bin/view/CMS/TriggerTables.

[70] The CMS Collaboration, CERN Report No. LHCC-G-134, 2007 (unpublished).

[71] http://cms-project-confdb-hltdev.web.cern.ch/cms-project-confdb-hltdev/browser/.

[72] https://twiki.cern.ch/twiki/bin/view/CMS/SWGuideKalmanVertexFitter.

[73] https://twiki.cern.ch/twiki/bin/view/CMS/SWGuideKinematicVertexFit.

[74] K.Prokofiev and T. Speer, A kinematic fit and a decay chain reconstruction library, 2004.

[75] C. e. a. Amsler, Physics Letters B **667**, 66 (2008).

[76] FOCUS, J. M. Link *et al.*, Phys. Lett. **B537**, 192 (2002), hep-ex/0203037.

[77] *RooFit Users Manual v2.91*, 2008.

[78] http://projects.hepforge.org/pythia6/.

[79] T. Sjöstrand *et al.*, JHEP **026** (2006).

[80] http://www.itp.ac.cn/ zhangzx.

[81] G. P. Lepage, Journal of Computational Physics **27**, 192 (1978).

[82] https://twiki.cern.ch/twiki/bin/view/CMS/SWGuideBcGenerator.

[83] https://twiki.cern.ch/twiki/bin/view/CMS/HARDCOLInterface.

[84] https://twiki.cern.ch/twiki/bin/view/CMS/EDDEInterface.

ACKNOWLEDGMENTS

This is the most read part of the thesis and, as a result, the most difficult to write. I hope not to forget anyone. I am grateful to Sandra, Daniele and Luigi who all helped me during this thesis work. They gave me directions as well as conveying their interest in this physics research. Many thanks also to the other components of the group: Dario, Silvano, Marco, Mauro and Giuseppe, with his "psychiatric help" in CMSSW and C++.
An acknowledgment also to the Milano-Bicocca CMS ECAL group, an interesting source of ideas and information.
I need to thank Julia Yarba for her help and explanations during my activity in the Generator WG of the CMS Collaboration.
I must also mention a lot of other people: Valentina, Martina, Arabella, Erica, Gemma, Filippo, Marco, Andrea, Marco, Federico and Cecilia; I met all of them, for different reasons and at different times, during this PhD: without them doing science would have not been the same. In this *friend list* there is also Leonardo who tolerated me and my problems of all kinds (but mainly computing) every day, for more or less two years. Curiously, he still speaks with me, but he is now living far away…
Many thanks to Paolo and Luca that were always very patient with one of their *most efficient* debuggers.
Finally, I have to thank two people outside Milano for their language support: Michele, from Oxford University, who unfortunately has a cousin ignorant in English, and Marta, an old university friend in Como, who patiently replied to all of my questions and doubts.